UNIVERSITY OF SOUTHAMPTON

FACULTY OF PHYSICAL AND APPLIED SCIENCES
Physics

Simulation and Design of Lateral Photo-Dember Emitters and a Novel Microwave Antenna

by

Lewis C. Maple

Thesis for the degree of Doctor of Philosophy

June 2017

UNIVERSITY OF SOUTHAMPTON

ABSTRACT

FACULTY OF PHYSICAL AND APPLIED SCIENCES
Physics

Doctor of Philosophy

SIMULATION AND DESIGN OF LATERAL PHOTO-DEMBER EMITTERS AND A NOVEL MICROWAVE ANTENNA

by Lewis C. Maple

In this thesis I will discuss the modelling and testing of THz and microwave emitters. I firstly present a new model for the lateral photo-Dember effect and find that the previous 1D model by Barnes et. al. is incomplete. I use a 2D solution of the drift diffusion equation and feed the currents in to a finite difference time domain algorithm. In order to have a realistic representation of the far-field to the detector I use a far-field algorithm.

I show that the dynamics of the system are dependent on the currents travelling perpendicular to the semiconductor surface, as opposed to just the lateral currents as previously thought. I then go on to compare this model with experimental results. The experiment in question involved the examination of photo-Dember emission when the semiconductor is under the influence of a biasing electric field. I also performed a separate experiment in which a gap was introduced to various lateral Photo-Dember emitters in order to observe its effects in both the time and frequency domains.

I also present a novel microwave antenna based on the fishscale and split-ring resonator metamaterial designs. I demonstrate that mutual coupling between the fishscale and SRRs is responsible for creating a greater absorption of the input signal than either component is capable of in isolation. The antenna was tested, and I compare the experimental results with the computational model.

Contents

Declaration of Authorship xiii

Acknowledgements xiv

Nomenclature xv

1 Introduction 1
- 1.1 THz Emitters . . . 1
  - 1.1.1 Photoconductive Antennas . . . 2
  - 1.1.2 Photo-Dember Emitters . . . 4
  - 1.1.3 Lateral Photo-Dember Emitters . . . 4
- 1.2 Metamaterials . . . 5
- 1.3 Thesis overview . . . 9

2 Modelling The Lateral Photo-Dember Effect 11
- 2.1 Introduction . . . 11
- 2.2 Finite Difference Methods . . . 12
  - 2.2.1 First order approximations . . . 12
  - 2.2.2 Second order approximations . . . 13
- 2.3 Modelling the Drift-Diffusion equation . . . 14
  - 2.3.1 Carrier Transport . . . 14
  - 2.3.2 Carrier Generation and Recombination . . . 16
    - 2.3.2.1 Photogeneration . . . 17
    - 2.3.2.2 Radiative Recombination . . . 17
    - 2.3.2.3 Shockley-Read-Hall Recombination . . . 18
    - 2.3.2.4 Auger Recombination . . . 19
    - 2.3.2.5 Surface Recombination . . . 19
  - 2.3.3 Calculating the Electric Field . . . 20
  - 2.3.4 The Scharfetter-Gummel discretization . . . 21
- 2.4 The Finite Difference Time Domain Method . . . 23
  - 2.4.1 Introduction and Setting Up The Problem . . . 23
  - 2.4.2 Boundary Conditions . . . 26
    - 2.4.2.1 Perfect Electric Conductors . . . 26
    - 2.4.2.2 Absorbing Boundary Conditions . . . 26
  - 2.4.3 Far-Field Analysis . . . 27
    - 2.4.3.1 Love's Equivalence Principle . . . 27
    - 2.4.3.2 The far-field algorithm . . . 28
- 2.5 Modelling the Lateral Photo-Dember Effect . . . 29

2.5.1 1D Diffusion Model in x 31
2.5.2 1D Diffusion Model in y 37
2.5.3 2D Drift Diffusion 41
2.5.4 Spot size and Fluence 47
2.6 Conclusions 50

3 THz Experiments **51**
3.1 Terahertz Time Domain Spectroscopy 51
3.2 Bias Experiments 52
3.3 Spaced LPD emitters 59
3.3.1 Results 60
3.4 Conclusions 64

4 Microwave Antenna **66**
4.1 Introduction 66
4.1.1 Microwave Spectroscopy 67
4.2 The Finite Element Method 68
4.2.1 Strong to Weak Formulation 69
4.2.2 Descretization 70
4.2.3 Galerkin Method 72
4.2.4 Perfectly matched layers 73
4.3 Metamolecule Design 73
4.4 Numerical Investigations 75
4.5 Experimental Results 77
4.6 Effect of SRR size on resonant properties 78
4.7 Use as a radiative antenna 80
4.8 Measured Far Field 81
4.9 Conclusions 86

5 Conclusions **87**
5.1 Modelling the Lateral Photo-Dember effect 88
5.2 Experiments on the Lateral Photo-Dember effect 88
5.3 An Investigation in to a Novel Microwave Antenna 89

References **90**

List of Figures

1.1 Geometry and workings of a PCA. The electric field accelerates the electrons and holes in opposite directions creating a rapidly changing dipole. We would expect to see THz emission in both directions perpendicular to the semiconductor surface. 3

1.2 Geometry and workings of a classical photo-Dember emitter. The higher mobility of the electrons has allowed them to diffuse further and faster than the holes, creating a net current in the vertical direction. The currents are equal and opposite in the horizontal direction, leading to a net current of zero lateral to the semiconductor surface. 5

1.3 Geometry and workings of a lateral photo-Dember emitter. The higher mobility of the electrons has allowed them to diffuse further and faster than the holes, creating a net current in the vertical direction. The currents are equal and opposite in the horizontal direction, like the classical PD despite their asymmetric distribution. 6

1.4 The mechanism behind the LPD effect according to Klatt et al. Since the carrier density gradient is much greater on the right (masked side) they proposed that there is a greater current in this direction, leading to an overall net current. 6

1.5 The current understanding of the mechanism behind the LPD effect. The grey region is semiconductor, while all else is air. The black and red arrow shows the laser pulse, the green arrows the induced lateral currents, the black arrows the directions in which the wave can be detected in the far field, and the dashed arrow showing destructive interference. The red and blue curves indicate electric fields with opposite polarity in x. In a, there is no metal mask and all parts of the wave may freely radiate. In b, the metal mask causes a reflection on the wave with a $\frac{\pi}{2}$ phase shift and destructively interferes with the part of the wave beneath the metal mask. 7

1.6 Geometry of various split ring resonators. Each contains at least one loop and at least one gap. 8

1.7 The path of light through a superlens 8

2.1 Finite difference discretization. A continuous function, shown in (a), is discretized at points x_0, x_1 etc. The corresponding discrete function is shown in (b). 12

2.2 The placement of the calulated densities (blue dots) and calculated currents (red arrows). The dashed black lines represent the mesh. 16

2.3 Direct and indirect band transitions in semiconductors. The blue lines represent a change in energy of an electron due to photon absorption, while the red line represents a change in momentum due to phonon absorption. (a) shows a direct transition in a direct semiconductor, (b) shows a direct transition in an indirect semiconductor and (c) shows an indirect transition in an indirect semiconductor. 17
2.4 A representation of the three primary forms of recombination in bulk semiconductors. Radiative recombination involves a conduction electron moving down to the valence band and recombining with a hole. Shockley-Read-Hall recombination involves a carrier of each species falling in to a trap site, while Auger recombination involves the transferral of energy to a third carrier. 18
2.5 Arrangement of a 1D FDTD problem in time and space. The red dots represent the electric field nodes while the blue dots represent the magnetic field nodes. 25
2.6 Arrangement the Yee cell for the 2D TE case. For the TM case, the green dot would represent E_z and the arrows would represent the different components of H. 26
2.7 Love's equivalemce principle. Using equations 2.50 and 2.53, it is possible to recreate the fields external to the equivalent surface by applying the derived currents to the surface. 28
2.8 A visualisation of the equivalent surface and the associated vectors used in the far-field calculation. 29
2.9 The alignment of the DD solver current and carrier densities with respect to the FDTD grid. The DD and FDTD currents are located in the same location, while the carrier density nodes are staggerred compared to the FDTD magnetic field nodes. 30
2.10 Field dependent mobility for GaAs used in the model. 32
2.11 Field dependent drift velocity due to the mobility for GaAs used in the model. 32
2.12 Field dependent diffusion coefficient used for GaAs used in the model. . . 33
2.13 Current density evolution for a 1D distribution of carriers confined to the x-direction in bulk LT GaAs. The laser spot size is 10 μm, which is cut off by the presence of a metal mask at x = 0. This model does not include drift. 33
2.14 Current density evolution for a 1D distribution of carriers confined to the x-direction for a 1D problem using the same parameters as fig. 2.13, but with the SRH term from ref. [1]. This model does not include drift. . . . 34
2.15 Density of holes and electrons in an SI-GaAs sample with no SRH term. What would be the SRH term for this distribution in LT-GaAs is also shown. In LT-GaAs, recombination would occur much more rapidly where $x < 0$. This model does not include drift. 35
2.16 Out-of-plane magnetic field evolution for an LT-GaAs sample with a 1D current restricted to the x direction. The result agrees with Barnes et. al. that the symmetry is broken by destructive interference beneath the metal mask. This model does not include drift. 36
2.17 Current density evolution for a 1D distribution of carriers in LT GaAs confined to the y direction. The effects of electric field are neglected. . . . 37

2.18 Out-of-plane magnetic field evolution for an LT-GaAs sample with 1D current restricted to the y direction. The result shows that the symmetry is broken by constructive interference beneath the metal mask. This model does not include drift. 38

2.19 Out-of-plane magnetic field for an LT-GaAs sample 1 ps after peak illumination with a 1D current restricted to the x direction and the entire domain modelled as GaAs. The radiation is quadrupolar in nature, which would lead to destructive interference from a metal mask placed just above the currents. This model does not include drift. 39

2.20 Out-of-plane magnetic field for an LT-GaAs sample 1 ps after peak illumination with a 1D current restricted to the y direction and the entire domain modeled as GaAs. The radiation is dipolar in nature, which would lead to constructive interference from a metal mask placed just above the currents. This model does not include drift. 40

2.21 Out-of-plane magnetic field for an LT-GaAs sample with 2D currents, negelcting the effects of the electric field. Note the similarity to the 1D system with only y currents, in that constructive interference occurs beneath the metal mask. This model does not include drift. 41

2.22 Out-of-plane magnetic field for an LT-GaAs sample with 2D currents with the effects of drift included. Again, constructive interference occurs beneath the metal mask. 43

2.23 Far-field time-domain scans for two 2D system, one in which only diffusion is considered and one in which both drift and diffusion are considered. The lower intensity of the drift and diffusion system is due to drift currents opposing the diffusion currents. 44

2.24 Far Field linescans for an LT-GaAs emitter taken at different far-field angles with both drift and diffusion included. 45

2.25 A comparison of the average far field linescans between -25° to 25° to the far-field linescan at 0°. The average linescan shows the small tick before peak emission as observed in experimentaiton. 46

2.26 The results of the spot size experiment for SI-GaAs performed by McBryde et al.[2] 47

2.27 Spectral powers given by the waveforms of $\delta J_y/\delta t$ integrated over the simulation domain. These results indicate that the intensity of the observed radiation due to the currents perpendicular to the semiconductor surface should change with spot size. 48

2.28 Spectral powers given by the waveforms of $\delta J_x/\delta t$ integrated in the area not beneath the metal mask for a spot size of 8 μm, and those for $\delta J_y/\delta t$ for spot sizes of 8 and 60 μm integrated over the simulation domain. Only the results from one spot size were used for the x currents, as there is no significant change with spot size. This indicates that the resulting THz emission due to the currents in x do not change with spot size. 49

3.1 A typical THz-TDS setup 52

3.2 The setup for the biasing experiments. The two gold contacts are used as electrodes to apply a voltage across the sample. 52

3.3 The linescans for the experiments performed by Mark Barnes.[3] 53

3.4 An attempt to recreate the experimental results using the parameters used in chapter 2. As can be seen, the biasing field dominates the emission. 54

3.5 A second attempt to recreate the results of the experiment by Barnes. et. al. In this model, the biasing field used in the previous model was divided by ϵ_{GaAs} . . . 55

3.6 The electron temperature derived from the Einstein relationship between μ and D. The peak in temperature occurs at the saturation field. . . . 56

3.7 The biasing experiment, assuming the values of μ and D are those at saturation with a peak pulse intensity of $1 \times 10^{12} Wm^{-2}$ . . . 57

3.8 The biasing experiment, assuming the values of μ and D are those at saturation with a peak pulse intensity of $1 \times 10^{11.5} Wm^{-2}$ and a spot size of 45 μm . . . 58

3.9 The integrated time derivative of the currents in x on the unmasked side under different bias conditions for a pulse of peak intensity $1 \times 10^{11.5} Wm^{-2}$ and spot size $45 \mu m$. Note that the magnitude is much greater for the biased samples. . . . 59

3.10 Geometry of the spaced LPD emitters . . . 60

3.11 Time domain scan of the spaced photo-Dember emitters with SU-8 thicknesses of 35 and 90 μm. As expected, the spacing causes the pulse to broaden. . . . 61

3.12 An illustration of the photo-Dember effect after illumination with an SU-8 cavity present. The black arrows represent possible paths for THz raditaion To the left of the mask, the fields are free to radiate. To the right of the mask edge, the fields travelling upwards are reflected after a delay and then propagate downwards where they expoerience interference. 61

3.13 Fourier transform of the emitter with a 90 μm spacing. Note the FSR created by the introduction of a cavity. . . . 62

3.14 Time domain scans for the two cavity thicknesses reproduced in the model. While the stretching of the temporal pulse is not comparable to the experiment, the reduction in the peak intensity is. . . . 63

3.15 Fourier scans for the two cavity thicknesses reproduced in the model. While the range of frequencies present is much greater than in experimentation, the same FSR can be observed. . . . 64

4.1 The setup used for far-field measurements of microwave emitters. . . . 69

4.2 An example of an FEM mesh used to discretize a complex geometry. . . . 69

4.3 The blue line shows a an approximate solution we hope to reach. The red lines show the basis functions at each internal node. . . . 71

4.4 (a) The geometry and dimensions of one unit segment of the modified fish-scale structure. (b) The geometry of a fish-scale segment complete with inner ring to form a SRR. The angular gap θ used for the inner split ring is 40°. (c) The final hybrid fishscale/SRR metamolecule. In the finalised design, $r_o = 1.1$ mm and $r_i = 0.9$ mm. . . . 74

4.5 (a) Top-down view of the hybrid structure on the CPW with placement relative to the CPW gaps (shown in red). (b) View from the side of the same sample showing the dimensions of the device layers. . . . 74

4.6 Shown above the calculated S_{21} for the SRRs (red), the fishscale (blue), and the hybrid SRR and fishscale structure (green). . . . 76

4.7 Electric field maps produced by the CPW-loaded structures determined using COMSOL simulation. The y-polarized electric fields (according to the geometry of Fig. 4.4 and perpendicular to the propagation axis) for both the isolated fishscale (a) and hybrid structure (b) are shown. The structures were excited by a coaxial port from the right hand side of the figure. 76
4.8 Comparison of computational results (green) with experimental results (blue). The S_{21} for the fishscale is shown in (a) and that of the hybrid structure is shown in (b). 77
4.9 Absorption as a function of frequency and SRR size, normalised to the inner radius of the original SRR dimension, which is 0.9 mm. At smaller SRR sizes, both the original fishscale resonance and SRR introduced resonance can be identified separately. For the smallest geometry geometry, the fishscale resonance can be seen on the left while that of the SRRs is seen on the right. 78
4.10 The y-polarization of the electric fields produced by the hybrid structure with SRRs 0.98 times the original size at the resonance around 15.9 GHz. 79
4.11 Absorption as a function of frequency of frequency for the two most extreme SRR sizes shown in Fig. 4.9. The scan for $r_i = 0.9$ mm × 0.975 is shown in blue, where hybrid mode can be seen on the right while the fishscale mode can be seen on the left. The scan for $r_i = 0.9$ mm × 1.125 is shown in green and the fishscale mode can be seen in approximately the same place, while the hybrid mode is starting to appear on the left. . 79
4.12 The comparison between the differences between P_{lost} for the hybrid structure and that of the fishscale is shown in (a). The experimental results are in blue while the computational results are in red. The frequency shift (about 0.5 GHz) of the resonance between the two sets of results is consistent with the previous computational results shown in Fig. 4.8. . . . 80
4.13 The modelled far field at resonance as a function of angle for the polarisation parallel to the length of the CPW. The scale is in dB. 83
4.14 The experimental far field at resonance as a function of angle for the polarisation parallel to the length of the CPW. The scale is in dB. 83
4.15 The modelled far field at resonance as a function of angle for the polarisation perpendicular to the plane of the CPW. The scale is in dB. 84
4.16 The experimental far field at resonance as a function of angle for the polarisation perpendicular to the plane of the CPW. The scale is in dB. . 84
4.17 A photograph of the sample and the wooden support used for the far-field measurements. 85

———-

Declaration of Authorship

I, Lewis C. Maple , declare that the thesis entitled *Simulation and Design of Lateral Photo-Dember Emitters and a Novel Microwave Antenna* and the work presented in the thesis are both my own, and have been generated by me as the result of my own original research. I confirm that:

- this work was done wholly or mainly while in candidature for a research degree at this University;
- where any part of this thesis has previously been submitted for a degree or any other qualification at this University or any other institution, this has been clearly stated;
- where I have consulted the published work of others, this is always clearly attributed;
- where I have quoted from the work of others, the source is always given. With the exception of such quotations, this thesis is entirely my own work;
- I have acknowledged all main sources of help;
- where the thesis is based on work done by myself jointly with others, I have made clear exactly what was done by others and what I have contributed myself;
- parts of this work have been published as: [4]

Signed:...

Date:..

Acknowledgements

Thanks to my family, my friends, my group and Vasilis.

And of course, Ania.

Nomenclature

DD	Drift-diffusion
FDTD	Finite difference time domain
CPW	Coplanar Waveguide
FEM	Finite Element Method
FFT	Fast Fourier transform
LT-GaAs	Low temperature gallium arsenide
LPD	Lateral photo-Dember
PCA	Photoconductive Antenna
PD	Photo-Dember
SI-GaAs	Semi insulating gallium arsenide
SRH	Shockley-Read-Hall
SRR	Split ring resonator
TE	Transverse electric
TM	Transverse Magnetic
Thz-TDS	Terahertz time domain spectroscopy
VNA	Vector network analyzer

Chapter 1

Introduction

1.1 THz Emitters

Investigations into the field of THz emitters and receivers have attracted considerable interest over recent years [5, 6, 7]. Though most recent THz research has focused primarily on the use of THz radiation to perform spectroscopy usually using THz time domain spectrometers [8, 9], there has also been research in communications [10] and submillimetre astronomy which is one of the first and traditional THz research areas [11]. The attractiveness of the use of THz spectroscopy comes from the fact that a large number of organic and inorganic molecules have resonances within the THz spectrum [12], so a wide range of materials and substances can in theory be detected by terahertz time domain spectroscopy (THz-TDS). There are species that have THz absorption lines such as water[13], molecular oxygen[14], ozone[15], carbon monoxide[16] and nitrogen monoxide[17]. There are also species that have only THz lines such as atomic oxygen, OH and HO_2[18]. For these reasons meteorological satellites and space missions are equipped with THz detection instruments. However, THz is becoming more interesting to industry for quality control and also for identification of organic molecules in pharmaceuticals, drugs explosives etc.

The primary difficulty in generating THz is due to its difficult position in the electromagnetic spectrum. Lower frequencies in the GHz range can be easily produced by oscillating electric currents, while higher frequencies towards the visible spectrum are produced from the changing of electron states in atoms[19]. In the THz range, electronics have poor efficiency to create fast currents oscillating in the picosecond time scale. Also, electronic states are separated by less energy than the energy spread dictated by thermal motions, therefore any lasing transition in the THz is difficult to be achieved at room temperature[20].

The difficulty of generating sources of THz radiation has been overcome with many novel methods, though the most commonly used method for both detection and emission is the photoconductive (PC) antenna[21, 22]. Such an antenna utilises two plates on the surface of a semiconductor separated by a small gap with a potential difference between them. For emission, a femtosecond laser pulse is then used to excite carriers at the surface of the semiconductor, which due to the bias are accelerated in one direction. This acceleration causes a transient wave to be emitted perpendicular to the surface of a semiconductor. When using a PC antenna for detection, no bias is applied. Rather, the femtosecond laser pulse is sent to the detector to create carriers within the semiconductor. If the THz pulse arrives when the carriers are excited within the semiconductor, the THz pulse will accelerate them in a certain direction, which can be detected as a current between the contacts[23].

There are many potential applications for THz spectroscopy, some of which I will briefly outline here to give a flavour for the research.

Unlike X-Rays, THz radiation is non-ionising and therefore unable to damage DNA[24]. This is obviously a huge attraction for the medical industry, where the safety of the patient is key. However, the primary limiting factor to its application, especially when compared to X-Rays, is the low penetration depth of THz radiation in tissue[25]. This depth typically on the order of millimetres or less, and as such THz does not lend itself to the wide range of imaging available with already existing technologies such as magnetic resonance imaging (MRI) or positron emission tomography (PET).

This is not to say that THz radiation is without its uses in the medical world. One such potential application is that of the early identification of skin cancers. Due to the different concentrations of water in healthy tissue and cancerous tissue, it has been demonstrated that THz is able to identify between the two[26]. Furthermore there are applications in endoscopy where a THz probe can identify between cancerous and healthy tissue[27], and has been used in London hospitals in order to identify if there are still cancer cells in a body cavity after an operation[28]. THz imaging has also proven useful in dentistry, allowing for the 3D imaging of teeth[29].

The security industry is also a key target for the application of THz technology. Many illegal materials such as explosives and narcotic drugs have absorption bands in the THz spectrum[30, 31]. Not only are THz scanners already in use at airports, there is a possible use for them in the postal industry; new THz scanners are able to identify substances within a package without the need to open it.

1.1.1 Photoconductive Antennas

Photoconductive antennas (PCAs) are commonly used emitters and detectors for Terahertz Time-Domain Spectroscopy. A PCA typically consists of two conducting plates separated by a small gap fabricated on a semiconductor surface, usually GaAs[32] as shown in fig. 1.1 . For use in emission, a potential difference is applied between the two

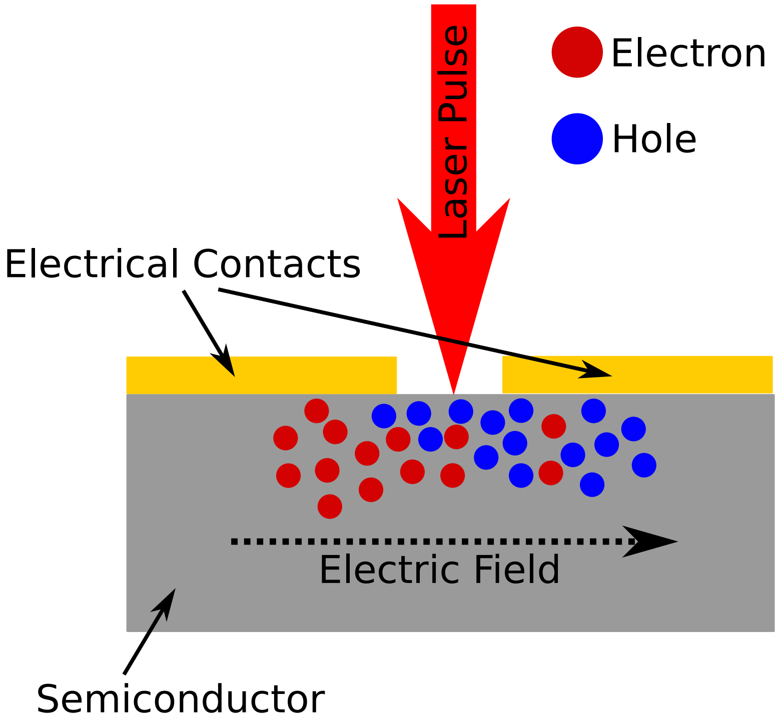

Figure 1.1: Geometry and workings of a PCA. The electric field accelerates the electrons and holes in opposite directions creating a rapidly changing dipole. We would expect to see THz emission in both directions perpendicular to the semiconductor surface.

electrodes creating an electrical bias in the substrate. An ultrafast laser pulse is then used to excite carriers in to the conduction band of the semiconductor. The generated carriers are accelerated by the applied field, the motion of which cause a rapidly changing dipole. This dipole lateral to the surface of the semiconductor produces emission perpendicular to the semiconductor surface, typically with a broadband nature ranging from around 100 GHz to 2-3 THz[33, 34, 35]. An illustration of this process is shown in Fig. 1.1.

When used for detection, the entire process is reversed. The detector is probed at certain times by the illumination of an ultrafast laser. The carriers generated by the laser pulse do not accelerate as there is no applied electric field. However, if a THz pulse reaches the detector at the same time as the probe pulse, the generated carriers will be accelerated by the THz field. This generated current can then be read by measuring the voltage between the two metallic plates. By choosing a substrate for the detector with a low carrier lifetime, the lifetime of the photoexcited carriers is much shorter than the THz pulse and the carriers effectively see a small part of the THz wave as a DC field[36]. Therefore, by moving the probe pulse forward and backwards in time relative to the generation of THz, it is possible to map out the entire generated THz field. An illustration of a THz-TDS setup is shown in chapter 3.

1.1.2 Photo-Dember Emitters

Photo-Dember emitters (PDEs) are also based on semiconductors but unlike a PCA, they require no bias and can therefore be used in the absence of any applied electric field. The geometry of a PDE is extremely simple, being only a piece of semiconductor and requiring no further fabrication or deposition. When an incident laser pulse hits a PDE, a large number of photocarriers are generated in the same manner as the incident pulse on a PCA. In the presence of no external field, the carriers are free to diffuse in all directions, the PDE is based on the difference of mobilities between holes and electrons for a dipole to be generated [37, 38, 39]. In the direction lateral to the surface, the overall net current is zero and the near fields generated by the current in this direction cancel out in the far field. In the direction perpendicular to the semiconductor surface, however, there is a net current due to the break in symmetry from the semiconductor surface[1]. For this reason, the fields emitted in the direction lateral to the surface do not cancel out in the far field and can be detected.

Though the intensity of the emitted radiation is lower from a PDE than from a PCA, they do hold several advantages. Firstly, due to their simple design they are far less of a task to fabricate. Secondly, since no bias need be applied, they do not suffer the same amount of degradation over time when compared to a PCA. Thirdly, although this is usually depending on the detection mechanism and specific experimental configuration, they generate less electrical noise. Their main drawback, however, is the difficulty in out coupling their emission to something useful, since the direction of the emitted THz pulse is perpendicular to the direction of the incoming optical beam.

1.1.3 Lateral Photo-Dember Emitters

Lateral photo-Dember emitters (LPDs) are designed to generate THz emission in the direction perpendicular to the semiconductor surface. By introducing a metal mask as shown in fig. 1.3 and illuminating the semiconductor at the edge of this mask, symmetry is broken in the lateral direction and the emitted THz pulse no longer cancels in the far field. First fabricated and tested by Klatt et. al, it was initially proposed that the break in symmetry was due to an asymmetric carrier density, causing a greater current to be generated on the masked side than the masked side. Their argument was that, since the microscopic current $\mathbf{j} \propto \frac{dN}{dx}$ where N is the carrier distribution[40]. This model is illustrated in fig. 1.4. This argument was disproven by Barnes et. al, who demonstrated that an asymmetrical carrier distribution does not lead to an overall net current[37]. The argument against Klatt's theory can be understood from the equation relating the net current **J** to the microscopic currents **j**

$$J = \int_{-\infty}^{\infty} j dx \propto \int_{-\infty}^{\infty} \frac{dN}{dx} dx = [N]_{-\infty}^{\infty} = 0 \tag{1.1}$$

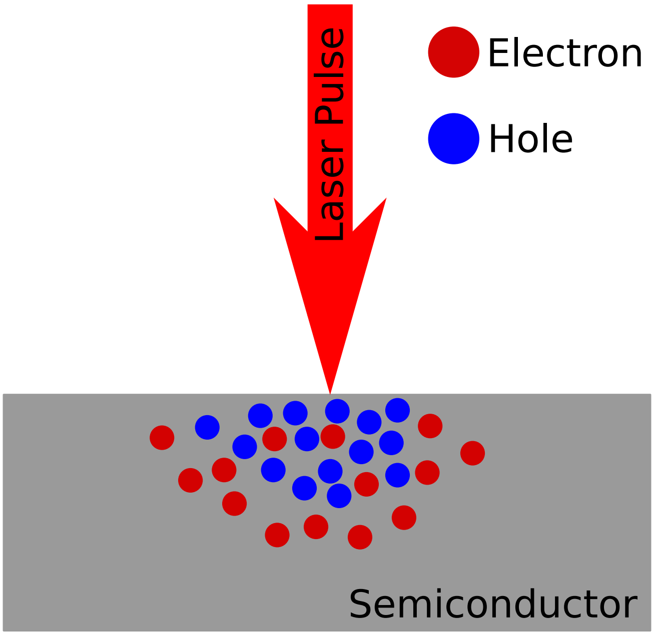

Figure 1.2: Geometry and workings of a classical photo-Dember emitter. The higher mobility of the electrons has allowed them to diffuse further and faster than the holes, creating a net current in the vertical direction. The currents are equal and opposite in the horizontal direction, leading to a net current of zero lateral to the semiconductor surface.

where N is the distribution of carriers. From this equation, it is apparent that no matter how we define N, we will never reach a net current in the sample. Barnes et al. explored in [41] experimentally if an asymmetric carrier concentration would generate THz emission and he found, as he hypothesised, that it did not. Therefore, Barnes et al. proposed an alternative explanation to justify the THz emission and this was that the metal mask reflected part of the THz wave being emitted out towards the laser source, which in turn destructively interferes with the wave emitted in the opposite direction due to a π phase shift[41] of the electric field. This theory is illustrated in fig. 1.5.

While also possessing the same advantages of a PDE over a PCA, namely simplicity in design and not requiring an applied voltage, they also have the quality of emitting in a direction parallel to the path of the optical beam. This allows for a much simpler integration in to THz-TDS system. While a classical PDE would require a drastic change from the setup of a PCA emitter, an LPD emitter could simply be switched and used in its place. This thesis will, in part, attempt to demonstrate that the currently accepted explanation for the emission mechanism of LPDs is in fact incomplete.

1.2 Metamaterials

The attraction towards metamaterial research can in part be understood simply from the meaning of the word. The prefix ‘Meta-’ comes from Greek and means ‘beyond’;

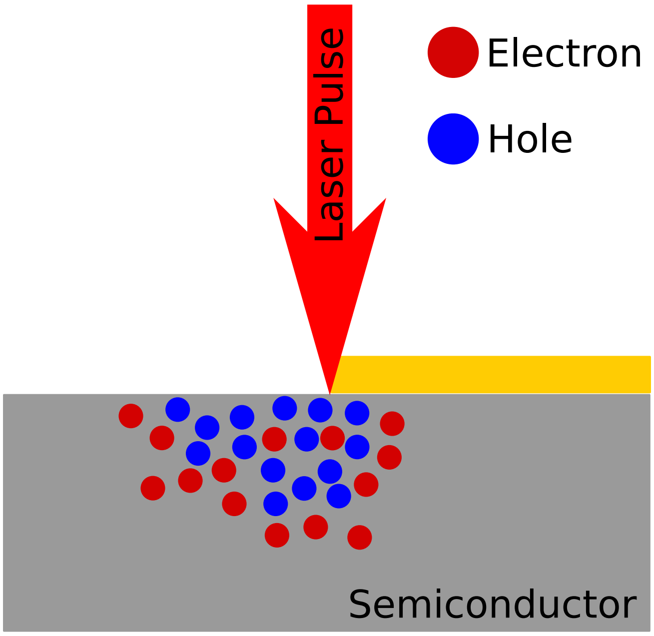

Figure 1.3: Geometry and workings of a lateral photo-Dember emitter. The higher mobility of the electrons has allowed them to diffuse further and faster than the holes, creating a net current in the vertical direction. The currents are equal and opposite in the horizontal direction, like the classical PD despite their asymmetric distribution.

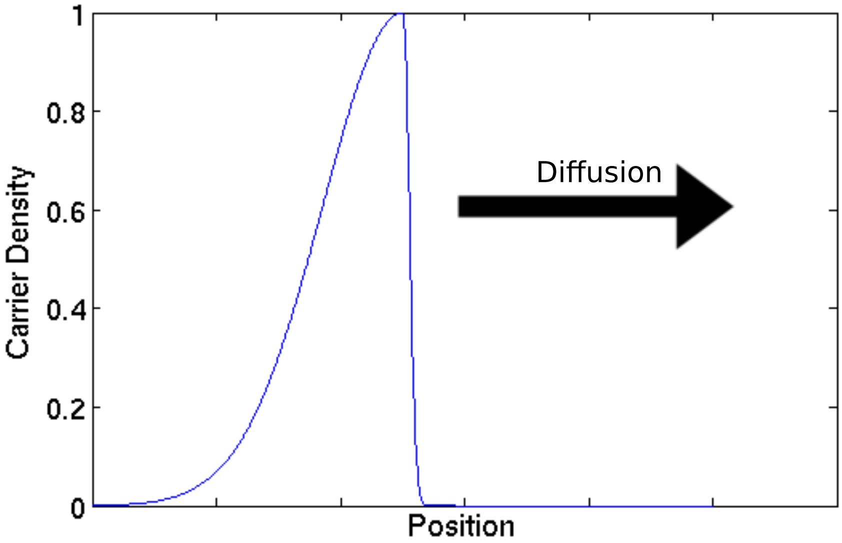

Figure 1.4: The mechanism behind the LPD effect according to Klatt et al. Since the carrier density gradient is much greater on the right (masked side) they proposed that there is a greater current in this direction, leading to an overall net current.

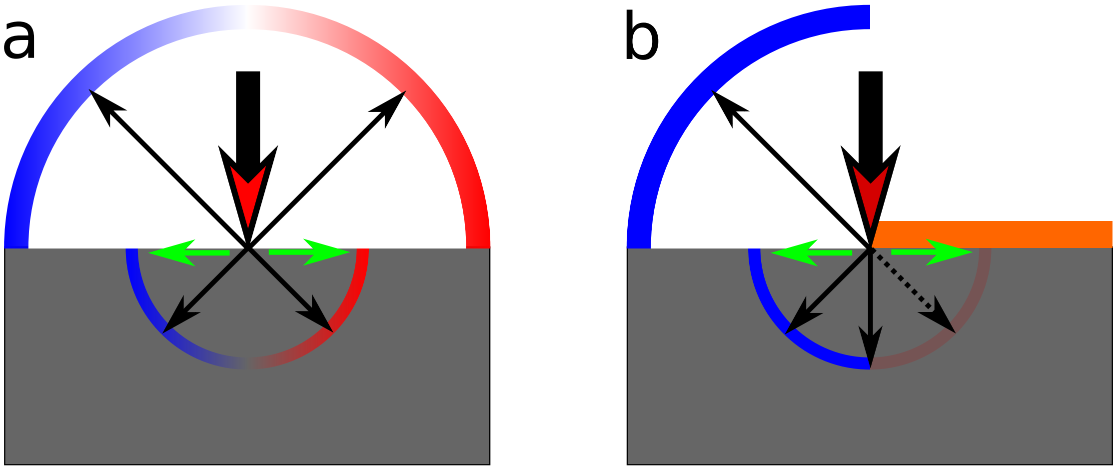

Figure 1.5: The current understanding of the mechanism behind the LPD effect. The grey region is semiconductor, while all else is air. The black and red arrow shows the laser pulse, the green arrows the induced lateral currents, the black arrows the directions in which the wave can be detected in the far field, and the dashed arrow showing destructive interference. The red and blue curves indicate electric fields with opposite polarity in x. In a, there is no metal mask and all parts of the wave may freely radiate. In b, the metal mask causes a reflection on the wave with a $\frac{\pi}{2}$ phase shift and destructively interferes with the part of the wave beneath the metal mask.

the word ‘metamaterial’ indicates that they exhibit properties beyond those found in naturally occurring materials[42]. This loose definition has been more and more applied to negative-index materials (NIMs), materials exhibiting a fully negative refractive index. Such materials were first proposed by Victor Veselago in 1967[43] and demonstrate several interesting properties such as a negative phase velocity of light, the reversal of Cherenkov radiation and invisibility to certain frequencies[44]. Metamaterials are typically comprised of an array of a large number of so-called ‘metamolecules’, structures with a subwavelength size so that incoming radiation sees a homogenous medium.

Metamaterials have been a point of interest in physics since the first demonstration of a NIM by Smith et. al in 2001[45]. The material, a composite of split-ring resonators (SRRs) and metallic rods was unique in being the first material to produce a negative magnetic response caused by a negative magnetic permeability. Interestingly, a magnetic material need not be present for the demonstration of a negative permeability[46]. Rather, the negative μ is the response of electrical currents in the SRRs oscillating in response to a changing magnetic field. These SRRs, combined with the negative ϵ from the metallic rods, produced a negative n for certain frequencies.

In their most basic design, an SRR is simply a loop of copper containing a small gap. This design allows an electrical current to flow around the ring, which as in a solenoid generates a magnetic field. Furthermore, the gap allows the build up of charge at each side, in this way acting as a capacitor. It is therefore apparent that an SRR is able to work as a small LC circuit and as such stores most of its energy as either the magnetic field generated by the current in the ring or in the electric field across the gap[44]. Also to be expected, they demonstrate a resonant frequency determined by $\omega = \frac{1}{\sqrt{LC}}$

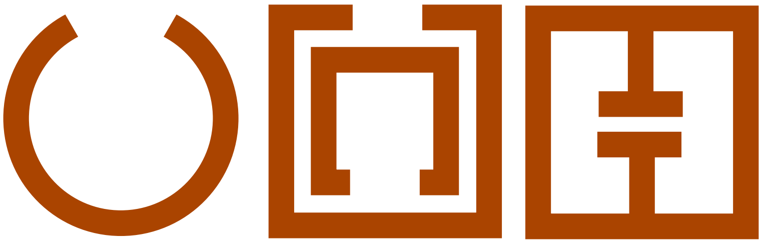

Figure 1.6: Geometry of various split ring resonators. Each contains at least one loop and at least one gap.

Split ring resonators are able to couple to an incoming EM wave if its magnetic field perpendicular to the plane of the SRR. The time-varying magnetic field of such a wave induces circular currents in the SRR according to Faraday's law. If the frequency of the incoming wave is below ω_0 then the currents induced in the SRR can keep up with the driving force produced by the wave and a positive response is achieved. If, however, the incoming wave has a frequency above ω_0, then the currents in the ring can no longer keep up with the driving force and begin to 'lag'[44]. At this point, the incoming wave sees a negative magnetic permeability. Interestingly, it is also possible to achieve a magnetic response from a split ring resonator without the necessary magnetic field. If an EM wave has **E** parallel to the SRRs line of symmetry, a magnetic response is also achieved. This is because the asymmetry of the SRR allows the electric field to drive a circular current. For this reason, this response is generally known as the electric excitation coupling to the magnetic resonance (EEMR)[47]

Microwave metamaterials were the first to be demonstrated, owing to the relative ease with which microwave radiation can be generated and the relatively large length scales on which they operate. This led, almost immediately, to the development of similar structures operating at shorter wavelengths in the THz regime.[48]

By looking at the proposed applications of metamaterials, we can further understand their current popularity. One of the first proposed applications was the 'superlens', a

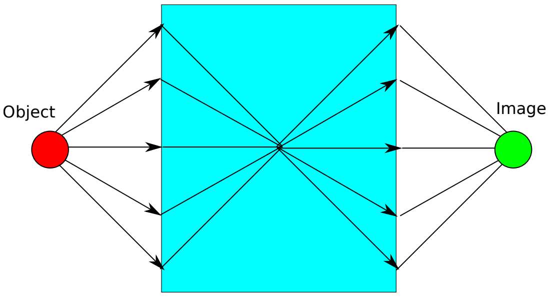

Figure 1.7: The path of light through a superlens

lens which, through a negative n is able to overcome the diffraction limit and allows for subwavelength imaging[49]. These lenses have been realised and experimentally verified at a range of frequencies, from the microwave to the high infrared. Another proposed application is that of 'invisibility cloaks'[50]. It is hoped that by tailoring metamaterials so that certain wavelengths of light flow smoothly around the metamaterial without reflection, and propagating forwards as though no obstacle had been encountered.

The focus of the metamaterial based research in this thesis is as part of a microwave antenna design. Though the notion of using SRRs to enhance a microwave antenna is nothing new, the usage of SRRs to couple an antenna to a waveguide while not in direct contact is, to our knowledge, novel. Furthermore, this microwave design incorporates mutual coupling between two types of metamaterial, SRR and 'fish-scale'. To my knowledge, this is the first time a coupling between these two designs has been demonstrated.

1.3 Thesis overview

In this thesis, I will present computational models of various emitters, both microwave and THz, and compare them to experimental results. I will utilise both finite difference and finite element methods to produce the models.

In chapter 2, I will discuss a 2D drift-diffusion model for photoexcited carriers in GaAs. The model takes in to account the change in mobilities of both carrier species when under the influence of an electric field. Furthermore, it also takes in to account the change in diffusion constant due to thermalization from electric fields. This model is then used to investigate the mechanics of the lateral photo-Dember effect. The results indicate that the mechanism may differ from previous understanding, and that the currents flowing perpendicular to the semiconductor surface are primarily responsible for the observed THz emission. I found and present that both the lateral and classical PD effect play a role to the THz EM wave generation and this is in contrast to the hypothesis presented by Mark Barnes, which suggested that the lateral currents were only responsible for the emitted radiation[41, 1].

In chapter 3, I will compare results from the computational model to results from laboratory experiments. The first experiment investigates the effect of a biasing electric field on the LPD mechanism. It was experimentally found that certain electric field strengths can either enhance or destroy the THZ emission resulting from an LPD emitter. The model gives good agreement with experimental results, showing similar amounts of destruction or enhancement when placed under the same electric fields. Secondly, I performed an experiment in which cavities of various thicknesses were introduced to the surface of various LPD emitters. By doing this, it was possible to increase the temporal width of the THz pulse, as well as introduce a free spectral range to the frequency domain.

In chapter 4, I will present a novel microwave antenna. The model was first designed and investigated using finite element modelling in COMSOL Multiphysics. The design consisted of a small antenna on the back of a coplanar wave guide (CPW). The coupling of the antenna to the CPW was shown to be improved through the introduction of SRRs in close proximity to the antenna. The sample was then fabricated, and experimental verification of enhancement of radiated emission due to the introduction of the split ring resonators was found.

Chapter 2

Modelling The Lateral Photo-Dember Effect

2.1 Introduction

The ultrafast generation and movement of carriers within a semiconductor by a femtosecond laser is known to result in the emission of a THz pulse. This is known as the photo-Dember effect[51, 39]. The radiation results from rapidly changing currents arising from the difference in mobility between the electrons and holes. Typically, the radiation emitted perpendicular to the semiconductor surface cancels out in the far field region due to the spatial symmetry of the emission profile. Thus, only emission travelling in the plane of the semiconductor surface is detected. It is possible to overcome the lack of perpendicular emission by introducing a metal mask, and illuminating an area in close proximity to the metal-semiconductor edge. Because only part of the THz pulse is reflected by the metal mask, symmetry is broken and radiation can be detected in the direction perpendicular to the sample surface. This is known as the lateral photo-Dember effect, and the currently accepted explanation for this phenomenon is given in [37, 41] and shown in Fig. 1.5.

It is known that the lateral currents arising in a PD sample create an emission profile like that shown in Fig. 1.5(a) when no metal mask is present. In the presence of a metal mask, it is posited by Barnes et. al.[1] that the lateral electric field component of the wave reflected by the metal mask undergoes a π phase shift, leading to destructive interference with the part of the wave radiating beneath the metal mask. In this way, it is believed that symmetry is broken and the pulse no longer cancels out in the far field region in the direction perpendicular to the sample surface. This is shown in Fig. 1.5(b). We aim to show, through the use of a computational model similar to that in[52], that the perpendicular currents play a much greater role in the LPD effect that the lateral currents currently believed primarily responsible for the observed THz emission.

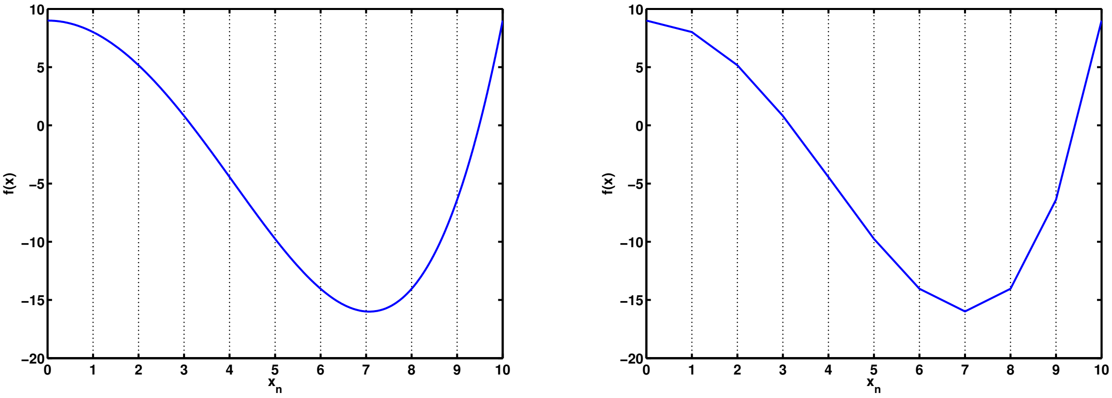

Figure 2.1: Finite difference discretization. A continuous function, shown in (a), is discretized at points x_0, x_1 etc. The corresponding discrete function is shown in (b).

2.2 Finite Difference Methods

Finite difference methods (FDMs) are a class of methods used extensively to solve sets of partial differential equations by approximating the derivatives using finite differences[53]. These approxmiations take place over a discrete grid, with solutions calulated on the nodes where the grid lines meet. An illustrative comparison between an arbitrary function and its discrete counterpart is presented in fig. 2.1. Typically, a finite difference approximation takes one of three forms; forward differences, backward differences and central differences.

Finite difference methods were chosen for this model, due to the well understood and documented finite difference algorithms for modelling the drift-diffusion dynamics and resulting radiation[52], and also for calculating the resulting far-field radiation[54]. Secondly, since the geometry of the problem consists entirely of straight lines, there is no difficulty in representing the geometry with an entirely rectangular mesh.

2.2.1 First order approximations

Let us take a function, f, imposed on a finite difference grid with a constant spacing h, and write the function $f(x_0 + h)$ as a Taylor series expansion[55].

$$f(x_0 + h) = f(x_0) + \frac{f'(x_0)}{1!}h + \frac{f^{(2)}(x_0)}{2!}h^2 + ... + \frac{f^{(n)}(x_0)}{n!}h^n \tag{2.1}$$

Let us now truncate this expression to the first derivative of f, which when divided through by h we arrive at

$$\frac{f(x_0 + h)}{h} = \frac{f(x_0)}{h} + f'(x_0) + \frac{R}{h} \tag{2.2}$$

where R refers to the remainder term which is due to the fact that the terms removed from the Taylor expansion due to truncation. Finally, assuming a negligible R, we can rearrange to get

$$f'(x_0) \approx \frac{f(x_0 + h) - f(x_0)}{h} \tag{2.3}$$

which is our forward-difference approximation for the derivative of f at x_0. It is known as the forward difference due to the two datapoints used for the calculation being the point at which the the solution is calculated and the point ahead of it in the $\hat{x}$ direction. We can produce a backward difference approximation by following the same steps for the forward difference but starting by expanding $f(x_0 - h)$ instead. This leads to the backward difference approximation of the first derivative

$$f'(x_0) \approx \frac{f(x_0) - f(x_0 - h)}{h} \tag{2.4}$$

Since both the forward and backward difference methods approximate the derivatives using only 2 nodes, these two methods are said to use a two-point stencil [56]. The errors in eqns. 2.3 and 2.4 are typically of opposite sign, meaning that greater accuracy can often be achieved by approximating the derivative by taking the average of these two expressions. This leads us to the expression

$$f'(x_0) \approx \frac{f(x_0 + h) - f(x_0 - h)}{2h} \tag{2.5}$$

This expression involves 3 nodes of the spatial grid, and is thus known as a three-point stencil.

2.2.2 Second order approximations

To reach expressions for the second derivative of f, let us start by finding first order central differences at $x_0 + \frac{h}{2}$ and $x_0 - \frac{h}{2}$. This is equivalent to solving the forward and backward finite difference expressions at x_0, and the expressions are identical to 2.3 and 2.4. We can now plug these expressions in to the central difference formula at x_0 in place of $f(x_0 + h)$ and $f(x_0 - h)$, causing us to arrive at

$$f''(x_0) \approx \frac{f(x_0 + h) - 2f(x_0) + f(x_0 - h)}{h^2} \tag{2.6}$$

which is the central difference approximation of the second derivative[57]. We can subsequently arrive at the central-difference approximation for the Laplace operator by summing eqn. 2.6 in two dimensions to arrive at

$$
\begin{aligned}
\nabla^2 f(x_0, y_0) \approx & \frac{f(x_0 + h_x, y_0) - 2f(x_0, y_0) + f(x_0 - h_x, y_0)}{h_x^2} \\
+ & \frac{f(x_0, y_0 + h_y) - 2f(x_0, y_0) + f(x_0, y_0 - h_y)}{h_y^2}
\end{aligned}
\tag{2.7}
$$

where h_x is the step size in x and h_y is the step size in y. Assuming a uniform grid where $h_x = h_y = h$, eqn. 2.7 simplifies to

$$
\nabla^2 f(x_0, y_0) \approx \frac{f(x_0 + h, y_0) + f(x_0 - h, y_0) + f(x_0, y_0 + h) + f(x_0, y_0 + h) - 4f(x_0, y_0)}{h^2}
\tag{2.8}
$$

2.3 Modelling the Drift-Diffusion equation

2.3.1 Carrier Transport

The modelling of the drift-diffusion is clearly useful for simulations involving the motion of carriers in a semiconductor.

Let us start from Fick's first law [58], from which the diffusion flux $\mathbf{J}_{diff}$ arising from a density distribution ϕ can be expressed as

$$
\mathbf{J}_{diff} = -D\nabla\phi
\tag{2.9}
$$

where D is the diffusion constant. In the case of semiconductor carrier motion, we wish to convert the flux $\mathbf{J}_{diff}$ to the current density$\mathbf{j}_{diff}$. In this case, eqn. 2.9 becomes

$$
\mathbf{j}_{diff} = -qD\nabla n
\tag{2.10}
$$

we can replace ϕ with qn, where q is the carrier charge and n is the charge carrier density. Since the carriers in our model carry an electric charge (holes and electrons), we must also consider drift, which when combined with eqn. 2.9 gives us [59]

$$
\mathbf{j} = q(\mu n\mathbf{E} + D\nabla n)
\tag{2.11}
$$

where μ is mobility. We can relate this current to the change in carrier desnity by Fick's second law [60]

$$\frac{\delta n}{\delta t} = \frac{1}{q}\nabla \cdot \mathbf{j} \tag{2.12}$$

Let us further assume two functions which we will not define for now, G and R, which represent carrier creation and recombination respectively. Let us also substitute **j** in eqn. 2.12 with eqn. 2.11 to give us the equation

$$\frac{\delta n}{\delta t} = \mu\nabla \cdot (n\mathbf{E}) + D\Delta n + G + R \tag{2.13}$$

where it is assumed that G has a positive value and R has a negative one. The diffusion part of this equation is easily calculable given the carrier distribution n, but the drift part requires the calculation of **E** at all points inside the simulation. For a calculation taking in the domain $\Omega \in \mathbb{R}^2$, the electric field acting on a point **r** is given by [61]

$$\vec{E}(\mathbf{r}) = \int_\Omega \frac{Q(\mathbf{r}')}{2\pi\epsilon(\mathbf{r}' - \mathbf{r})} dr' \tag{2.14}$$

We will solve this problem numerically with a finite-difference approach. Let us take our domain Ω and discretize it with a grid of M nodes in the $\hat{x}$ direction and N nodes in the $\hat{y}$ direction which we will label as $x_0, x_1...x_M$ and $y_0, y_1...y_N$. We assume that the distance between nodes is the same in both directions, which we will denote h. While the carrier densities are stored at the nodes of the grid line, the current is calculated between the nodes, as shown in fig. 2.2. This setup allows the currents to be calulated using a central difference method, using the two neighbouring carrier concentrations. This allows eqn. 2.11 to be first calculated in the spaces between the nodes, then by plugging this value in to 2.12, the carrier concentrations located on the nodes may be updated. From here on, we will denote sampled functions with subscript coordinates so for example $\mathbf{E}_{ij}$ denotes the electric field sampled at the node located at (x_i, y_j). Time is also discretised.

The preceding set of equations give us the basis of the drift-diffusion model. It can be seen that this set of equations ignores the underlying band structure of the semiconductor, instead focusing on bulk transport properties defined by μ and D. Furthermore, it assumes a constant carrier temperature throughout the sample. It is possible to extend the validity of the drift-diffusion model by introducing field-dependent transport properties through $\mu(\mathbf{E})$ and $D(\mathbf{E})$, the values of which are taken from Monte Carlo models. Even through the introduction of these field-dependent variables, however, the drift-diffusion model is unable to account for the effects of velocity overshoot. It is therefore reasonable to assume that the drift-diffusion model is far more accurate in cases of low injection than high injection.

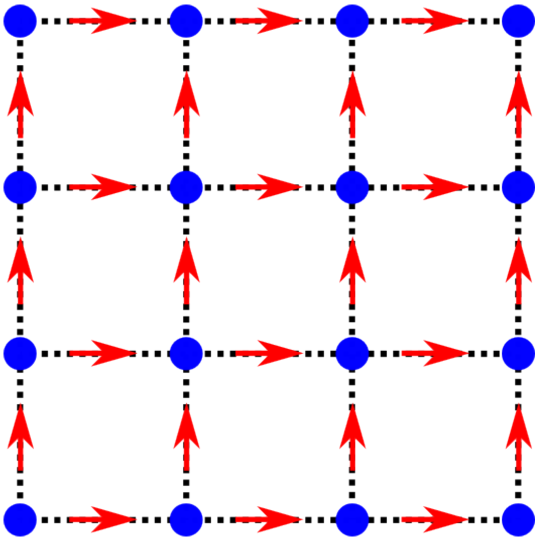

Figure 2.2: The placement of the calulated densities (blue dots) and calculated currents (red arrows). The dashed black lines represent the mesh.

An alternative method is presented in the Hydrodynamic model[62, 63]. While the drift diffusion model assumes bulk characteristics for all carriers, the hydrodynamic model instead models each individual valley in which carriers may be found[64]. The hydrodynamic model utilises three types of conservation in order to model velocity overshoot, particle conservation (as in the DD model), momentum conservation and energy conservation. This requires the discovery of momentum and energy relaxation rates at different fields which can be fed in to the model. These rates, along with other parameters, must be taken from a Monte Carlo[65].

Despite the advantages of the hydrodynamic model, in this thesis I will use the drift-diffusion model. Firstly, its relative simplicity makes it easy to implement and allows calculations to be performed in shorter time. Secondly, since in the drift-diffusion model the currents are solved directly, it allows for the results of the transport model to be fed directly in to the FDTD model. Furthermore, while for the hydrodynamic model a series of Monte Carlo simulations must first be run, no such preliminary investigations are required for the drift diffusion model.

2.3.2 Carrier Generation and Recombination

In order to correctly model the drift and diffusion of carriers within a semiconductor, it is necessary to describe the processes by which charge carriers are created and annihilated. We will look at photogeneration as the primary source of charge carriers, while the types of recombination covered in this section are Shockley-Read-Hall, Auger, surface and radiative.

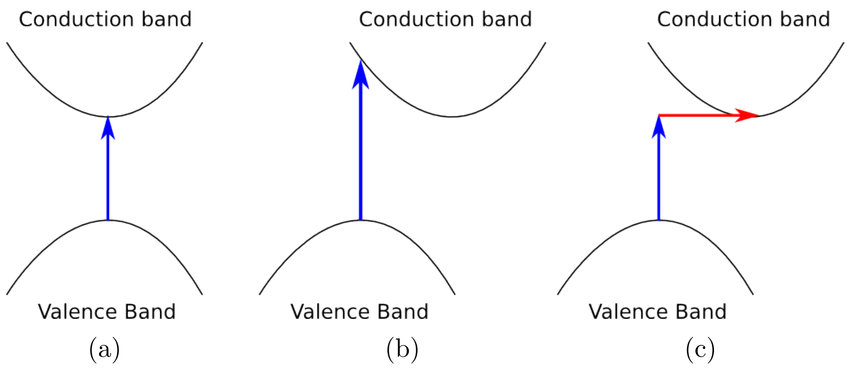

Figure 2.3: Direct and indirect band transitions in semiconductors. The blue lines represent a change in energy of an electron due to photon absorption, while the red line represents a change in momentum due to phonon absorption. (a) shows a direct transition in a direct semiconductor, (b) shows a direct transition in an indirect semiconductor and (c) shows an indirect transition in an indirect semiconductor.

2.3.2.1 Photogeneration

When incoming light has an energy greater than the band gap of the semiconductor, it may be absorbed by an electron in the valence band which is then excited in to the conduction band[66]. The manner in which this likely occours is dependent on the band structure of the semiconductor. For direct band gap semiconductors, such as GaAs or InP this process is relatively straightforward. In such structures, the trough of the conduction band exists at the same k as the valence band and a direct transition is probable (fig. 2.3(a)). However, for indirect band gap semiconductors, these two locations exist at different k. This means the probability of a direct transition may be low if the energy difference between the two bands at a specific k is large (fig. 2.3(b)). However, if the excited electron already has momentum, it may take on a different k as it transitions between the bands, allowing for an indirect transition to occour (fig. 2.3(c))[67]. The rate of photogeneration is given by[52]

$$G = \frac{I\lambda\alpha}{hc} \tag{2.15}$$

where I is the laser intensity, λ is the laser wavelength and α is the absorption coefficient. The wavelength of the laser used both in experimentation and the model is 800 nm, while α is $1 \times 10^{-}6$ for GaAs[52].

2.3.2.2 Radiative Recombination

Radiative recombination (fig. 2.4, left), or band-to-band recombination is essentially the reverse of photogeneration. Any electron excited to the conduction band carries a probability of spontaneously relaxing down in to the valence band. As it does so, it

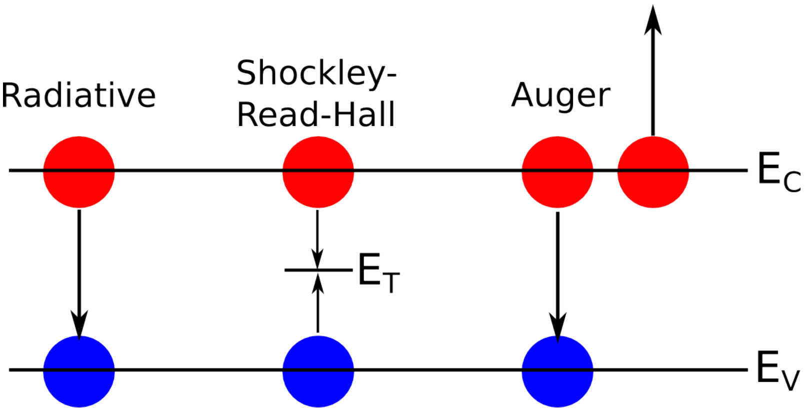

Figure 2.4: A representation of the three primary forms of recombination in bulk semiconductors. Radiative recombination involves a conduction electron moving down to the valence band and recombining with a hole. Shockley-Read-Hall recombination involves a carrier of each species falling in to a trap site, while Auger recombination involves the transferral of energy to a third carrier.

annihilates a hole and releases a photon containing the energy lost in the relaxation process[68]. In the same manner as photogeneration, this may be a direct or indirect process. The rate of radiative recombination in a semiconductor is given by[69]

$$R_{rad} = B_{rad}(np - n_i^2) \tag{2.16}$$

where B_{rad} is a material-specific constant and n_i is the intrinsic carrier concentration, which for GaAs is $9 \times 10^6 cm^{-3}$[52]. Since this process requires the presence of both an electron and a hole, it is easy to understand why it has a dependency on np.

2.3.2.3 Shockley-Read-Hall Recombination

Shockley-Read-Hall (SRH) recombination (fig. 2.4, centre) occurs due to the presence of impurities or crystal defects in a semiconductor. Such defects give rise to defect levels; energy levels that exist between the allowed bands. Such traps cause the recombination of carriers through a two stage process. Firstly, either an electron in the conduction band or a hole in the valence band moves to the trap level. For electrons, this causes the transfer of excess energy ($E_C - E_T$) to the crystal lattice in the form of a phonon[70]. For holes, this requires the absorption of the required amount of energy ($E_T - E_C$). These two processes are known as electron or hole capture. Secondly, a carrier of the other species must also move in to the trap state, causing the annihilation of both carriers. Furthermore, it is possible for a trapped electron to move back from the trap state to the conduction band (or a hole to the valence band), known as electron or hole emission[71]. Thus, there is a possibility that a trapped carrier will leave the trap before annihilation from the opposite species. Assuming a quasi-stationary system, the rate of recombination due to the SRH process is given by[72]

$$R_{SRH} = \frac{np - n_i^2}{\tau_p(n + n_1) + \tau_e(p + p_1)} \tag{2.17}$$

where τ_e and τ_p represent the electron and hole lifetimes and for GaAs $tau_e = 0.3$ ps and $tau_p = 0.4$ ps[52]. n_1 and p_1 give a dependency on the energy level of the trap, E_t by

$$n_1 = N_c e^{(E_t - E_c/k_b T)} \tag{2.18}$$

$$p_1 = N_v e^{(E_v - E_t/k_b T)} \tag{2.19}$$

where E_c and E_v are the conduction band and valence band energy levels respectively, N_c and N_V represent the density of states in each band. For GaAs, $n_1 = p_1 = 4.5 \times 10^6 cm^{-3}$[52].

2.3.2.4 Auger Recombination

Auger recombination (fig. 2.4, right) involves three charge carriers. Unlike radiative recombination, where the excess energy of an electron relaxing in to the valence band is given off as a photon, Auger recombination involves the transferral of energy to a third carrier. This third carrier then loses its excess energy through collisons with the lattice[73]. Like radiative recombination, this may also occour as a direct or indirect process [74]. Two types of Auger recombination are possible, electron-electron-hole, or hole-hole-electron. The recombination rates for electrons and holes are given by[75]

$$R^n_{aug} = B^n_{aug} n^2 p \tag{2.20}$$

$$R^p_{aug} = B^p_{aug} n p^2 \tag{2.21}$$

Again, B^n_{aug} and B^p_{aug} are material-specific constants. For GaAs, $B^n_{aug} = B^p_{aug} = 7 \times 10^{-30} cm^6 s^{-1}$.

2.3.2.5 Surface Recombination

The surface of a semiconductor typically contains a large number of traps due to the termination of the lattice and impurities from exposure during the fabrication process. For this reason, there are large number of trapped states at the surface of a semiconductor. Thus, surface recombination occurs by a similar process to SRH recombination; charge carriers are trapped in surface states and may be annihilated by the opposite species of carrier if they do not escape from the trap state[76]. Surface recombination is typically characterised by a surface recombination velocity by which the recombination rate can described as a flux leaving the surface

$$J_n = v_s(n - n_i) \tag{2.22}$$

In reality there are no charge carriers, and by extension no current leaving the semiconductor surface. However, this flux is still useful as it provides a convenient manner in which to calculate the loss of carriers at the semiconductor surface.

2.3.3 Calculating the Electric Field

In order to calculate $\frac{\delta n}{\delta t}$ at each node we must seperately sample n, **E**, R and G. Assuming we know the number of holes and electrons in the system at a particular time, the simplest method by which we can calulate the electric field, and thus **E**, is by using the finite difference version of eqn. 2.14

$$\mathbf{E}_{ij} = \sum_{k=0}^{M-1}{}' \sum_{l=0}^{N-1}{}' q \frac{n^h_{kl} - n^e_{kl}}{2\pi\epsilon\sqrt{(x_k - x_i)^2 + (y_l - y_j)^2}^2} \hat{r}_{ijkl} \tag{2.23}$$

with n^h being the number of holes, n^e being the number of electrons and $\hat{r}_{ijkl}$ being the direction from (x_i, y_j) to (x_k, y_l). The primed sums ensure we avoid dividing by zero when $i = k$ and $j = l$. In spite of its simplicity, the usage of eqn. 2.23 for large multidimensional geometries requires a large amount of physical memory, since at each node in the mesh the effects of the carrier concentrations at all other mesh points must be directly calculated. In practice, this means that the increase in RAM required to perform such a calculation scales proportionally to N^2, where N is the number of mesh points in the simulation.

In order to work around this computational limit, it is apparent we need a method seperate from 2.23, which we find in the Fourier transform method (FTM). The FTM allows us to solve Poisson's equation for the electric potential, ψ

$$\nabla^2\psi = \frac{\rho}{\epsilon_0\epsilon_r} \tag{2.24}$$

without the need to directly integrate it, as we do must with eqn. 2.23. Instead, as the name implies, we first calculate the Fourier transform of the right hand side of eqn.

2.24 to give us $\hat{\rho}$. Taking the expression for the inverse Fourier transform function for an arbitrary function u[77]

$$u_{jk} = \frac{1}{MN} \sum_{m=0}^{M-1} \sum_{n=0}^{N-1} \hat{u}_{mn} e^{-2\pi ijm/M} e^{-2\pi ikn/N} \tag{2.25}$$

we can gain expressions for ψ and ρ in terms of their Fourier transforms. Plugging both values in to eqn. 2.8 and making use of the uniqueness of a Fourier series[78], we find

$$\hat{\psi}_{mn} = \frac{h^2 \hat{\rho}_{mn}}{e^{2\pi im/M} + e^{-2\pi im/M} + e^{2\pi in/N} + e^{-2\pi in/N} - 4} \tag{2.26}$$

or, alternatively

$$\hat{\psi}_{mn} = \frac{h^2 \hat{\rho}_{mn}}{2(cos\frac{2\pi m}{M} + cos\frac{2\pi n}{N} - 2)} \tag{2.27}$$

from which we can take the inverse Fourier transform to find ψ. From the two sum terms in the inverse Fourier (eqn. 2.25) and their counterparts in the regular Fourier transform it may appear as though no computational time is saved when compared with eqn. 2.23. This is true for the discrete Fourier transform algorithm, for which the number of arithmetic operations required on N points is proportional to N^2. However, since the number of arithmetic operations required for the fast Fourier transform is proportional to $N\log(N)$[79], using the FFT approach makes this calculation significantly quicker. Since the Fourier transform satisfies the condition

$$u_{mn} = u_{m+M,n} = u_{m,n+N} \tag{2.28}$$

this method solves eqn. 2.24 with periodic boundary conditions. We can satisfy Dirichlet and Neumann boundary conditions by applying the same process with the sine or cosine Fourier transforms respectively[77]. For these transformations, eqn. 2.27 becomes

$$\hat{\psi}_{mn} = \frac{h^2 \hat{\rho}_{mn}}{2(cos\frac{\pi m}{M} + cos\frac{\pi n}{N} - 2)} \tag{2.29}$$

after which we can apply the appropriate inverse Fourier transform.

2.3.4 The Scharfetter-Gummel discretization

It is important to correctly choose the continuity scheme used to approximate the currents and by extension $\frac{\delta n}{\delta t}$. While on the surface, it seems simplistic enough to simply choose the spatial average of the two densities either side of the current. Such a scheme would lead to an explicit continuity equation for electrons as

$$\frac{\delta n}{\delta t} = \frac{n_{i,j}^{k} - n_{i,j}^{k-1}}{\Delta t} = \nabla \cdot \mathbf{J}_{i,j}^{k-1} \tag{2.30}$$

with the k representing the time step and the current density defined as

$$J_{x\,i+\frac{1}{2},j} = q(D\frac{\delta n_{i+\frac{1}{2},j}}{\delta x} - n_{i+\frac{1}{2},j}\mu\frac{\delta \psi}{\delta x}) \tag{2.31}$$

or

$$J_{x\,i+\frac{1}{2},j} = q\frac{(D(n_{i+1,j} - n_{i,j}) - \frac{n_{i+1,j}+n_{i,j}}{2}\mu(\psi_{i+1,j} - \psi_{i,j}))}{\Delta x} \tag{2.32}$$

While this scheme is appropriate for many applications, it can break down and lead to substantial errors in regions with a strong electric field. To demonstrate, let us assume a situation in which there are carriers present but no current flow. From eqns. 2.11, 2.32 and the Einstein relationship, we can see that this requires

$$\psi_{i+1,j} - \psi i, j = \frac{2k_bT(n_{i+1,j} - n_{i,j})}{q(n_{i+1,j} + n_{i,j})} \tag{2.33}$$

If we further assume that there are no carriers in the $n_{i,j}$ node, then we reach the condition

$$\psi_{i+1,j} - \psi i, j \leq \frac{2k_bT}{q} \tag{2.34}$$

In other words, if the potential difference between two neighbouring nodes is greater than $\frac{2k_bT}{q}$ V, then a negative density n will be produced. One way to overcome this limit to ensure the mesh size is small enough, however for many semiconductor systems this size and its associated timestep lead to extremely long solution times. It is possible to overcome this limit using the Scharfetter-Gummel discretization.

The Scharfetter-Gummel discretization method instead assumes that the carrier densities follow an exponential variation between mesh points as opposed to a linear one[80]. Let us start with the condition that **E** and **J** are constant between neighbouring nodes. Starting from eqn. 2.11 in 1D, we have

$$\frac{\delta n}{\delta x} = -\frac{\mu\mathbf{E}}{D}n + \frac{\mathbf{J}}{qD} = an + \frac{\mathbf{J}}{b} \tag{2.35}$$

which, after rearranging and integrating, gives

$$n + \frac{\mathbf{J}}{ab} = e^{ax+c} \tag{2.36}$$

Hence,

$$\frac{n_{i+1,j} + \frac{J_{i+\frac{1}{2},j}}{ab}}{n_{i,j} + \frac{J_{i+\frac{1}{2},j}}{ab}} = e^{ah} \tag{2.37}$$

which can be rearranged for J to give

$$J_{i+\frac{1}{2}} = \frac{ab}{e^{ah} - 1}(n_{i+1,j} - n_i e^{ah}) \tag{2.38}$$

or

$$J_{i+\frac{1}{2}} = \frac{b}{h}[B(ah)n_{i+1,j} - B(-ah)n_{i,j}] \tag{2.39}$$

For the purposes of our simulations, R is dependent on n^e and n^h and G is dependent on x, y, and t. Therefore, we need only the already sampled carrier distributions to calculate R, and G is already defined and sampled before the simulation starts.

Once we know all the quantities required for the solution of eqn. 2.13 for both holes and electrons, we require a method to progress the model forward in time. Arguably the simplest method to understand is Euler's method, which we will discuss here. If we have a function $f(t)$ from which $f'(t)$ can be calculated and $f(t_0)$ is known, then we can select a value for dt appropriate to the dynamic timescale of the system we are modelling. If dt is small enough, then a valid approximation of $f(t+dt)$ from $f(t)$ is $f(t+dt) \approx f(t) + f'(t) * dt$. In this case $f'(t)$ is equal to eqn. 2.13, which we calculate at each timestep and then add to the values of n^e and n^h for that timestep to get their values for the next timestep.

2.4 The Finite Difference Time Domain Method

2.4.1 Introduction and Setting Up The Problem

The Finite-Difference Time Domain (FDTD) was first proposed by Yee in 1966[81], and remains an extremely popular choice for the solution of dynamic electromagnetic problems. The FDTD method applies a discrete grid in t as well as x, with dt remaining constant throughout the problem.

Maxwell's equations for electromagnetism when allowing for fictitious magnetic charges are as follows[82]

$$\nabla \cdot \mathbf{E} = \frac{\rho_e}{\epsilon} \tag{2.40}$$

$$\nabla \cdot \mathbf{B} = \rho_m \tag{2.41}$$

$$\nabla \times \mathbf{E} = -(\frac{\delta \mathbf{B}}{\delta t} + \mathbf{J_m}) \tag{2.42}$$

$$\nabla \times \mathbf{B} = \mu(\epsilon\frac{\delta \mathbf{E}}{\delta t} + \mathbf{J}) \tag{2.43}$$

Equations 2.40 and 2.43 are as expected, but 2.41 and 2.42 contain the unfamiliar terms ρ_m and J_m, which are the magnetic charge density and magnetic current respectively. Though these two terms are always equal to zero in the real world, they can nonetheless be useful tools in the world of computational electrodynamics, as we will see later.

For the FDTD algorithm, we must consider eqns. 2.42 and 2.43, since these are the two equations that describe the change in the fields with respect to time. The revelation of Yee's algorithm was to offset the nodes at which the **E** and **H** fields are evaluated. Rather than allowing the E and H nodes to occupy the same space, they are instead staggered in all spatial dimensions. for example, for a 1D grid with E field nodes located at x_0, x_1, x_2 etc. the H field nodes will be located at $x_0 + \frac{dx}{2}, x_1 + \frac{dx}{2}, x_2 + \frac{dx}{2}$ etc. Thus, when we wish to evaluate eqn. 2.42 or 2.43, we can calulate the time derivative of any node by evaluating the cross product of only the two neighbouring nodes of the opposite type. Furthermore, the time at which each type of node is evaluated is staggered as well, meaning that if the **E** nodes are evaluated at times t_0, t_1, t_2 etc. then the **H** field nodes are evaluated at times $t_0 + \frac{dt}{2}, t_1 + \frac{dt}{2}, t_2 + \frac{dt}{2}$ etc. This scheme is shown in Fig. 2.5. This means that the FDTD method is a central difference method in both time and space.

Let us assume a one dimensional case in which the electric field has only a $\hat{z}$-component. We can rewrite eqn. 2.42 as

$$-\mu\frac{\delta \mathbf{H}}{\delta t} = \begin{vmatrix} \hat{x} & \hat{y} & \hat{z} \\ \frac{\delta}{\delta x} & 0 & 0 \\ 0 & 0 & E_z \end{vmatrix} \tag{2.44}$$

from which we can see that **H** will be time-varying in the $\hat{y}$ direction. Similar to eqn. 2.45, we can rewrite eqn. 2.43 as

$$\epsilon\frac{\delta \mathbf{E}}{\delta t} = \begin{vmatrix} \hat{x} & \hat{y} & \hat{z} \\ \frac{\delta}{\delta x} & 0 & 0 \\ 0 & H_y & 0 \end{vmatrix} \tag{2.45}$$

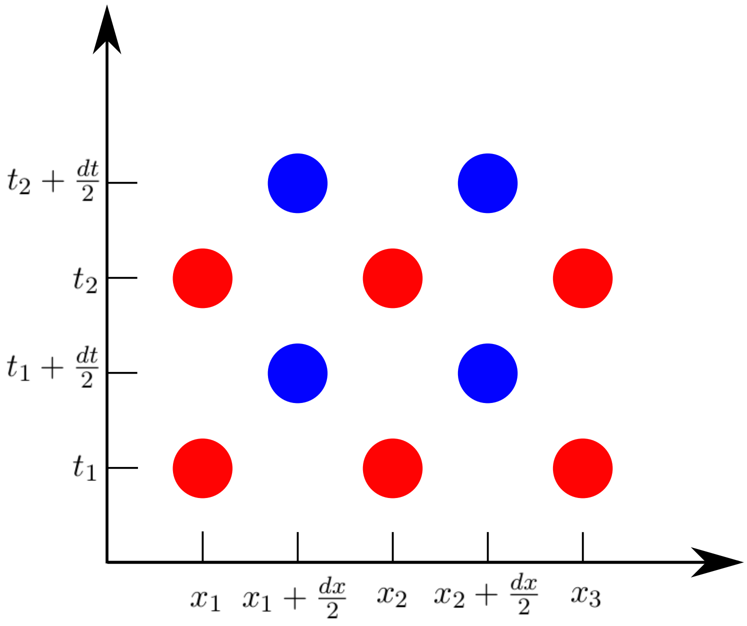

Figure 2.5: Arrangement of a 1D FDTD problem in time and space. The red dots represent the electric field nodes while the blue dots represent the magnetic field nodes.

When performing FDTD simulations in two dimensions, two possible arrangements of the electric and magnetic field nodes are possible. These two configurations are commonly known as the transverse magnetic (TM) or the transverse electric (TE) case[83]. In the transverse electric case, we allow the electric field to have components in both x and y, which according to eqn. 2.42 will only allow a time varying magnetic field in the z-direction. Similarly, if we allow the magnetic field to contain both x and y components then it is the electric field that is restircted to z. Furthermore, whichever field has two components has these two components offset from one another. This configuration is shown for the TE case in 2.6.

So, for the TE configuration, eqns. 2.42 and 2.43 would reduce to the scalar equations

$$\frac{\delta E_x}{\delta t} = \frac{\delta H_z}{\delta y} - J_x \tag{2.46}$$

$$\frac{\delta E_y}{\delta t} = -\frac{\delta H_z}{\delta x} - J_y \tag{2.47}$$

$$\frac{\delta H_z}{\delta t} = \frac{\delta E_x}{\delta y} - \frac{\delta E_y}{\delta x} + J_m \tag{2.48}$$

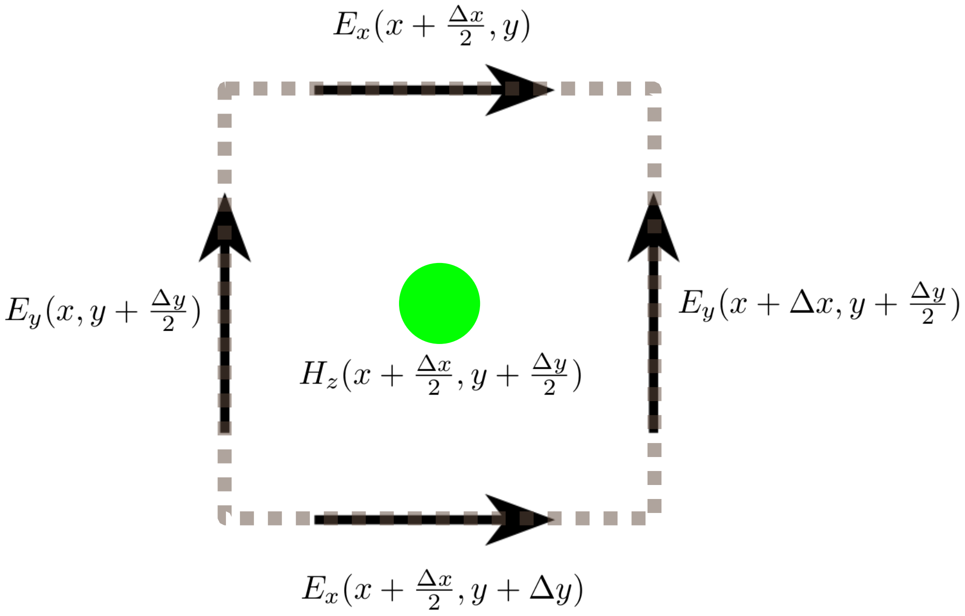

Figure 2.6: Arrangement the Yee cell for the 2D TE case. For the TM case, the green dot would represent E_z and the arrows would represent the different components of H.

2.4.2 Boundary Conditions

2.4.2.1 Perfect Electric Conductors

Perfect electric conductors (PECs) are an extremely useful tool for modelling electromagnetic systems. A PEC is an idealized material exhibiting zero resistivity. Although PECs do not exist in nature, it is often helpful to utilise them when the electrical resistance of a material is negligible compared to the other effects of the system. For instance, in a model investigating the scattering of a wave from a metallic object, by defining the edge of the object as a PEC we negate the need to calculate the fields inside the object, as they will remain at zero[84]. A PEC is easily realised in an FDTD simulation. Since any electric field on its boundary will immediately be opposed by a current acting opposite to it, we can define our perfect electric conductor by setting the update equations associated with its nodes to zero.

2.4.2.2 Absorbing Boundary Conditions

In the simulations in this thesis, 2nd order Mur absorbing boundary conditions (ABCs) were used. These act by forcing a forward propagating condition on a wave incident on the boundary. Effectively this means that the wave sees no boundary and will freely radiate, but in reality there will be small errors due to the discretisation of the problem. To implement these boundary conditions, we are required to store information about the fields just outside the boundaries at previous timesteps. Because of this, the boundaries are able to ‘look back’ and apply the boundary conditions based on what they expect to arrive. This implemented using the following equation for the electric field on the boundary $x = 0$[85]

$$E_{0,i}^{n+1} = -E_{1,i}^{n-1} + \frac{u_s - 1}{u_s + 1}(E_{1,i}^{n+1} + E_{0,i}^{n-1}) + \frac{1}{u_s + 1}(2 + \frac{u_s^2}{2} d_y^2)(E_{1,i}^{n} + E_{0,i}^{n}) \tag{2.49}$$

2.4.3 Far-Field Analysis

Far field analysis is an extremely useful tool when we are concerned with the fields at a point in space far beyond the domain of the simulation. If the magnitude of the distance we are interested in is even one order higher than the size of the simulation, in a two dimensional simulation we would experience an increase in the time required to arrive at a solution by 10000%. For distances three orders of magnitude higher, a simulation that previously took 1 second to run would now take over 11 days. Obviously if we wish to determine these values a method other than simply making the simulation larger is needed.

2.4.3.1 Love’s Equivalence Principle

The first step to far field analysis is to set the problem up in a simple manner. Let us define two regions of space. The first, region A, contains all sources and scatterers. Outside of region A is region B which is entirely made of free space. Separating these regions is a boundary which is defined by its normal pointing from region A to region B. Such a problem is shown in Fig. 2.7.

It is possible to recreate the fields on this boundary through the use of the equivalence principle, which states that there exists certain electric and magnetic current sources which will reproduce these fields. These currents are given by

$$J_e = \hat{n} \times (\mathbf{H}_B - \mathbf{H}_A) \tag{2.50}$$

$$J_m = -\hat{n} \times (\mathbf{E}_B - \mathbf{E}_A) \tag{2.51}$$

These equivalent currents will produce the same outwards propagating waves on the boundary as the original problem[86]. However, they will also produce erroneous inward propagating waves. Since we are not concerned with the fields within region A, we can choose to set these to zero by setting to zero any fields in region A in eqns. 2.50 and 2.52. We then get the equivalent currents

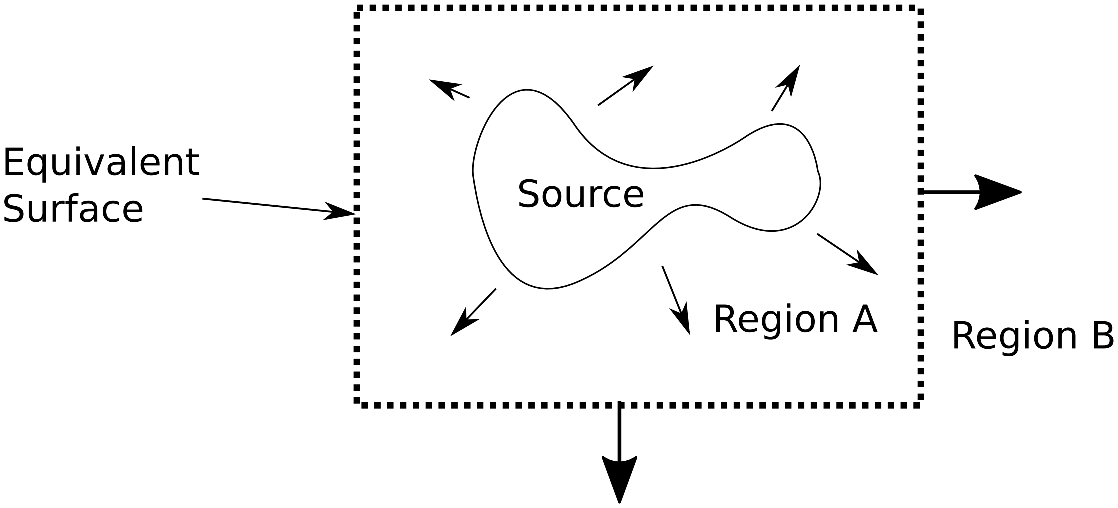

Figure 2.7: Love's equivalemce principle. Using equations 2.50 and 2.53, it is possible to recreate the fields external to the equivalent surface by applying the derived currents to the surface.

$$J_e = \hat{n} \times \mathbf{H}_B \tag{2.52}$$

$$J_m = -\hat{n} \times \mathbf{E}_B \tag{2.53}$$

which will propagate the correct fields outwardly but the fields within region A will remain at zero.

2.4.3.2 The far-field algorithm

There are many different algorithms for calculating the far field for a given set of magnetic an electric currents. In this thesis I will use the work of Garcia et al[54]. The derivation of the algorith is rather complex and involved, so in this thesis we will skip the derivation and simply cover how to apply the final algorithm. Firstly though, we must define some variables. The 'field point' represents the location of the far field we are trying to find, and the 'source point' is some point along the equivalent surface from whose contriobution to the far field we are finding. We define three vectors; $\boldsymbol{\rho}$, $\boldsymbol{\rho'}$ and $\mathbf{P}$ which are the field point position vector, the source point position vector and the vector from the source point to the field point respectively. These vectors are shown in Fig. 2.8

The far field profile at time t is computed with the equation

$$\mathbf{H}^{far}(\boldsymbol{\rho}, t) = -\frac{1}{2\pi\sqrt{2}\sqrt{\rho}} \int_{L_a} dl' \times \int_{t'=-\infty}^{t'=t-P/c} \frac{\delta_{t'}\mathbf{J}_m(\boldsymbol{\rho}, t')/Z_0 - \delta_{t'}\mathbf{J}_e(\boldsymbol{\rho}, t') \times \hat{\rho}}{\sqrt{c(t-t') - P}} \tag{2.54}$$

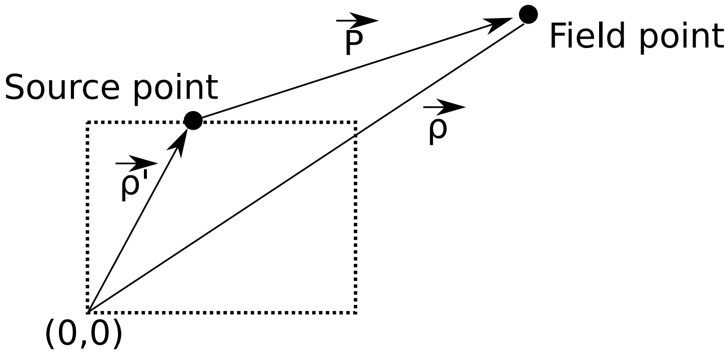

Figure 2.8: A visualisation of the equivalent surface and the associated vectors used in the far-field calculation.

The spatial integral can easily be numerically calculated using the trapezoidal rule, but the time integral is unbounded when t'. For this reason we split it in to two parts. With $t_1 = t - P/c$ and the numerator expressed as $f(t')$ and taking the lower limit of the ime integral as 0 as there is no illumination before this

$$\int_{t'=0}^{t'=t_1} \frac{f(t')}{\sqrt{c(t_1-t')}} dt' = \int_{t'=0}^{t'=t_1-4\Delta t} \frac{f(t')}{\sqrt{c(t_1-t')}} dt' + \int_{t'=t_1-4\Delta t}^{t'=t_1} \frac{P(t')}{\sqrt{c(t-t')}} dt' \quad (2.55)$$

where $P(t')$ is an interpolating polynomial of $f(t')$ taken from the final five time increments. We can then solve the first integral in 2.55 using the trapezoidal rule while the second can be calculated analytically.

2.5 Modelling the Lateral Photo-Dember Effect

The drift diffusion model is set up as described in section 2.3. By then aligning the FDTD **E** nodes shown in fig. 2.6 with the DD current nodes shown in fig 2.2, it is possible to directly feed the electric currents calculated by the DD solver in to the FDTD algorithm when **E** is updated. As such, the spatial and temporal steps the same for both solvers. This arrangement of the two meshes can be seen in fig. 2.9.

For an unmasked Photo-Dember emitter modelled in two dimensions, G must have a gaussian profile in both x, and t. In y, the pulse is assumed to follow the Beer-Lambert law and therefore exponentially decreases in intensity through the depth of the semiconductor. In our geometry, we define $y > 0$ as air and $y \leq 0$ as semiconductor and the laser intensity to be greatest at $x = 0$. For the Photo-Dember effect in 2D, G is therefore defined as

$$G(x, y \leq 0, t) = k_n \exp\Big(-\frac{2x^2}{w^2} - \alpha y - \frac{(t-t_0)^2}{w_t^2}\Big) \quad (2.56)$$

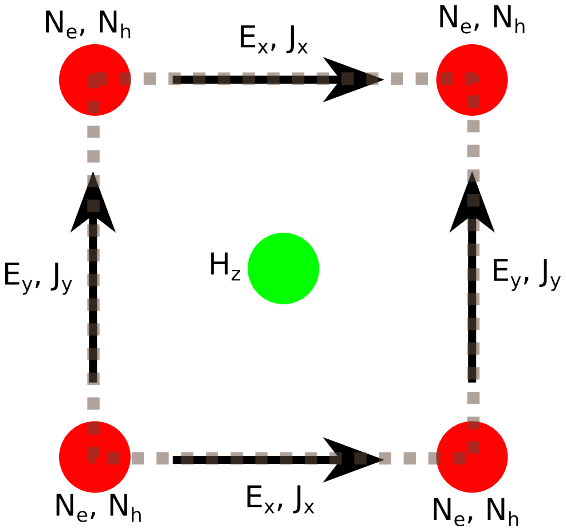

Figure 2.9: The alignment of the DD solver current and carrier densities with respect to the FDTD grid. The DD and FDTD currents are located in the same location, while the carrier density nodes are staggerred compared to the FDTD magnetic field nodes.

where k_n is a constant relating the profile to the number of generated carriers, w is the spatial pulse width, t_0 is the time at which the pulse reaches peak power and w_t is the temporal pulse width. For an LPD emitter, we would expect this profile on the unmasked ($x < 0$) side only. We cannot reasonably set $G(x > 0, y, t)$ to be zero everywhere, as this would create a dramatic discontinuity in charge carriers at the mask edge. Furthermore, we would physically expect a small amount of diffraction to excite carriers under the metal mask. For this reason, we also define $G(x > 0, y < 0, t)$

$$G(x > 0, y \leq 0, t) = \exp\Big(- \frac{2x^2}{(5 \times 10^{-7})^2} - \alpha y - \frac{(t - t_0)^2}{w_t^2}\Big) \tag{2.57}$$

For the drift diffusion equation, the air-semiconductor boundary condition is[52]

$$\frac{\delta n}{\delta \hat{n}} = 0; \tag{2.58}$$

$$\frac{\delta p}{\delta \hat{n}} = 0; \tag{2.59}$$

where $\hat{n}$ is a vector perpendicular to the air-semiconductor boundary pointing out of the semiconductor.

For the FDTD algorithm, we define a perfect electric conductor (PEC) to act as the metal mask. All boundaries in the FDTD simulation are defined as second order mur absorbing boundary conditions (ABCs).

2.5.1 1D Diffusion Model in x

Firstly, I present a one-dimensional model to compare with [1]. A 1D drift-diffusion equation is solved for a row of carriers 1 μm below and running parallel to the semiconductor surface. The currents are then fed in to a 2D FDTD model and the fields allowed to propagate. The equations are solved using the parameters for LT-GaAs. The generation term was given a temporal pulse width of 100 fs and a spatial pulse width of 10 μm with peak intensity of 1×10^{11} occurring at 500 fs. Though this setup is similar to the model used by Barnes et. al, it differs in both in the fact that I use the FDTD method rather than finite-element method, and also in the description of the carrier dynamics. Firstly, the DD algorithm used by Barnes et. al. assumed constant carrier mobilities. While applicable to the low field region, this assumption fails to take in to account high field effects on the mobility and diffusion constant. For this reason, I fit the mobility to [87], which is calculated based on the electric potential at each time step. The resulting mobilities and drift velocities for different field values used in the simulation are shown in figs 2.10 and 2.11. Similarly, I have also fitted a field dependent electron diffusion constant according to [88] shown in fig. 2.12, which [1] derived from the Einstein relationship between D and μ. Here, it is assumed that any variation in these constants depend only on the longitudinal electric field. Since the hole diffusion constant varies little with increasing electric field, it is assumed to be constant. One final and important consideration when comparing my results to those of Barnes. et. al. is their assumption that k_n is arbitrary. In fact, while the diffusion current increases linearly proportional to n, drift current increases proportionally to n^2. It is likely that this is the reason that Barnes reports a negligible drift current, which I find to be untrue. Nevertheless, a diffusion only model does allow us a simplified understanding of the carrier dynamics. For this reason, in the one-dimensional model the drift term was removed, and D and μ were taken as their zero field values.

Shown in fig 2.13 is the time evolution evolution of the current density. This shows relatively good agreement with Barnes at. al, though one obvious difference is the sharp decrease in local current density at the metal mask edge, which I find to be due to the Shockley-Read-Hall mechanism. To demonstrate this, I have run a model in which the SRH term is the same as that in [1]. I find that, under this assumption, the model gives good agreement with Barnes as shown in fig 2.14. The difference between the two results due to the definition of the SRH mechanism can be easily understood. The definition used by Barnes. et. al. assumes that the fast trapping of a carrier species depends only on the local density for that species, eqn. 2.17 assumes a dependence on both species. This second asssumption is reasonable, because while electrons can easily be trapped without the presence of holes, a hole must also be trapped for recombination to occour before the electron is released. The dip in the current in fig. 2.13 is due to the low mobility of holes compared to elctrons. This can be understood if we examine the evolution of the system with the SRH term removed. In essence, this means the model

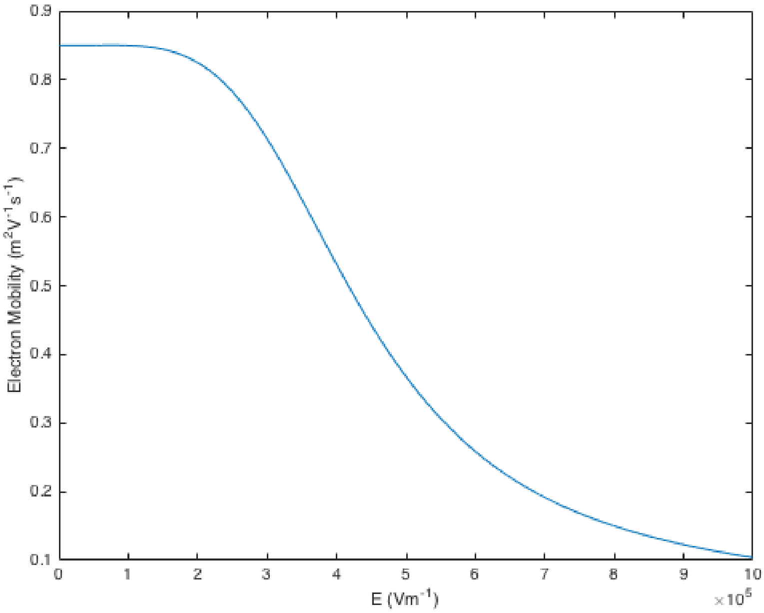

Figure 2.10: Field dependent mobility for GaAs used in the model.

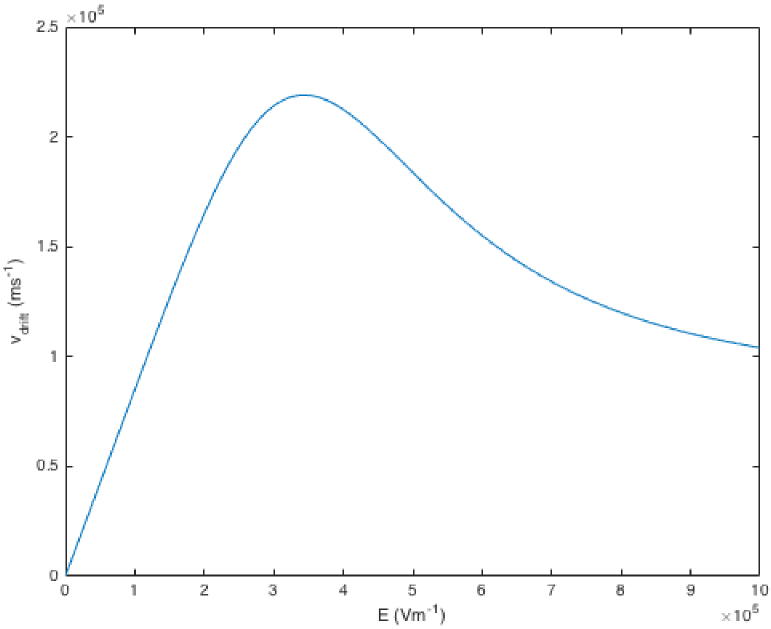

Figure 2.11: Field dependent drift velocity due to the mobility for GaAs used in the model.

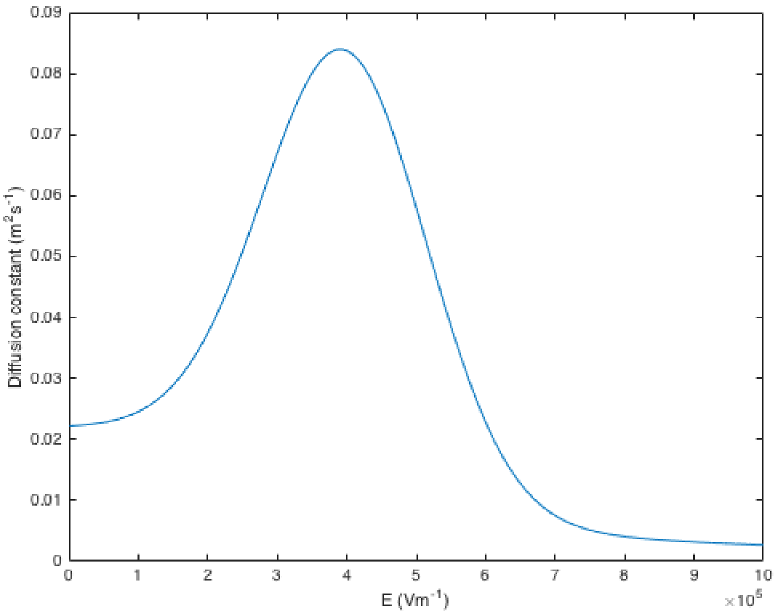

Figure 2.12: Field dependent diffusion coefficient used for GaAs used in the model.

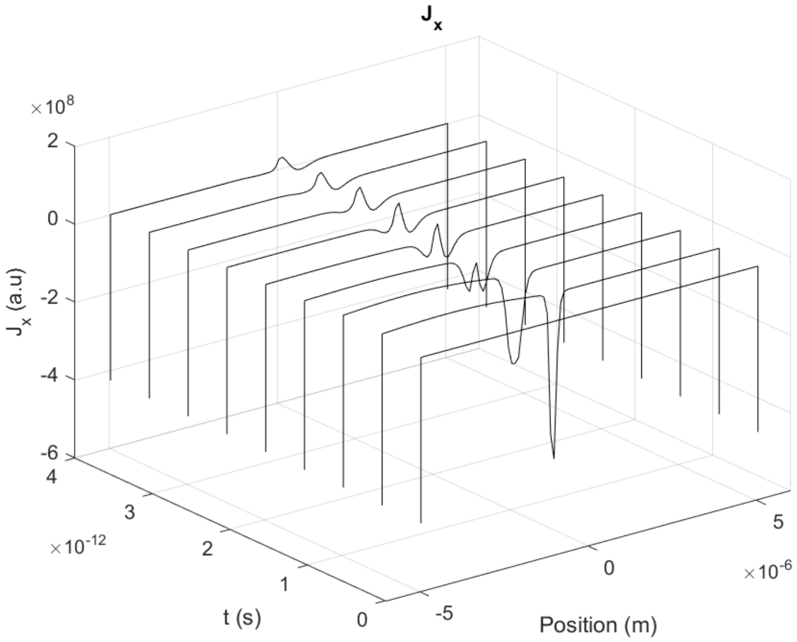

Figure 2.13: Current density evolution for a 1D distribution of carriers confined to the x-direction in bulk LT GaAs. The laser spot size is 10 μm, which is cut off by the presence of a metal mask at x = 0. This model does not include drift.

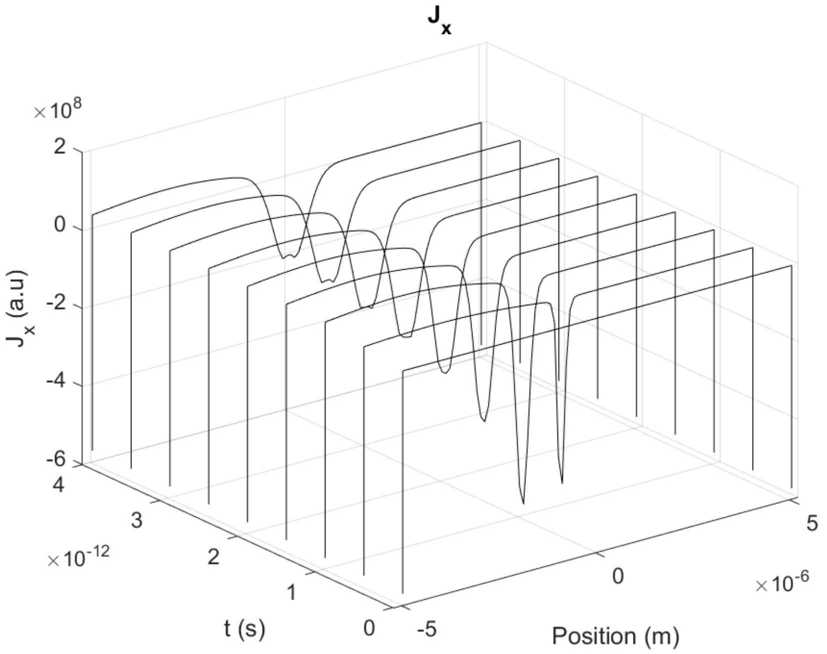

Figure 2.14: Current density evolution for a 1D distribution of carriers confined to the x-direction for a 1D problem using the same parameters as fig. 2.13, but with the SRH term from ref. [1]. This model does not include drift.

is now of SI-GaAs instead of LT-GaAs. The densities of holes and electrons at 2 ps in SI-GaAs are shown in fig. 2.15 as well as what would be the SRH term. The electrons have readily diffused away from the centre, while the holes have not. Since, to the left of where the densities are equal the SRH term is great, recombination will readily occour. As the sytem evolves, the carriers to the left of the crossover will decay at a faster rate to those on the right, first approaching the same density before the number of carriers on the left is less than the number of carriers on the right. This is the cause of the dip seen in the time evolution for LT-GaAs.

This model also agrees with Barnes' statement that the net current in the semiconductor is zero, supporting the claim that the mechanism suggested by Klatt et. al. is unphysical. The time evolution of the out-of-plane magnetic filed is presented in fig. 2.16. The magnetic field was chosen for the plots since, as there is only one directional component to it, the dyamics of the system can be inferred from H_z alone. This figure differs from the prediction by Barnes et. al, in that the width of the emitted pulse is much wider. The reason for this can be traced to the differing definitions of D. While I assume that the Diffusion constant for electrons is at its zero field value, Barnes followed the technique in [38], assuming an Einstein relationship with the mobility with the electron temperature at 3000 K. This leads to a factor of 10 difference between the two diffusion constants used, and as such the carrier dynamics in my model are spread over a longer time. However, there is agreement between the two models over the crux of Barnes' argument, that the metal mask leads to destructive interference and a break in symmetry.

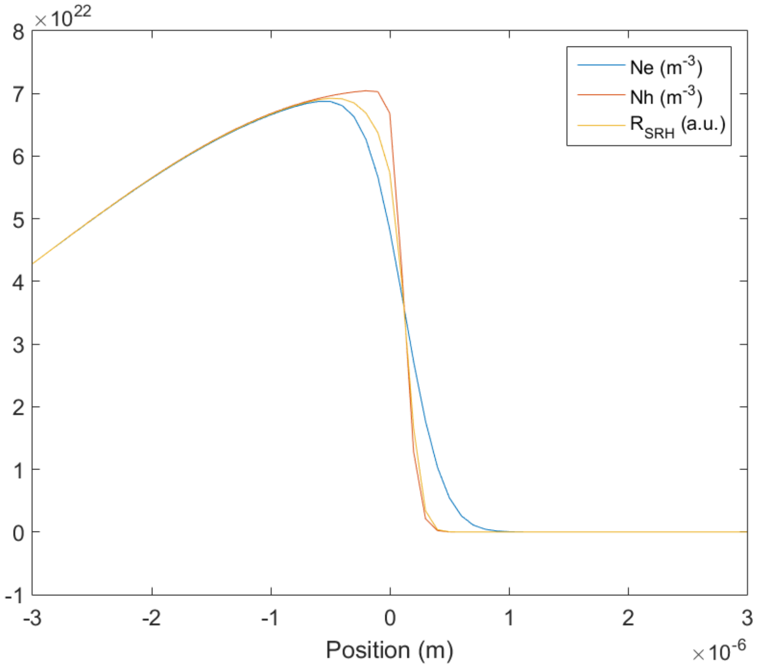

Figure 2.15: Density of holes and electrons in an SI-GaAs sample with no SRH term. What would be the SRH term for this distribution in LT-GaAs is also shown. In LT-GaAs, recombination would occur much more rapidly where $x < 0$. This model does not include drift.

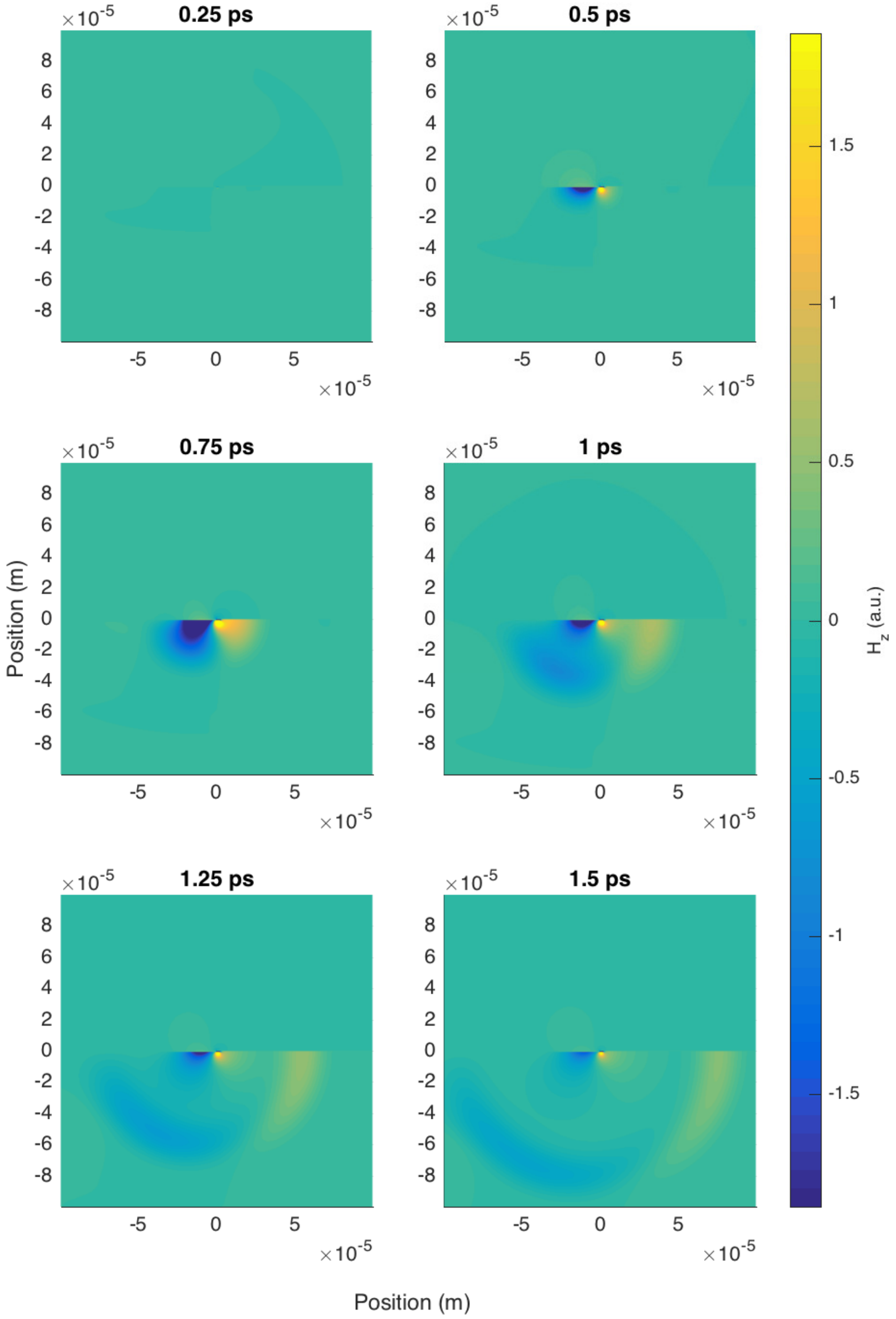

Figure 2.16: Out-of-plane magnetic field evolution for an LT-GaAs sample with a 1D current restricted to the x direction. The result agrees with Barnes et. al. that the symmetry is broken by destructive interference beneath the metal mask. This model does not include drift.

2.5.2 1D Diffusion Model in y

Secondly., I present a model similar to that previous shown. Rather than the currents being confined to the x-direction, they are confined to the y direction at the metal mask edge. G(x,y,t) is therefore 0 for $x < 0$ and $x > 0$. The semiconductor surface is described with the Neumann boundary condition $\frac{\delta n}{\delta y} = 0$. Shown in fig. 2.17 is the time evolution of the currents.

Shown in fig. 2.18 is the time evolution of the out-of-plane magnetic field. It can be seen that the emitted fields directly beneath the metal mask are stronger than those beneath the unmasked side, the opposite of that predicted by Barnes et. al. with their 1D DD model. The cause of these two opposing mechanisms is easily understood by comparing the emitted magnetic fields for unmasked samples with current restricted to the x or y direction, seen in figs. 2.19 and 2.20.

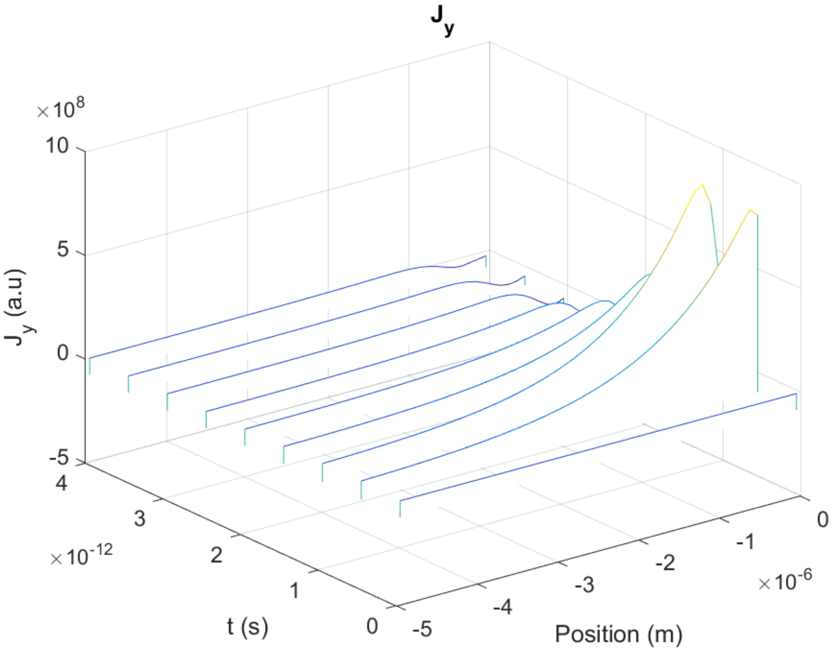

Figure 2.17: Current density evolution for a 1D distribution of carriers in LT GaAs confined to the y direction. The effects of electric field are neglected.

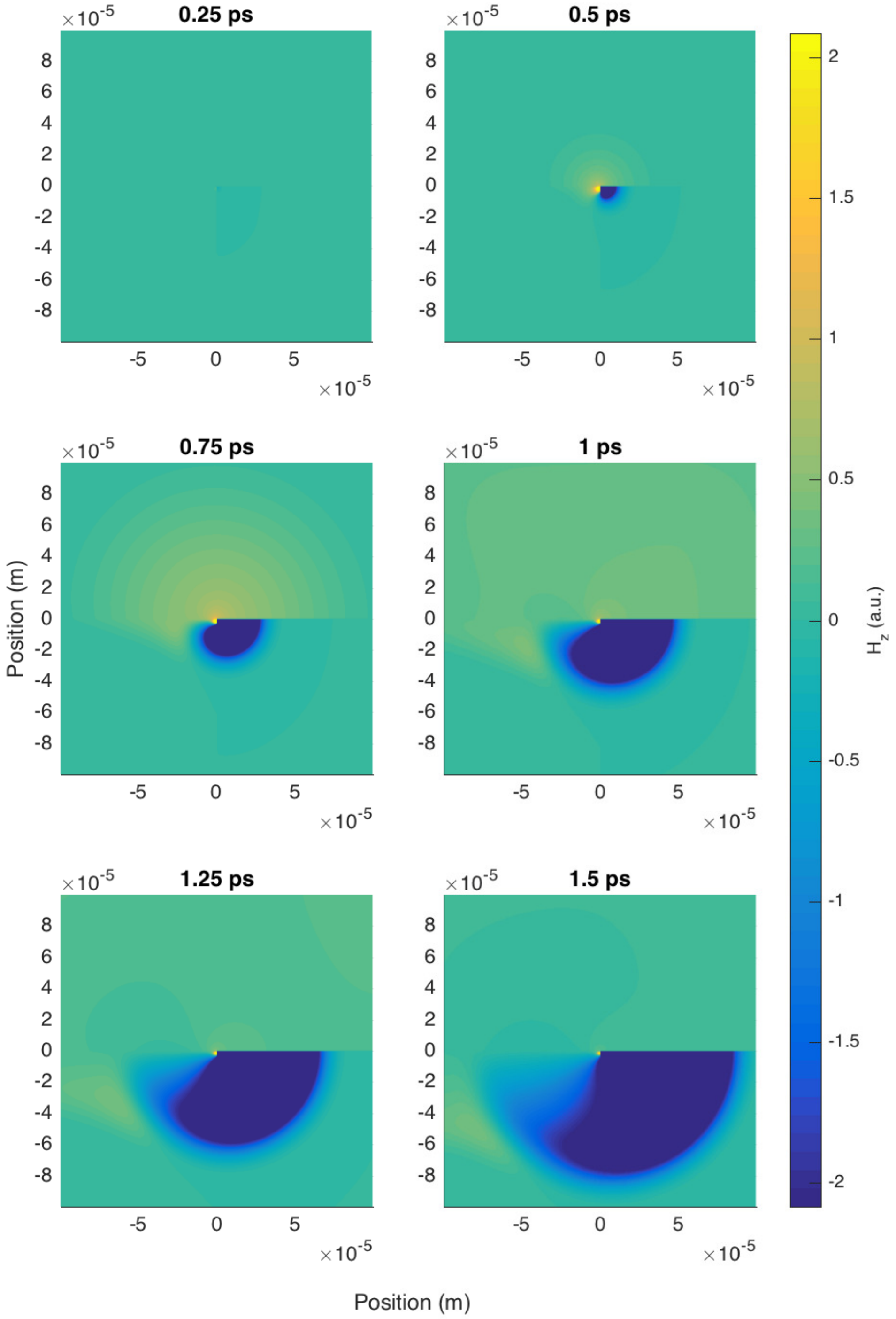

Figure 2.18: Out-of-plane magnetic field evolution for an LT-GaAs sample with 1D current restricted to the y direction. The result shows that the symmetry is broken by constructive interference beneath the metal mask. This model does not include drift.

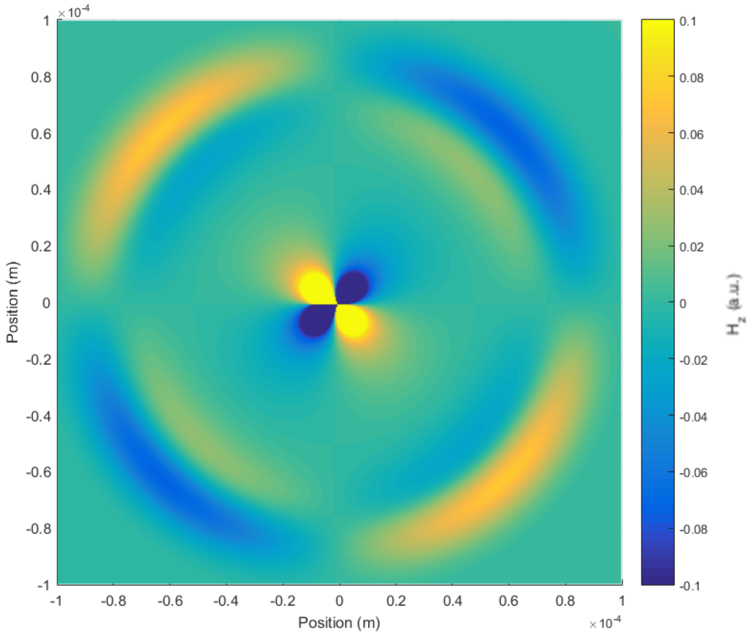

Figure 2.19: Out-of-plane magnetic field for an LT-GaAs sample 1 ps after peak illumination with a 1D current restricted to the x direction and the entire domain modelled as GaAs. The radiation is quadrupolar in nature, which would lead to destructive interference from a metal mask placed just above the currents. This model does not include drift.

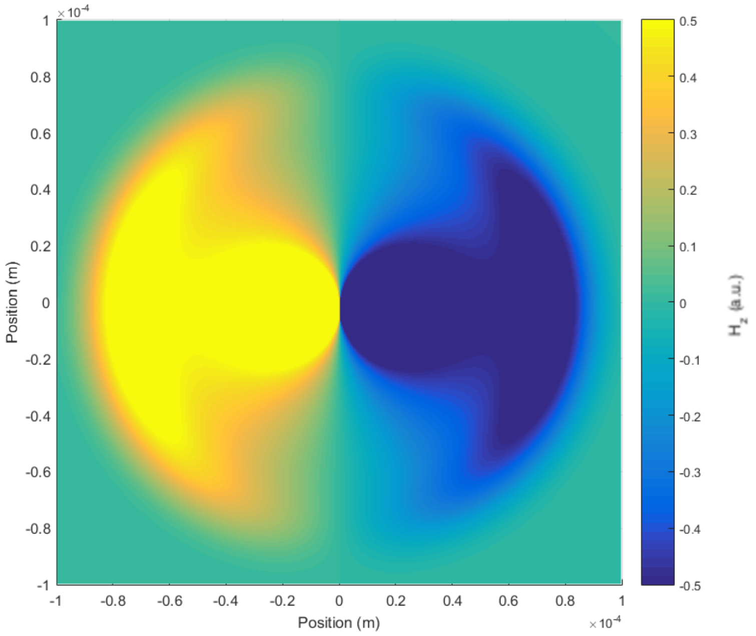

Figure 2.20: Out-of-plane magnetic field for an LT-GaAs sample 1 ps after peak illumination with a 1D current restricted to the y direction and the entire domain modeled as GaAs. The radiation is dipolar in nature, which would lead to constructive interference from a metal mask placed just above the currents. This model does not include drift.

2.5.3 2D Drift Diffusion

A model was then created to explore the dynamics of a 2D diffusion dominated system. In this case, a 2D diffusion system was modelled using the same material and pulse parameters as the 1D model. The currents were then fed in to a 2D FDTD algorithm. The evolution of the out of plane magnetic field is shown in fig. 2.21.

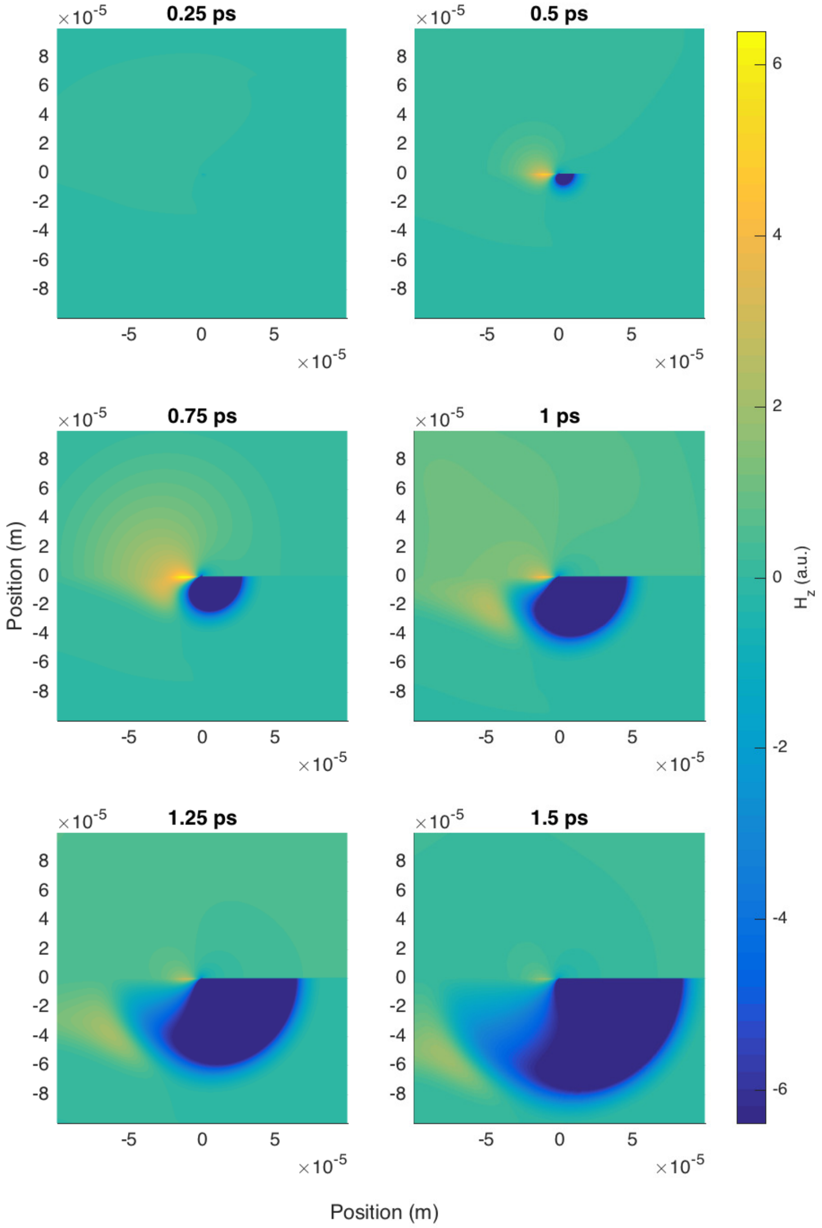

Figure 2.21: Out-of-plane magnetic field for an LT-GaAs sample with 2D currents, negelcting the effects of the electric field. Note the similarity to the 1D system with only y currents, in that constructive interference occurs beneath the metal mask. This model does not include drift.

It is immediately evident that the results resemble those caused by the 1D currents in the y direction than those from the x direction. For this reason, I believe that the primary cause of the LPD effect are the fields caused by the currents perpendicular to, rather than lateral to, the semiconductor surface. Shown in fig. 2.23 is the calculated far field at a (0, -1) m for two seperate 2D models. In each, the depth of the GaAs is 50 μm. This is smaller than that used in laboratory conditions, but a smaller depth helps to decrease the calculation time. The emission was generated with a spot size of 60 μm and a peak intensity of $1 \times 10^{11} W m^{-2}$. The most notable difference is the relative strength of the diffusion dominated system to the drift dominated system. This is easily understood by considering the total currents in each. For the drift-diffusion system, drift currents arise which in the case of electrons oppose the diffusion currents. This leads to an overall decrease in net current in the sample. Though the hole drift current will flow in the same direction as the hole diffusion current, this increase is negligible due to the lower mobility of holes. The evolution of this drift-diffusion system is shown in fig. 2.22, and a demonstration of the effects on the far-field of including drift is shown in fig. 2.23. This disagrees with the conclusion by Mark Barnes that the effects of drift are negligible.

For the drift-diffusion system, I further present a graph showing the angular dependence of the far field. Taking the direction of 0° to be negative y, and defining the other angles by sweeping from this point in the anticlockwise direction, I show the far field line scans at -25°, 0° and 25° in fig. 2.24. Further shown in fig. 2.25 is the far-field linescan at 0°, as well as the average of the far field linescans sweeping from -25° to 25° in 5° intervals. Since the parabolic mirrors used for many LPD experiments in our lab collect at a 50° angle, this average should resemble the far field linescans in experimentation. Indeed, unlike the linescan at 0°, it shows the small downwards tick before the peak emission often found in experimentation. The shape of this linescan shows good qualitative agreement with the measured fields for LT-GaAs in [3]

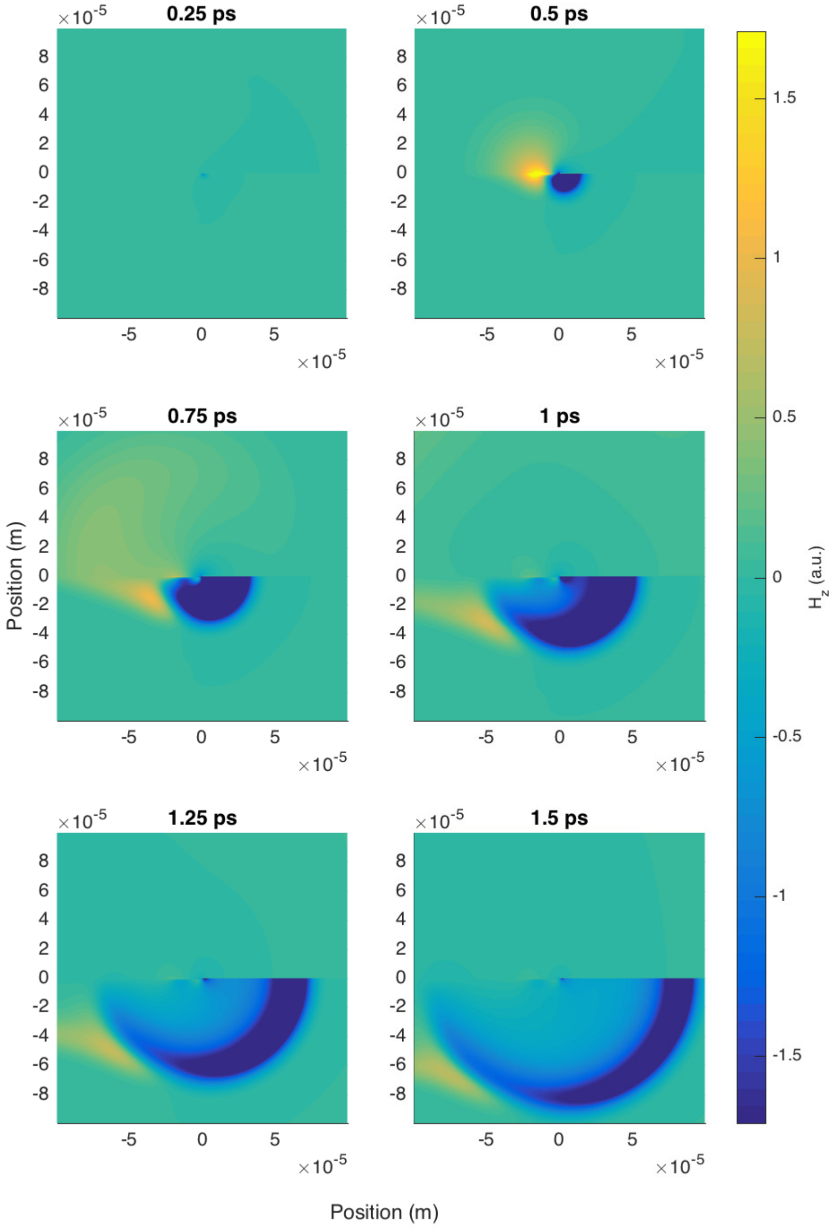

Figure 2.22: Out-of-plane magnetic field for an LT-GaAs sample with 2D currents with the effects of drift included. Again, constructive interference occurs beneath the metal mask.

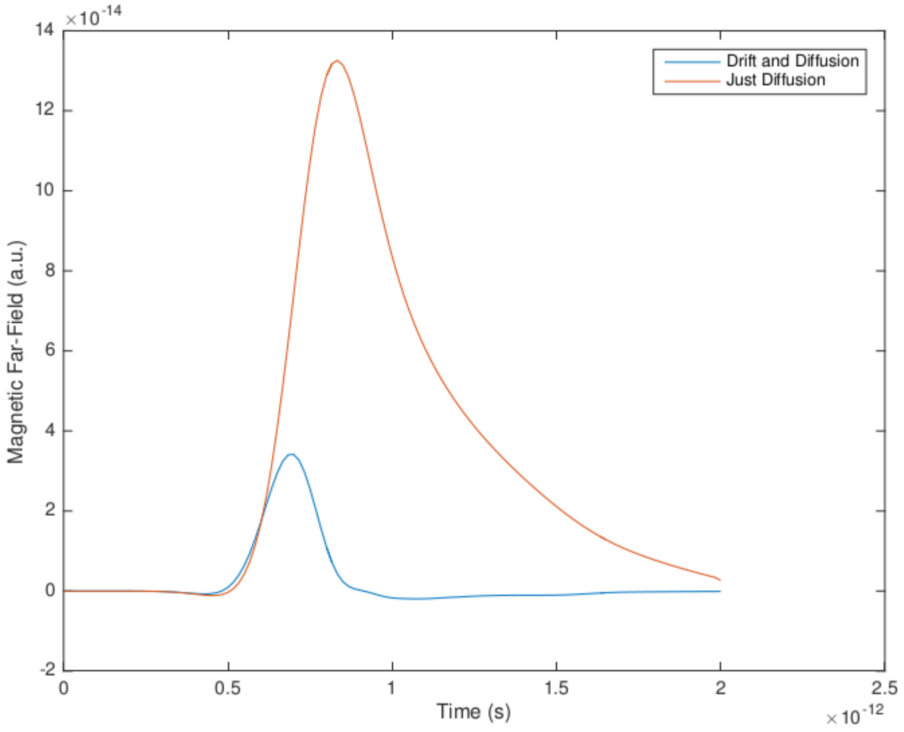

Figure 2.23: Far-field time-domain scans for two 2D system, one in which only diffusion is considered and one in which both drift and diffusion are considered. The lower intensity of the drift and diffusion system is due to drift currents opposing the diffusion currents.

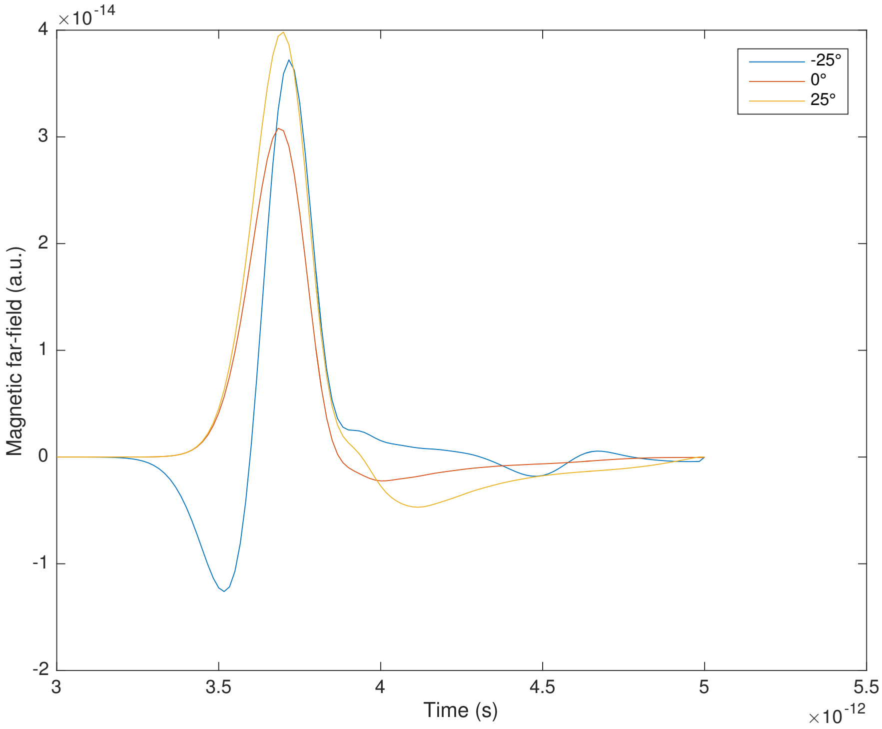

Figure 2.24: Far Field linescans for an LT-GaAs emitter taken at different far-field angles with both drift and diffusion included.

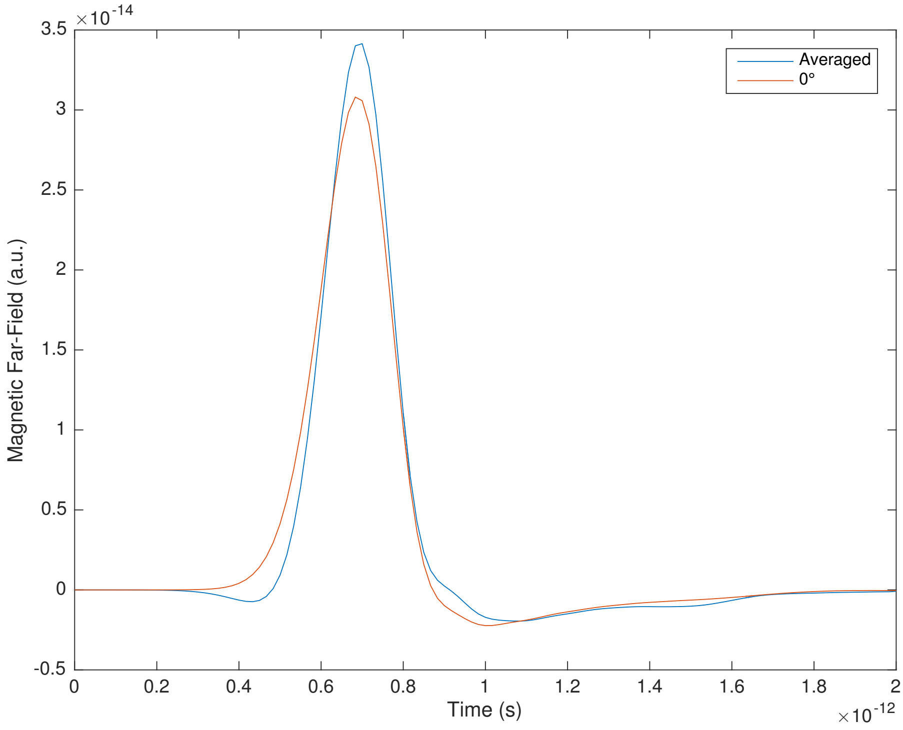

Figure 2.25: A comparison of the average far field linescans between -25° to 25° to the far-field linescan at 0°. The average linescan shows the small tick before peak emission as observed in experimentaiton.

2.5.4 Spot size and Fluence

A further investigation was performed in to the effects of laser fluence and spot size on the dynamics of the drift diffusion system. Spot sizes of 8, 15, 23, 30, 45 and 60 μm were used to excite carriers within an SI-GaAs emitter. These spot sizes were chosen so as to be able to draw comparisons with the results for SI-GaAs found in [2] shown in fig. 2.26. To compare the relative strengths of the x and y current components for each sample, the time derivatives of each current component were integrated over a chosen area in the simulation domain. Since the fields emitted by the x component of current are cancelled beneath the metal mask, the x component was integrated over the area on the unmasked side. The y currents are assumed to emit equal and opposite fields in the two directions parallel to the semiconductor surface. Since the fields underneath the metal mask undergo constructive interference, all y currents are assumed to contribute to the emitted fields and the time derivatives are integrated over the entire simulation area.

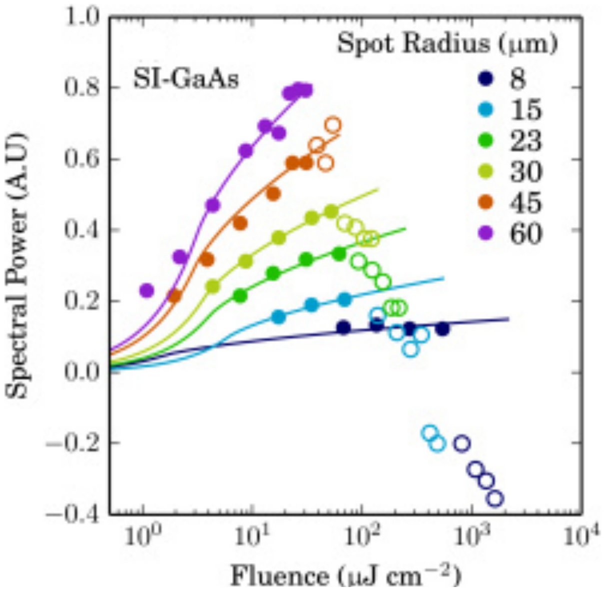

Figure 2.26: The results of the spot size experiment for SI-GaAs performed by McBryde et al.[2]

Shown in fig. 2.27 are the spectral powers of the waveform given by the integration of $\delta J_y/\delta t$ taken as a function of time. It is immediately apparent that by increasing the spot size at a certain fluence, we increase the amount of THz radiation emitted due to the y-currents.

Shown in fig. 2.28 is the spectral power of the waveform given by the integration of $\delta J_y/\delta t$ taken as a function of time, integrated over the area not underneath the metal mask. This value was not plotted for other spot sizes, as the difference between the spot sizes was negligible. Plotted for comparison are given by the currents in y for spot sizes of 8 and 60 μm. We can understand why this might be the case by acknowledging

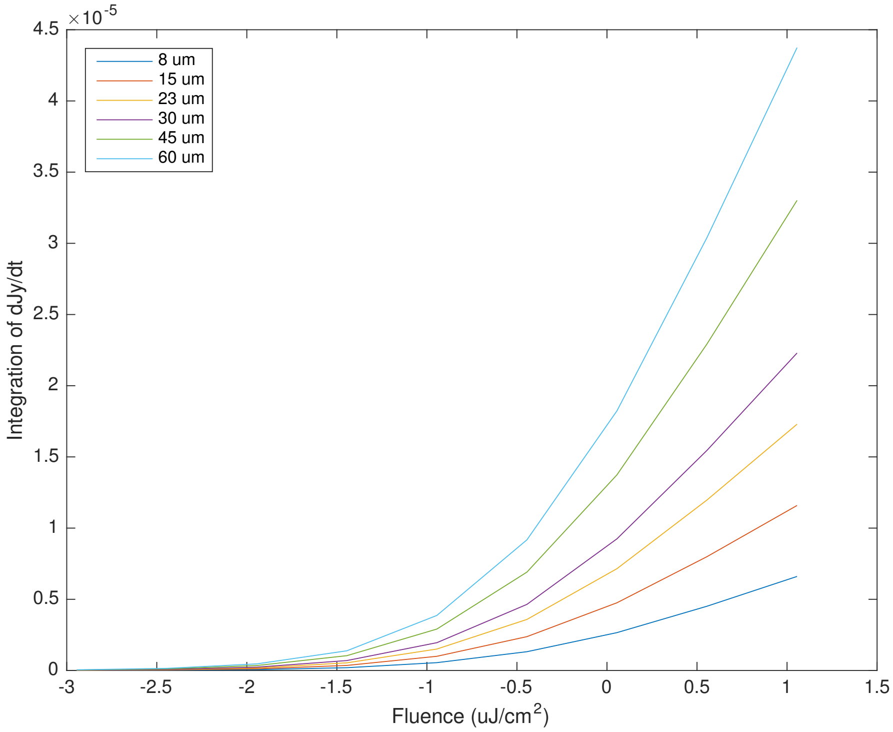

Figure 2.27: Spectral powers given by the waveforms of $\delta J_y/\delta t$ integrated over the simulation domain. These results indicate that the intensity of the observed radiation due to the currents perpendicular to the semiconductor surface should change with spot size.

that in the diffusion regime, the total net current for a distribution of carriers in an unbounded region of space is zero. Since the small amount of light diffracted under the metal mask is independent of the overall spot size and only depends on the peak fluence, the number of carriers beneath the metal mask after illumination is independent of spot size. These carriers are responsible for all diffusion away from the mask edge beneath the masked area. This means that, regardless of spot size, the fields given by the currents in x remain the same at a given fluence.

This further supports the theory that the y currents are predominantly responsible for the observed radiation given by the LPD effect. Since it has been reported[2, 3] that the intensity of the observed radiation from the LPD effect increases with spot size, according to the DD model, only the currents in y could be responsible for this behaviour. Unlike the experiments performed by McBryde et. al, no saturation is observed as the intensity increases. This is likely due to the fact that the drift-diffusion model does not account for the fact that the number of carriers that can be excited from each band is finite. While in experiment the number of excited carriers will saturate with increasing spot power, in the model no such saturation occours and the strength of the emitted radiation will continue to increase. Finally, the dramatic drop in power at higher fluences for lower

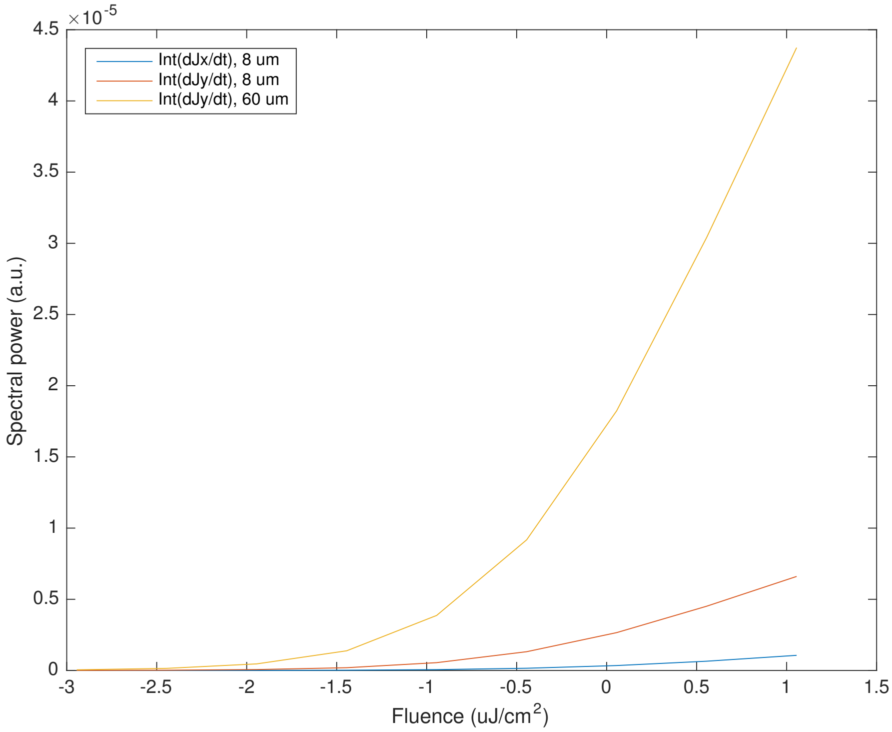

Figure 2.28: Spectral powers given by the waveforms of $\delta J_x/\delta t$ integrated in the area not beneath the metal mask for a spot size of 8 μm, and those for $\delta J_y/\delta t$ for spot sizes of 8 and 60 μm integrated over the simulation domain. Only the results from one spot size were used for the x currents, as there is no significant change with spot size. This indicates that the resulting THz emission due to the currents in x do not change with spot size.

spot sizes in fig. 2.26 is unseen in the model. This is expected as this downturn has been attributed to the Schottkey effect[2].

2.6 Conclusions

In this chapter I have demonstrated that the LPD effect in fact depends on both the lateral and perpendicular currents, whereas it was previously believed that only the lateral currents are responsible. Furthermore, it seems that the drift plays a large role in LPD emitters as opposed to being a negligible effect as proposed by Barnes et. al. I have extended the model by Barnes by introducing Auger recombination, surface recombination and a more realistic SRH trapping term. Furthermore, my model utilises a field dependent mobility and diffusion constant, rather than an assumption that they are constant throughout the model. Secondly, I have also fed the results in to a far-field algorithm from which we can see the angular dependence of the emitted far-field, as opposed to simply using the Hertzian dipole approximation in which the far field is assumed to be directly proportional to the change in current.

Chapter 3

THz Experiments

3.1 Terahertz Time Domain Spectroscopy

The advent of THz spectroscopy began in 1975 when Auston et al. demonstrated broadband emission of single cycle THz pulses from a photoconductive antenna[89]. This technique, in conjunction with ultrafast pulsed lasers, led to the development of THz time domain spectroscopy (THz-TDS)[90]. A general THz-TDS setup is shown in figure 3.1. An ultrafast laser, typically a titanium sapphire (Ti:S) with a pulse width on the order of femtoseconds is first passed through a beam splitter to create two separate pulses which we will designate as the pump pulse and the probe pulse. The pump pulse illuminates an emitter, usually a photoconductive antenna (PCA). The generated THz wave is then directed on to a pair of parabolic mirrors which guide the beam and focus it on to the detector, also usually a PCA. At the same time, the probe pulse is passed through an optical delay and used to illuminate the detector. The probe pulse also passes through an optical chopper connected to a lock-in amplifier[91]. The generation of photocarriers in the detector allows for the detection of the THz wave as a current, while the optical delay allows the relative time of arrival of the gating pulse with respect to the THz pulse to be controlled. By adjusting this delay time fractionally and repeating the experiment, a time domain scan of the generated pulse can be collected. The signal generated by the chopper is fed in to the lock-in amplifier in order to isolate the signal of the THz pulse from background noise.

THz-TDS allows for a complete measurement of the E-fields in the time domain, which can then easily be converted to the frequency domain through a fast Fourier transform. The spectrum obtained from THz-TDS scan usually spans over multiple octaves, with a typical range of around 50 GHz to 3 THz[3]. Because THz-TDS is a synchronous detections scheme, pulses below the black-body radiation will average to zero[92]. This allows a remarkably high signal-to-noise ratio to be achieved. Also, since THz-TDS is a pump-probe experiment, it is possible to explore the dynamic behaviour of a materials permittivity after some stimulus is applied. This is because the THz signal can be measured at a specific time after some other event has taken place and since it is the transient electric fields, rather than the intensity is measured, THz-TDS can reveal the complex permittivity of a sample without the need to use the Kramers-Kronig relations[93].

For this thesis, THz-TDS was used to explore the characteristics of lateral photo-Dember emitters and explore the model presented in the previous chapter.

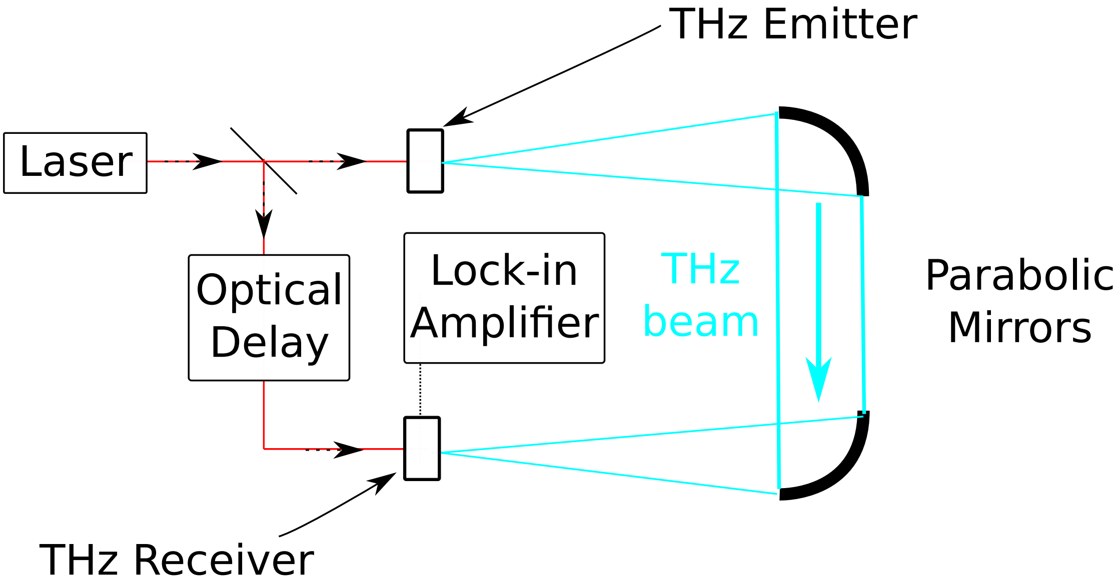

Figure 3.1: A typical THz-TDS setup

3.2 Bias Experiments

An experiment was performed by Mark Barnes [3] in which an LPD emitter was subjected to a biasing electric field. This was achieved by the presence of two metal masks on the surface of the substrate separated by a 200 μm gap as shown in fig. 3.2. These two plates were used as electrodes, and the edge of one was used as the LPD mask. In this manner, it was possible to apply a voltage across the plates and observe the effects of a static bias on the emission. The time domain scans for two biases and an unbiased emitter are shown in fig. 3.3.

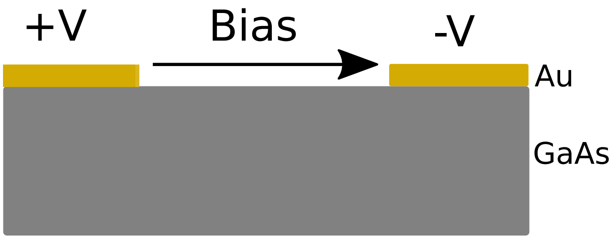

Figure 3.2: The setup for the biasing experiments. The two gold contacts are used as electrodes to apply a voltage across the sample.

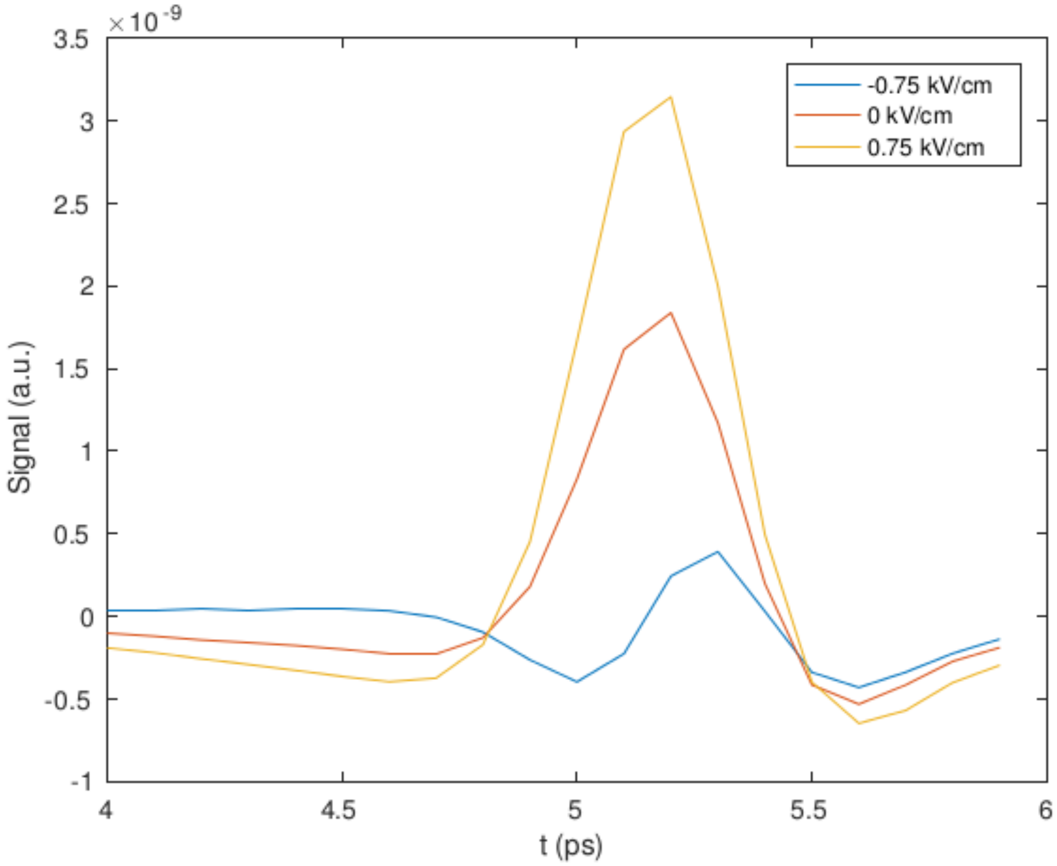

Figure 3.3: The linescans for the experiments performed by Mark Barnes.[3]

It can be seen that it is possible to either enhance or destroy the emission from an LPD emitter by applying an electric field. The recreation of this effect was attempted using the model produced in chapter 2.

Firstly, recreating the effects of the electric field was attempted by adding a potential, V_{bias} to the electric potential for a sample illuminated with a peak intensity of $1 \times 10^{12} Wm^{-2}$. This intensity was chosen as it translates to an average power of around 150 mW, the value used for the experiment. For the same reason, a spot size of 60 μm was used. It was found that, when using the diffusion constant and mobility the model gives a result where the biasing field dominates, and strength of the emission for each biased sample is much greater in magnitude than the emission from the unbiased sample. These effects are shown in fig. 3.4.

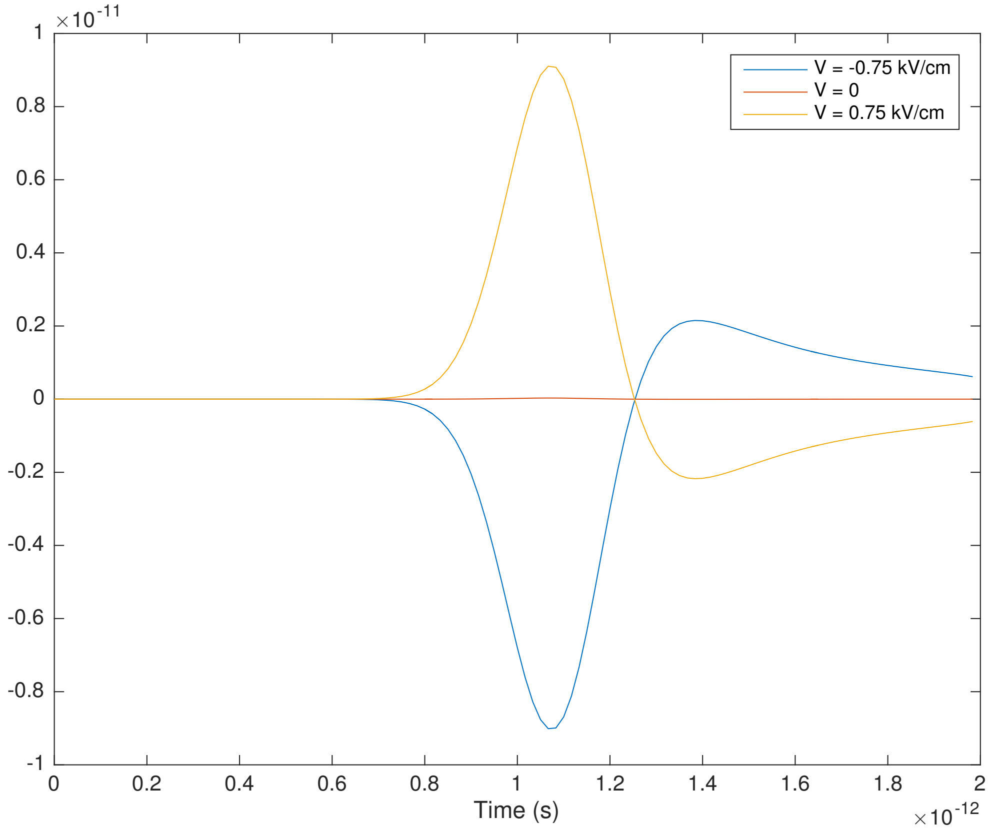

Figure 3.4: An attempt to recreate the experimental results using the parameters used in chapter 2. As can be seen, the biasing field dominates the emission.

These results indicate that the effect of the bias is too strong in relation to what we experience experimentally. The cause of this effect was due to a misunderstanding of the electric bias used in the experiment. It was assumed in fig. 3.4 that the electric field used to label fig. 3.2 referred to the internal electric field of the GaAs sample. Assuming instead that it refers to the external electric field applied to the sample (as verified with Mark Barnes), we must divide the field by ϵ_{GaAs}. The results under this condition shown in fig. 3.5 still overstate the effects of the electric field.

The disagreement between the model and the experimental results can be understood by realising that the ratio of D to μ is in reality not only governed by the electric field, but also from other mechanisms such as impurity and phonon scattering. Since the drift-diffusion model does not model carrier temperature, a suitable assumption must be found if we wish to introduce the effect of carrier temperature.

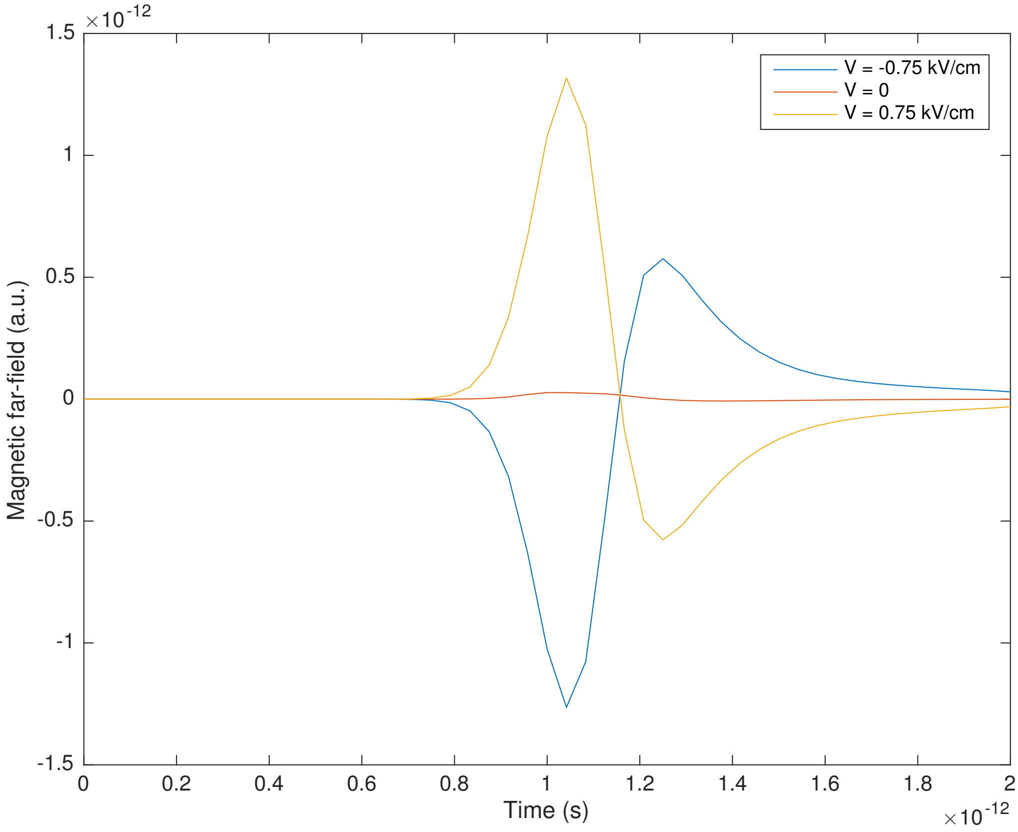

Figure 3.5: A second attempt to recreate the results of the experiment by Barnes. et. al. In this model, the biasing field used in the previous model was divided by ϵ_{GaAs}

Finally, I present the results from a model under the same injection conditions, however assuming that the mobility and diffusion constants are always at the values found at saturation. The results for this model are found in fig. 3.7. The assumption of saturation values for μ and D is based on an assumption of 'hot' carriers. It has been stated that under high injection conditions, the temperature of the electrons may far exceed the temperature of the lattice[94]. Dekorsy et. al.[38] state that this temperature is around 2000 K. Plotted in fig. 3.6 is the derived carrier temperature for different electric fields using the Einstein relationship. It can be seen that by using the values at the saturation field (4×10^5 V/m), we model the carrier dynamics as if the temperature of the electrons was 2000 K. However, this also requires that the electric field has no effect on the ratio of D to μ as there is no trivial way to understand the combination of effects. So, for the following models, we assume that the electric field has no effect on the values of D and μ and they are solely governed by the temperature.

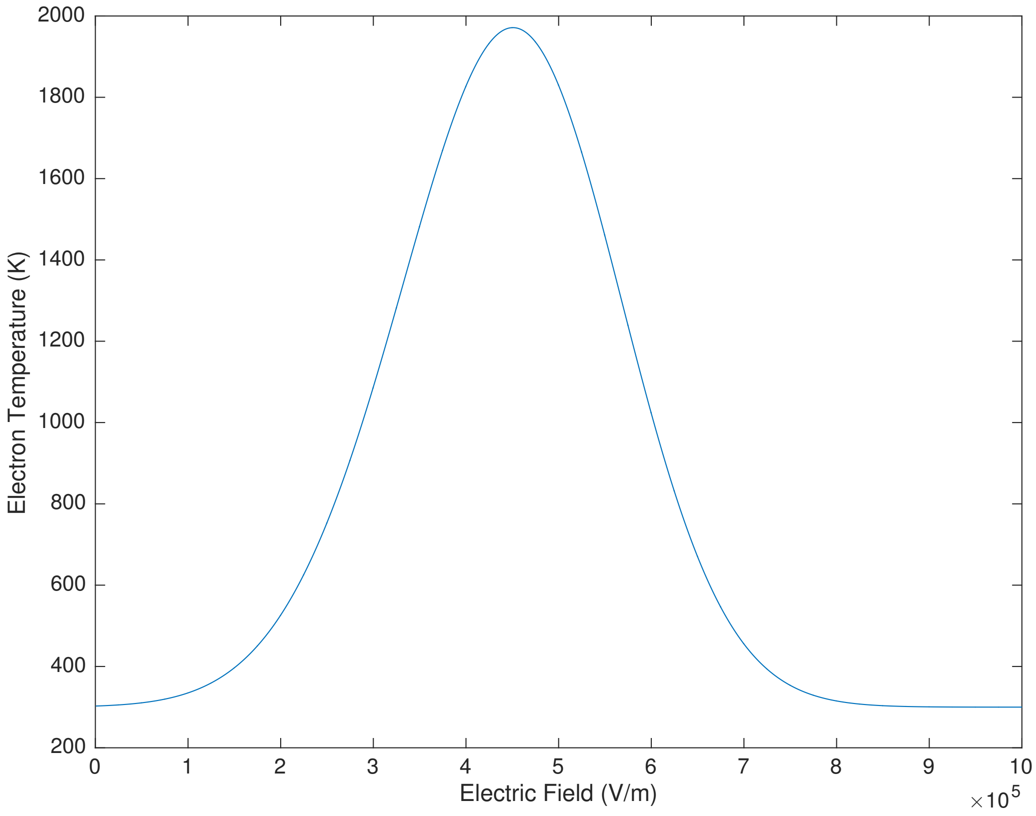

Figure 3.6: The electron temperature derived from the Einstein relationship between μ and D. The peak in temperature occurs at the saturation field.

It was discovered that, under these conditions, the model far more accurately predicts the effects of the biasing field (fig. 3.8. This likely indicates an underestimation of the ratio between the diffusion constant and the mobility in the previous models. This could well be due to the effects of the thermalisation of electrons being poorly expressed in the model.

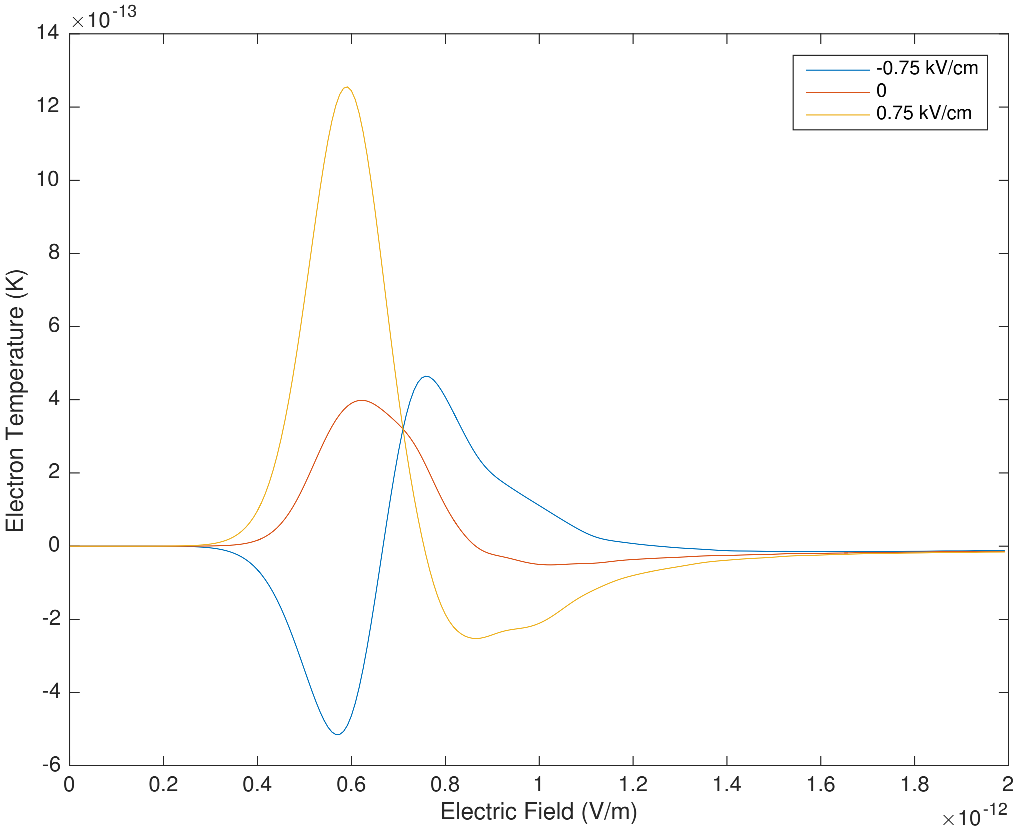

Figure 3.7: The biasing experiment, assuming the values of μ and D are those at saturation with a peak pulse intensity of $1 \times 10^{12} Wm^{-2}$

A further model was produced, with the same parameters as the previous model, but with the laser peak intensity set to $1 \times 10^{11.5}$ Wm^{-2} and a spot size of 45 μm. Shown in fig. 3.8 It can be seen that under these conditions, the enhancement or destruction of the overall signal in the linescan more closely resembles that in experiment than that of 1×10^{12} Wm^{-2}.

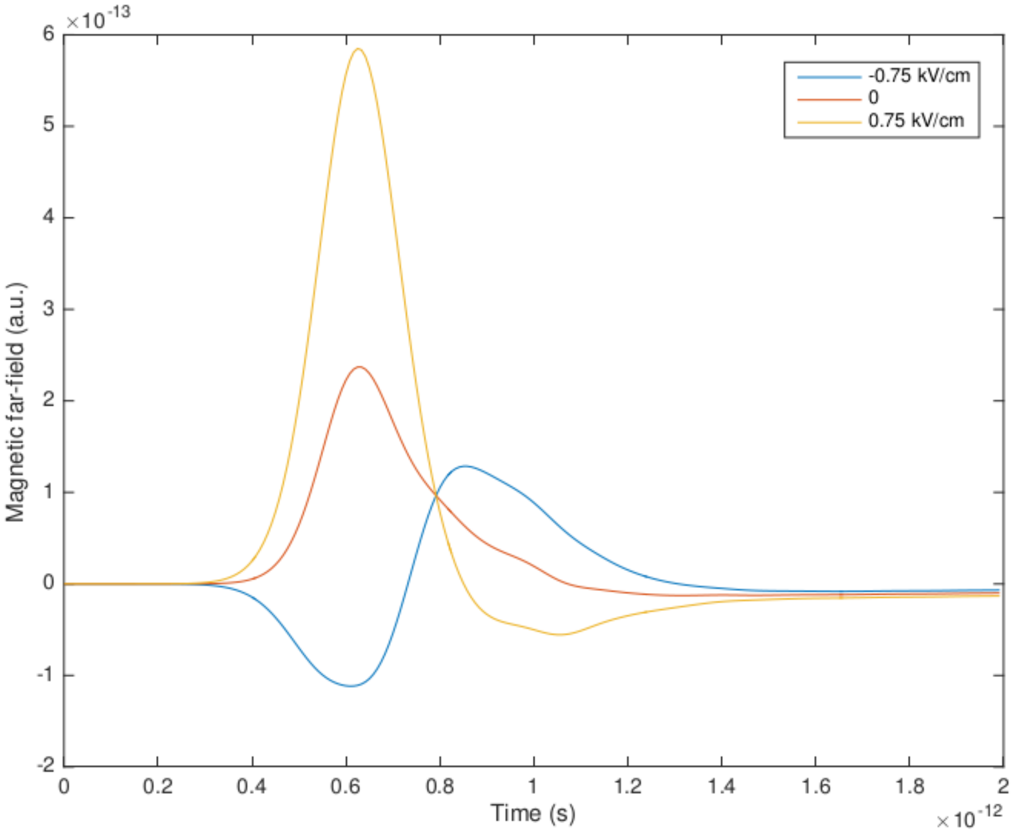

Figure 3.8: The biasing experiment, assuming the values of μ and D are those at saturation with a peak pulse intensity of $1 \times 10^{11.5} Wm^{-2}$ and a spot size of 45 μm

The reason for this enhancement or suppression depending on the biasing field is easily understood. While under no bias, the currents in y dominate as expressed in chapter 2. However, when an electric field is applied in the x direction, the currents in x undergo far more rapid acceleration than when under 0 field conditions. In these circumstances, the emission from the currents in x produce emission on the same order of magnitude as the currents in y. When a positive bias is applied, the resulting THz emission from the currents in x enhances the emission from the currents in y. When a negative bias is applied, the resulting THz radiation from the currents in x is of the opposite sign, and interferes destructively with the emission produced by the y currents. Using the model shown in fig. 3.8, I present the integrated time derivative of the currents in x for the not beneath the metal mask in fig. 3.9 It can be seen that the currents generated for the biasing conditions are much greater than those created for zero field. Also, by comparing figs. 3.9 and 3.8 it can be seen how important it is to take into account the currents in y in order to match the results of the labs.

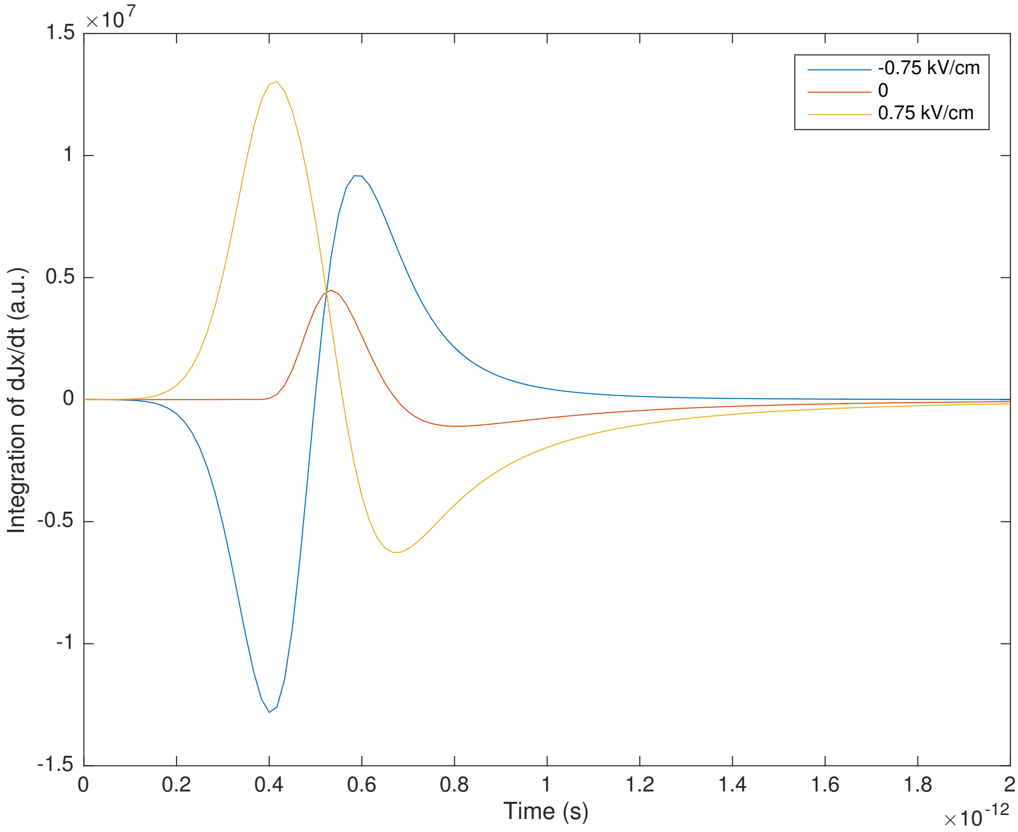

Figure 3.9: The integrated time derivative of the currents in x on the unmasked side under different bias conditions for a pulse of peak intensity $1 \times 10^{11.5} W m^{-2}$ and spot size $45 \mu m$. Note that the magnitude is much greater for the biased samples.

3.3 Spaced LPD emitters

Here, I wanted to investigate the level of suppression from the metallic part of the sample by raising using a flat thin film of a dielectric. This configuration is shown in Fig. 3.10. Firstly, small pieces of SI-GaAs were cleaved and spun with SU-8 photoresist before baking and developing them with in the presence of no mask, leaving a layer of U-8 photoresist on top of the substrate. By choosing both the viscosity and spin speed according to the official datasheets, it was possible to control the thickness of the deposited SU-8 layer. The sample was then exposed, baked, and developed. A small portion of the SU-8 on the very edge of the sample was left unexposed. This allowed for the height of the SU-8 layer to be measured using an alpha step. Half of the surface covered in SU-8 was then masked, and a gold layer was then thermally evaporated on to the surface of the SU-8. In this way, it was possible to produce a lateral photo-Dember emitter with a cavity between the semiconductor and the metal mask.

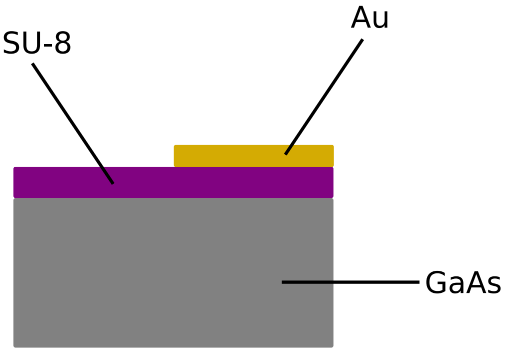

Figure 3.10: Geometry of the spaced LPD emitters

Three samples with cavity thicknesses 35 and 90 μm were produced. Each was then excited with a femtosecond laser pulse in a THz-TDS setup, using a photoconductive antenna as a detector. For each sample, time and Fourier scans were obtained to examine the effect of the cavity spacing on the produced THz pulse.

3.3.1 Results

Shown in Fig. 3.11 are the time domain scans for each thickness. It can be seen that the introduction of larger cavities lead to a broadening of the THz pulse in time. This is fairly trivial to understand; by introducing a cavity between the semiconductor surface we have delayed the time between which the THz pulse is emitted and the reflected part of the wave interacts with the rest of the pulse. This is illustrated in fig. 3.12.

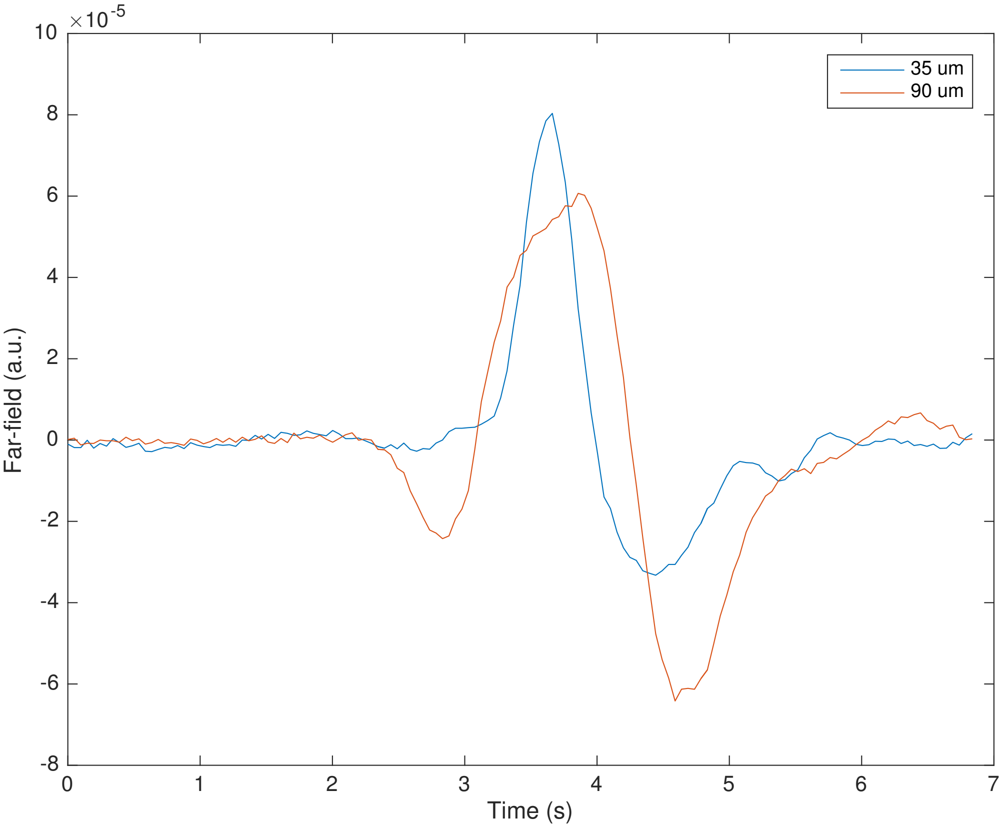

Figure 3.11: Time domain scan of the spaced photo-Dember emitters with SU-8 thicknesses of 35 and 90 μm. As expected, the spacing causes the pulse to broaden.

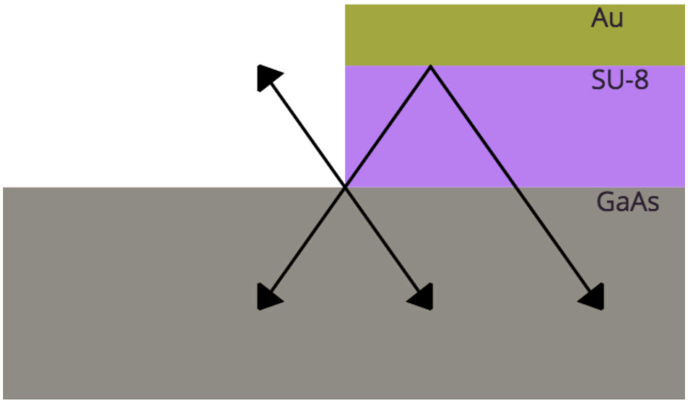

Figure 3.12: An illustration of the photo-Dember effect after illumination with an SU-8 cavity present. The black arrows represent possible paths for THz raditaion To the left of the mask, the fields are free to radiate. To the right of the mask edge, the fields travelling upwards are reflected after a delay and then propagate downwards where they expoerience interference.

Shown in fig. 3.13 is the fast Fourier transform of the signal from the sample with a 90

μm. From a 90 μm thickness and a refractive index of around 1.5, we would expect a FSR of around 1 THz. From fig. 3.13, it is apparent that this is the case.

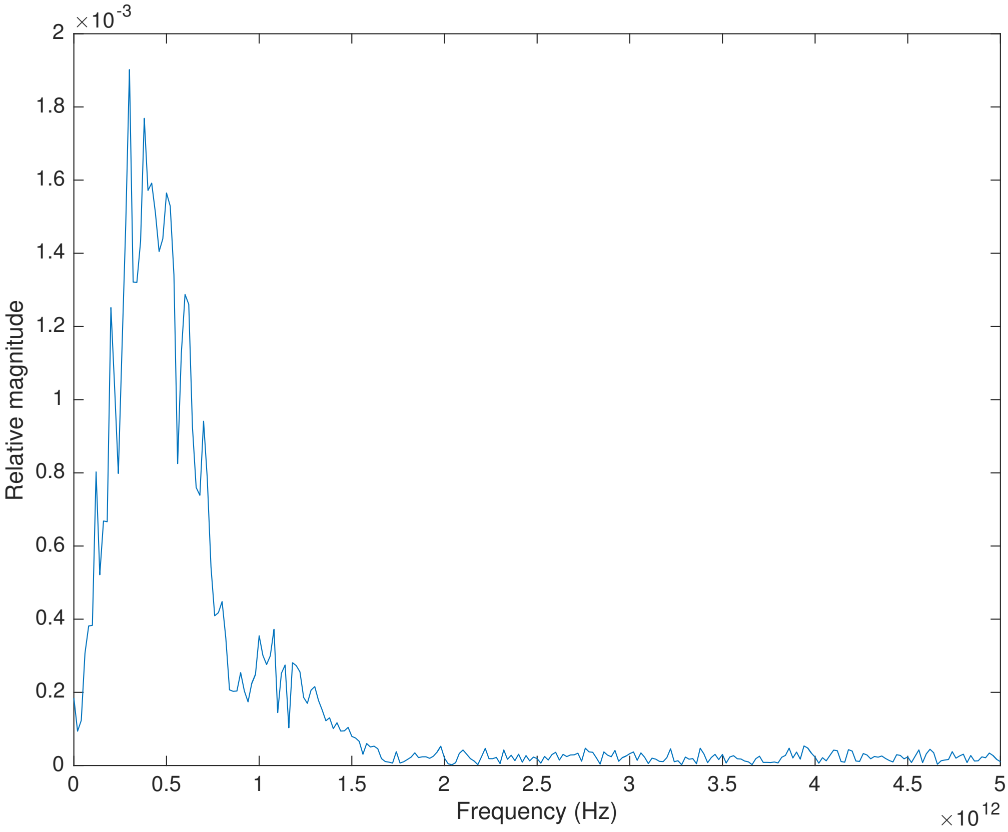

Figure 3.13: Fourier transform of the emitter with a 90 μm spacing. Note the FSR created by the introduction of a cavity.

An attempt to recreate these results was performed using the DD-FDTD model. Again, high injection conditions were assumed. The linescans produced by the model for both thicknesses are shown in fig. 3.14. It can be seen that the model agrees with experiment in the reduction of the peak intensity of the linescan between the 35 μm and 90 μm spacings. However, the stretching of the temporal pulse as in experiment was not so apparent. However, it can be seen that a small peak in the linescan for the modelled emitter with a 90 μm spacing exists at around the 1.2 ps mark, before the main peak. It is therefore possible that the model underestimates the temporal width of the emitted THz pulse, and that the effect observed in experiment would indeed be visible if the THz pulse was broader in time. It is possible wisth of the THz pulse is narrower in the model than in experiment due to the lack of dispersion in the FDTD algorithm, which would cause different frequency components to have different travel times through the substrate. Furthermore, the model does not account for the convolution of the detector, which would broaden the detected signal over time[**?**].

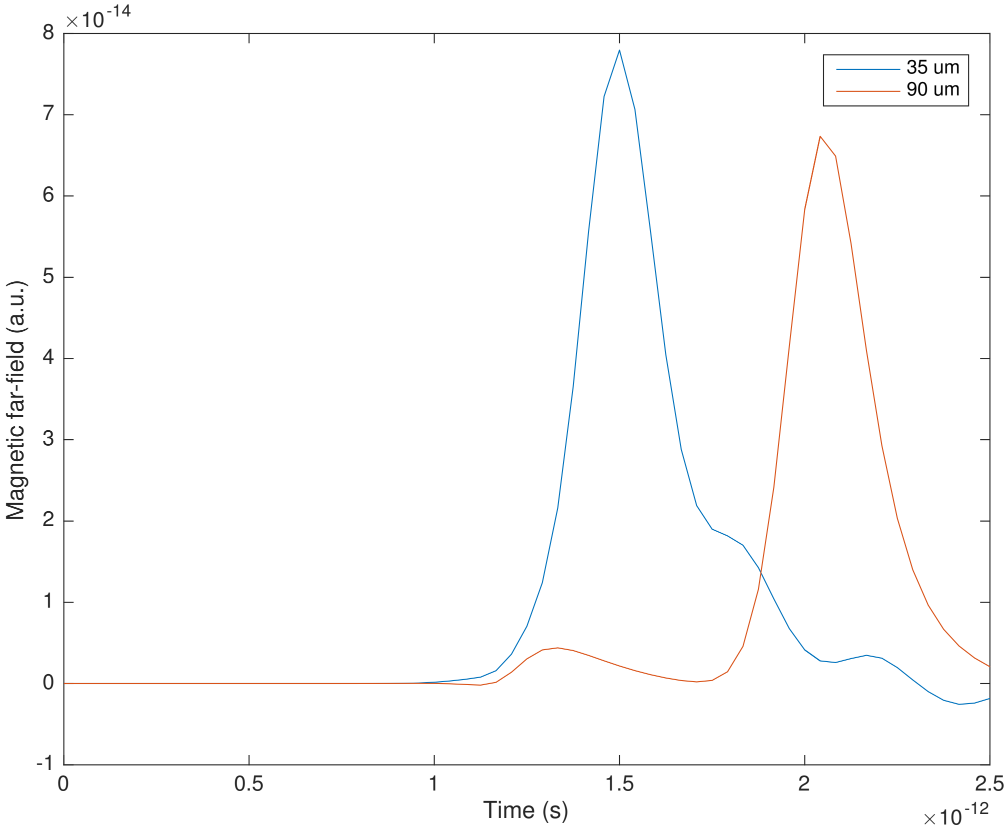

Figure 3.14: Time domain scans for the two cavity thicknesses reproduced in the model. While the stretching of the temporal pulse is not comparable to the experiment, the reduction in the peak intensity is.

Secondly, I show the Fourier transforms for the linescans produced with each model in fig. 3.15. It can be seen that the model fairly accurately predicts the location of the FSR, however we can also see both higher and lower frequencies are observed in the model when compared to experiment. This would indicate that either these frequencies are erroneous in the model, or that the observed THz spectrum in experimentation is limited by the by the response of the detector. Since higher frequencies have a smaller focus, it is highly possible that the alignment of the experimental setup was simply not accurate enough to detect these frequecies. The presence of the lower frequencies in the model not observed in experimet can be attributed to the lack of dispersion in the model. In reality, at the lower end of this spectrum, the refractive index of photoexcited GaAs can be over double the value given for non-photoexcited GaAs[95]. This would dramatically increase the time for the lower frequency components to travel through the substrate, causing them to arrive well after the initial pulse.

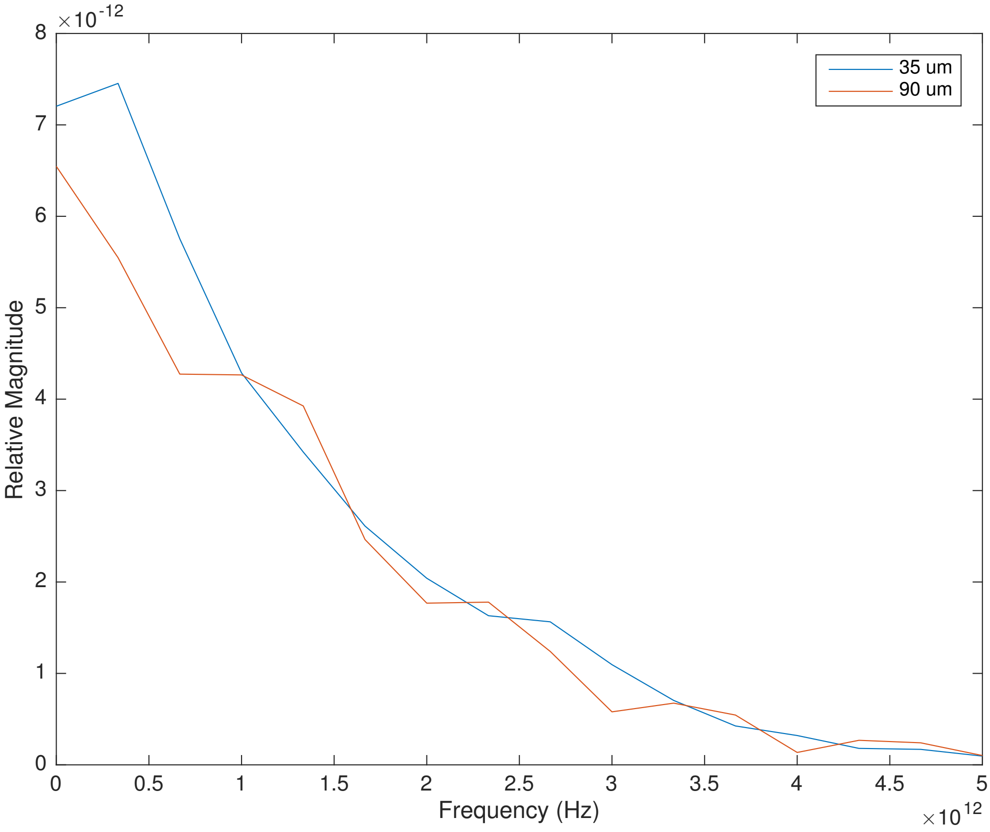

Figure 3.15: Fourier scans for the two cavity thicknesses reproduced in the model. While the range of frequencies present is much greater than in experimentation, the same FSR can be observed.

3.4 Conclusions

In this chapter I have compared the results from the model to different experimental results. I firstly used the same parameters given in chapter 2 to model an LPD emitter under a bias. I found that by using the mobility and diffusion constant curves from chapter 2 the model greatly overestimated the effects of drift compared to diffusion. I then set up a second model which assumed that the carriers heat up as they are excited and that it is the electron temperature that governs the ratio of D to mu. To do this, I set the diffusion and mobility to be equal to their values at the saturation field, as this gives the temperature of the carriers given by the Einstein relation to be around 2000 K, approximately equal to the temperature of 'hot' photoexcited electrons in GaAs take from literature. Under these conditions, I found that the results from the model gave qualitative agreement with experiment.

Secondly, I have performed an experiment in which a cavity is introduced to LPD emitters. Experimentally, the introduction of this cavity causes a broadening of the THz pulse and the creation of a free spectral range in the fourier spectrum. However, while the FSR range is clearly observable in the Fourier spectrum from the model, it also includes both higher and lower frequencies than those seen in experiment. While the presence of higher frequencies can be attributed to imperfect alignment of the experimental setup, the presece of the lower frequencies is most likely due to the lack of dispersion in the model. The broadening of the pulse in time was not observed in the model, however two peaks are observed in the results. This possibly indicates that the THz pulse should be broader in time than the model currently predicts. This disagreement between the model and experiment could possibly be due to the lack of dispersion in the model.

In order to verify the model further, an experiment could be performed in which the far-field emission of an LPD emitter as a function of detection angle is found. It would then be possible to compare the angular profile of the far-field emission between the model and experiment.

Chapter 4

Microwave Antenna

4.1 Introduction

The field of metamaterial research has attracted considerable attention in recent years due to the fabrication of metallic structures exhibiting both negative permittivity and permeability at certain resonant frequencies [45, 44]. The potential applications of such metamolecules are numerous, owing to the unique ability to engineer the material's refractive index, including negative refractive indices. While most metamaterials research has been focused on potential applications in free space, metamolecules loaded on to microwave waveguides have also been demonstrated [96, 97], allowing their easy incorporation into microwave circuits. Such applications of metamaterials in the microwave region include band-stop and band-pass filters [98, 99, 100, 101] and antennae [102, 103]. Metamaterials are attractive for antenna design for multiple reasons. Their subwavelength size opens up the opportunity for miniaturization[104, 105], a common aim in modern wireless technology. Furthermore, they show further uses in antennae for impedance matching[106, 107] and increasing bandwidth[108].

In the THz range there is a need for antennae in order to outcouple the THz radiation from emitters or to couple free space THz radiation into waveguide systems. Most methods used to generate THz rafiation, for example photoconductive antennas, have sub-wavelength dimensions[109]. Therefore, there is a problem of impedance mismatch between the device and free space[110]. One prominent example where out-coupling poses a difficulty is in the quantum cascade laser (QCL). QCLs are electrically pumped intersubband semiconductor quantum well lasers[111].

The first QCL emitted in the mid-IR was demonstrated by in Bell labs in 1994 by Faist et al.[112]. The first QCL operating in the THz regime was introduced, almost a decade later in 2002 by Tredicuccci et. al.[113]. In the initial design of THz QCLs the THz wave was guided by the top contact which served both as an electrical contact and also as a plasmon waveguide[114], giving an extended waveguide mode of approximately 100 μm or more. This type of device had excellent out coupling but very poor overlap of the laser mode and the active region of the laser. The poor overlap resulted to high threshold currents and poor temperature performance[115]. At MIT Qing Hu demonstrated the use of subwavelength double metal waveguides where the active region was sandwiched between two metallic layers[116, 117]. This creates a waveguide with a mode of approximately 10 μm, which is of course sub-wavelength. To outcouple from such devices, methods such as gratings[118, 119], photonic crystals[120] or horn antennae[121] must be used. Metamaterial antennae, such as the one investigated in this chapter, may represent an easier away to achieve outcoupling.

In this chapter, I present a metamaterial-inspired passive antenna incorporating both the fish-scale [122, 123] and split ring resonator (SRR) designs [45, 124, 125]. By coupling SRRs to a modified fish-scale, a hybrid structure was developed with a greater absorption than either component in isolation when loaded on a coplanar waveguide (CPW). We fabricated one sample that has only the fishscale design and one sample that has the hybrid metamolecule which incorporates the combination of the fishscale and the SRRs. The designs were first probed using the finite element method (FEM) using the commercial software package COMSOL Multiphysics and then tested experimentally using a vector network analyser (VNA). We show that there is excellent agreement between the simulations and the experimental measurements of the frequency response of the system. This permits us to use COMSOL to extract and compare the electric fields generated by the fishscale and those generated by the hybrid design. Furthermore, using COMSOL I show how varying the size of the structure affects the resonances of the SRR and the fishscale. COMSOL also predicts that at resonance the launched power is emitted and the hybrid metamolecule design acts as an antenna. To confirm this behaviour I compare its results with the experimental difference in losses between the fishscale and the hybrid sample and I find very good agreement. Finally, COMSOL was used to extract the antenna gain of the hybrid design as a function of direction and as a function of frequency.

4.1.1 Microwave Spectroscopy

On the whole, microwave spectroscopy presents an easier set of problems problem than THz-TDS. While the length scales involved in the THz region are on the order of millimeters, those involved in microwave spectroscopy are much larger, with the work in this thesis being in the 10 GHz region. Not only does this mean that accurate measurements can be taken while requiring less painstaking precision, it also allows the use of waveguides orders of magnitude wider which for obvious reasons are easier to manufacture and use. Furthermore, with microwave spectroscopy we have the added advantage of being able to generate signals with AC currents instead of the more novel and complex solutions required for THz-TDS.

At this frequency range, measurements are typically taken with a vector network analyzer (VNA). VNAs are microwave networks with the ability to read the voltage or apply a voltage at any port. Typically, most VNAs measure the S-parameters with a CW excitation. Therefore, to measure a spectrum one must sweep over range of frequencies of interest. Newer, more expensive VNAs can employ a pulse covering a range of frequencies. Much like analyzing the spectrum from a THz-TDS scan, one must then perform a fourier transform to examine the frequency response. Depending on the number of measurements that must be taken, using a pulsed VNA can drastically reduce the time required to perform a set of experiments. The incident voltages (V^{inc}) are related to the detected voltages (V^{det}) through the 'S-Matrix'

$$\begin{pmatrix} V_1^{det} \\ V_2^{det} \end{pmatrix} = \begin{pmatrix} S_{11} & S_{12} \\ S_{21} & S_{22} \end{pmatrix} \cdot \begin{pmatrix} V_1^{inc} \\ V_2^{inc} \end{pmatrix} \tag{4.1}$$

with the subscript indices representing each port. The S-parameters S_{ij} can be understood as the voltage at port i due to the applied voltage at j. Hence, S_{11} is the reflection at port 1 relative to the excitation at port 1. We can then understand that S_{11} and S_{22} are reflection coefficients while S_{12} and S_{21} are transmission coefficients. Two different microwave setups were used for the project in this thesis. In the first, a sample deposited on to a coplanar waveguide was connected at each end to a VNA by coaxial cables. Port 1 of a VNA was then used to excite one end of the coplanar waveguide, with the transmission and reflection coefficients being taken as S_{21} and S_{11} respectively. Due to the simple nature of the setup, this was able to be performed without difficulty. The VNA used for this measurement had a range of 2-20GHz, though in reality measurements could only be performed up to 18 GHz as thiswas the upper limit of the coaxial cables used to connect the VNA to the sample.

For the far field measurements, an anechoic chamber was used in which one end of the waveguide being tested was excited by a VNA. The second port of the VNA was connected to a horn antenna so that the transmission could be detected in the far field at multiple angles by rotating the sample relative to the antenna. This experiment was performed with a pulsed VNA, which allowed for measurements to be taken up to 18 GHz for a large range of angles. An illustration of this setup can be seen in fig. 4.1.

4.2 The Finite Element Method

Unlike finite difference methods, which discretize functions, the finite element method discretzes the underlying space[126]. One large advantage of FE is that the elements

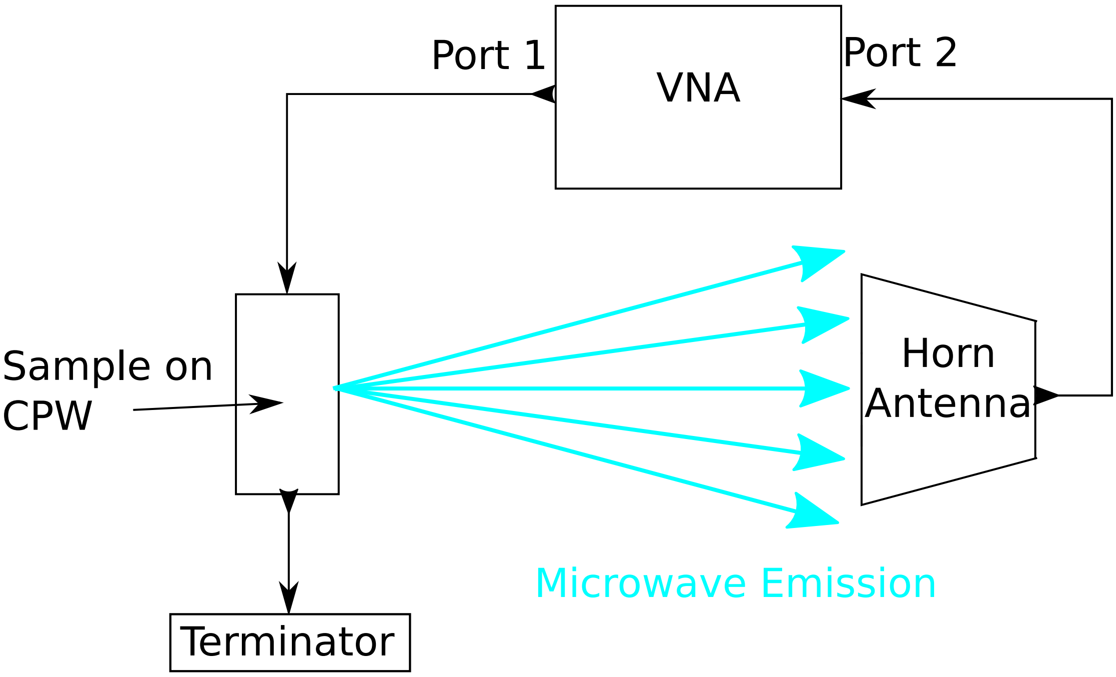

Figure 4.1: The setup used for far-field measurements of microwave emitters.

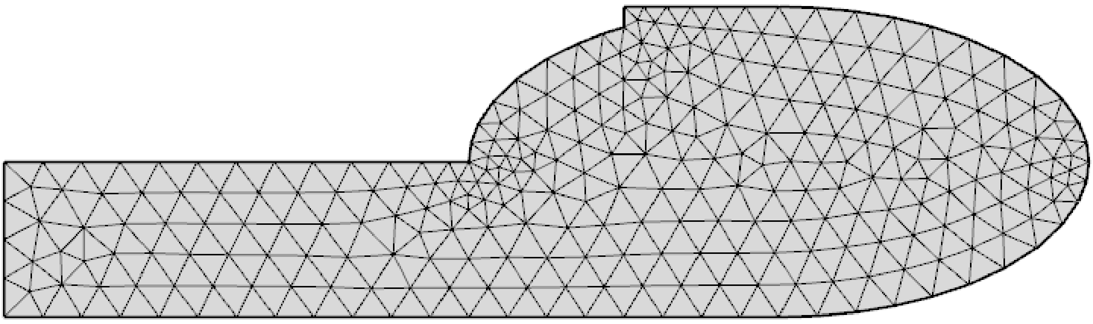

Figure 4.2: An example of an FEM mesh used to discretize a complex geometry.

need not be regular tetrahedra as in FD, rather they can irregular triangles or quads in 2D and tetrahedra, pyramids, prisms or tetrahedra in 3D. For this reason, geometries that involve complex shape which cannot be well meshed through regular quads are much better solved using FE than FD. Also, while FD is used to solve differential equations, FE is used to solve integral equations[127]. This means that for each approach, we must pose the problem differently. The first step in FEM is to convert the equation in to some form we can use.

4.2.1 Strong to Weak Formulation

Before we can solve a partial differential equation using FEM, we must first convert that equation from its strong to its weak form[128]. Let us look at Poisson's equation in 2D and define it on the domain $\Omega \in \mathbb{R}^2$ using use homogenous dirichlet boundary conditions. This gives

$$-\Delta u(x) = f(x), \qquad x \text{ in } \Omega \tag{4.2}$$

$$u(x) = 0, \qquad x \text{ on } \delta\Omega \tag{4.3}$$

In FEM parlance, we would call this the 'strong form' of the equation. To get the weak form of this equation, we first multiply it by an arbitrary 'weight function', $v(x, y)$, and then integrate to obtain

$$\int_\Omega v\Delta u = \int_\Omega fv \tag{4.4}$$

Integrating by parts, we get

$$\int_\Omega v\Delta u = \int_\Omega \nabla(v\nabla u) - \int_\Omega \nabla v \cdot \nabla u \tag{4.5}$$

Gauss's theorem states that

$$\int_\Omega \nabla(v\nabla u) = \int_{\delta\Omega} v\nabla u \cdot \hat{n} dS \tag{4.6}$$

which from eqn. 4.3 will be equal to zero. Therefore, combing eqns. 4.2 with 4.5 we get

$$\int_\Omega \nabla v \cdot \nabla u = \int_\Omega fv \tag{4.7}$$

This is what would be called the 'weak formulation'. The primary difference between the strong and the weak form is that the strong form is required to be continuously differentiable until the second partial derivative[129]. Because in the weak form we have transferred one of the partial derivatives on to the weight function, it is required to be continuously differentiable until only the first partial derivative[130]. Furthermore, while the strong form of the equation tells us what is happening at each point in the domain, the weak form tells us only what is happening over the entire domain as a whole.

4.2.2 Descretization

While in finite difference methods the data is located at the nodes of the mesh, in FEM the data is located in the space between the nodes, known as 'elements'. Let us take 7

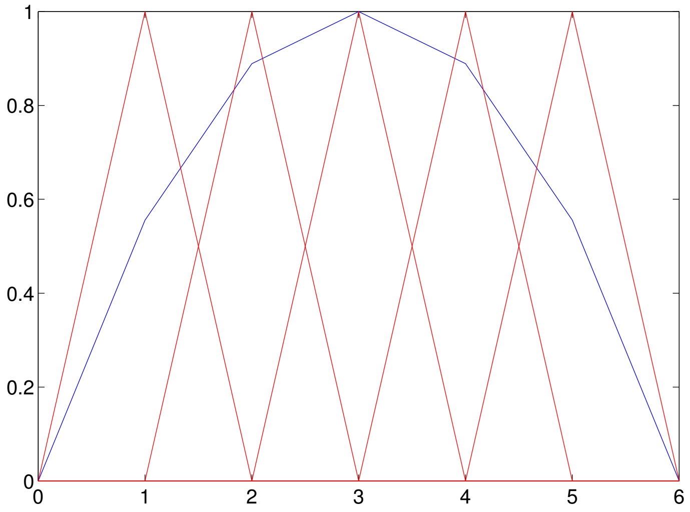

Figure 4.3: The blue line shows a an approximate solution we hope to reach. The red lines show the basis functions at each internal node.

nodes, denoted as x_j where $j = 0, ...6$. At each internal node is located what is called a basis function, which we will denote ϕ_i, with $i = 1, ...4$. Each basis function is zero on all nodes other than the node on which it is located[131]. In other words,

$$\phi_i(x_j) = \delta_{ij} \tag{4.8}$$

Fig. 4.3 shows a the approximation of a function we hope to arrive at in blue along with the basis functions in red. It can also be seen that each basis function is non-zero in its two neighbouring elements. Let us designate our solution as $u(x)$. We can approximate u as a linear combination of these basis functions

$$u(x) = \sum_{i=0}^{6} c_i \phi_i(x) \tag{4.9}$$

where c_i are unknowns to solve for.

Therefore, if we can find the coefficients c_i we can find the approximate solution $u(x)$.

4.2.3 Galerkin Method

Let us go back to the weak formulation of Poisson's equation (eqn. 4.7). Using our basis ϕ let us say[132]

$$u(x) = \sum_{j=1}^{N} c_j \phi_j(x) \tag{4.10}$$

$$v(x) = \sum_{j=1}^{N} b_j \phi_j(x) \tag{4.11}$$

where c_j are unknowns to solve for, N is the total number of elements, including boundaries. b_j is arbitrary as we will cancel it out later. After placing this in to our weak form and rearranging, we get

$$\int_\Omega \sum_{j=1}^{N} c_j \nabla\phi_j \sum_{i=1}^{N} b_i \nabla\phi_i = \int_\Omega f \sum_{j=1}^{N} b_j \phi_j(x) \tag{4.12}$$

which rearranges and cancels to

$$\sum_{j=1}^{N} c_j \int_\Omega \nabla\phi_j \nabla\phi_i = \int_\Omega f\phi_i \tag{4.13}$$

We can now turn this in to a matrix problem of the form

$$\mathbf{Kc} = \mathbf{F} \tag{4.14}$$

where c is a vector of our unknowns, c_j

$$K_{ij} = \int_\Omega \nabla\phi_j \nabla\phi_i \tag{4.15}$$

and

$$F_i = \int_\Omega f\phi_i \tag{4.16}$$

We are now able to solve this equation using standard methods from linear algebra. In this thesis, all FEM work is used to solve the frequency domain electromagnetic wave equation

$$\nabla \times \frac{1}{\mu_r} \nabla \times \mathbf{E} - k_0^2 \epsilon_r \mathbf{E} = -ik_0 Z_0 \mathbf{J} \tag{4.17}$$

All FEM simulations included in this thesis were performed with the use of COMSOL Multiphysics.

4.2.4 Perfectly matched layers

Perfectly matched layers (PMLs) present an absorbing domain with extremely low reflection. Unlike ABCs which as the name tells us are boundary conditions, the PMLs are instead domains defined at the edge of the simulation. They are called ‘perfectly matched’ because the impedance at the PML boundary is set to be equal to that of its neighbouring domain. A damping constant is applied to the waves inside the PML so that any wave that enters will attenuate to approximately zero before it reaches the edge of the simulation[133]. In mathematical terms, we apply the transformation

$$\frac{\delta}{\delta x} \rightarrow \frac{1}{1+i\frac{\sigma(x)}{\omega}} \frac{\delta}{\delta x} \tag{4.18}$$

to our differential equation at all points inside the PML domain. The outer PML boundary can therefore be defined as anything we want; there is no need to worry about reflections from the outer PML boundary because the waves will continue to attenuate as they travel back towards the inner domain. So long as our PML is well defined and thick enough, spurious reflections from the outer PML edge should pose no problem. Minor reflections will occur from the inner PML edge due to the discretization. If these are too large, then decreasing the mesh size of the problem will help to further remove them.

One disadvantage to PMLs when compared to absorbing boundary conditions is their relatively longer time to compute. Since ABCs only exist on a boundary, they are essentially one element thick. PMLs, being a domain, can cause a noticeable increase in the time required to solve the problem if their thickness is too great.

4.3 Metamolecule Design

The design of the antenna under investigation and its dimensions are detailed in fig. 4.4. The antenna was inspired by the fishscale metamolecule design and the concentric double SRR. The fishscale pattern was modified by replacing the characteristic ‘U’ shape with a ring of sector angle 270°. The inner radius of each loop was 1.7 mm and the outer radius of each loop was 1.9 mm (fig. 4.4(a)). The resulting structure was found to resonate at microwave frequencies.

Inner split rings were then added to one half of the design as shown in fig. 4.4(b). Each inner split ring has a sector angle of 320°. It was hoped that each inner SRR and its surrounding fishscale would couple with one another in the same manner as a double SRR.

The final metamolecule design is presented in fig. 4.4(c).

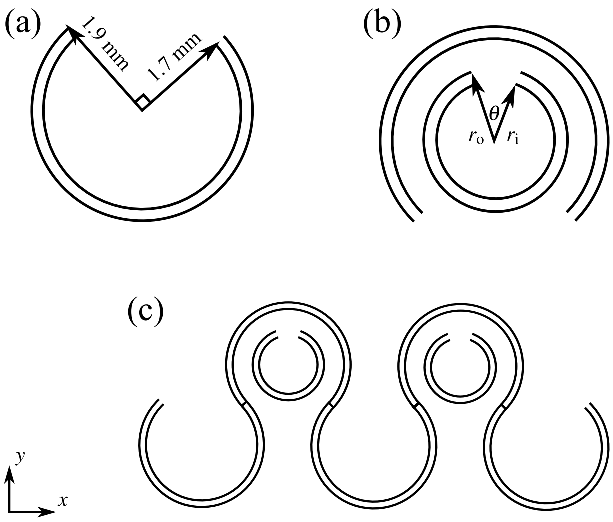

Figure 4.4: (a) The geometry and dimensions of one unit segment of the modified fish-scale structure. (b) The geometry of a fish-scale segment complete with inner ring to form a SRR. The angular gap θ used for the inner split ring is 40°. (c) The final hybrid fishscale/SRR metamolecule. In the finalised design, $r_o =$ 1.1 mm and $r_i = 0.9$ mm.

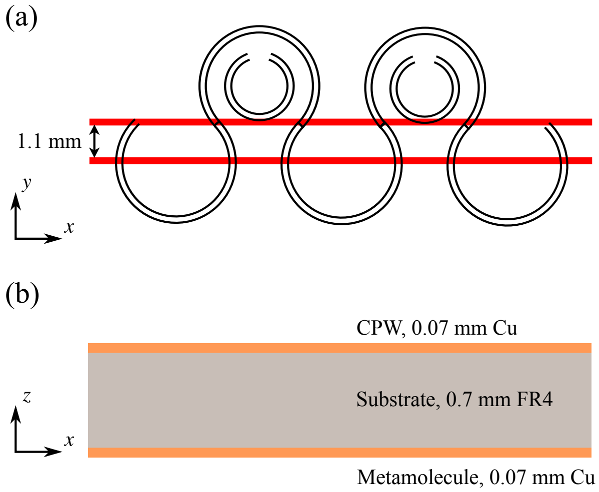

Figure 4.5: (a) Top-down view of the hybrid structure on the CPW with placement relative to the CPW gaps (shown in red). (b) View from the side of the same sample showing the dimensions of the device layers.

When designing the structure, it was chosen that the fishscale should be exposed to asymmetric driving fields in order to prevent the generation of equal and opposite currents inside the structure. For this reason, the centre of the fishscale in the y-direction was located directly in line with one of the CPW tramlines.

The placement of the metamolecule relative to the CPW is shown in fig. 4.5(a). The CPWs were also centrally placed above the same tramline, again to ensure that they experienced an asymmetric driving field. Furthermore, the electric fields produced by each tramline of a coplanar waveguide cancel above the conduction strip, so placement over a tramline also ensured that the SRR experienced a strong electric field. The final placement of all the components was checked using COMSOL to ensure good coupling between the SRRs and fishscale.

The metamolecule itself is 0.07 mm thick and fabricated from copper. It was separated from the CPW by the CPW substrate, namely a 0.7 mm thick layer of FR4 circuit board. (Fig. 4.5(b)). The conduction and ground planes of the CPW were also made from copper and also with a thickness of 0.07 mm. The tramlines are each 0.2 mm wide separated by a central conduction plane with a width of 1.1 mm(Fig. 4.5(a)). Such a design, being based on the mutual coupling between the waveguide and the antenna requires no line feeding.

4.4 Numerical Investigations

Before performing fabrication and experimentation, the design of the metamolecule was first studied in COMSOL. The aim was to find appropriate dimensions for the SRRs so that they would couple to the fishscale structure. Firstly, the geometries of the CPW and fishscale structures were described to COMSOL. PMLs were also introduced in the form of a cylindrical domain encompassing the entire structure. While a sphere may seem the obvious choice for a full analysis of the far field, the domain becomes much more complex, leading to a great increase in the computation time and difficulty in creating the mesh. Each end of the CPW was attached to SMA end launch connectors identical in size and geometry to those used in experimentation. Half of each end launch connector is encompassed within the PML, while the exposed metal is defined as a PEC and the coaxial dielectric as a port. It was then possible to excite the system at a certain frequency by applying a signal to one of the end launch connectors. In this manner, it was possible to extract the scattering matrix parameters of the system in order to characterise the system and, later, compare the results to experimentation.

The numerical investigation predicted that the fishscale would produce a resonance at around 16 GHz. I found that, by setting the inner radius of the SRRs to 0.9 mm and the outer radius to 1.1 mm, coupling between the two components produced a stronger resonance than either component in isolation as shown in fig. **??**. The final dimensions are shown in Fig. 4.4 and Fig. 4.5.

Three different simulations were performed. One include only the fishscale and CPW, on included only the SRRs and CPW while the final one included the entire final structure. The SRRs produce a resonance at around 15.2 GHz, while the fishscale produces a resonance at around 15.7 GHz. The hybrid structure also produces a resonance at 15.7 GHz, though stronger than that of the fishscale in isolation. This suggests a hybrid mode produced by coupling between the SRRs and fishscale.

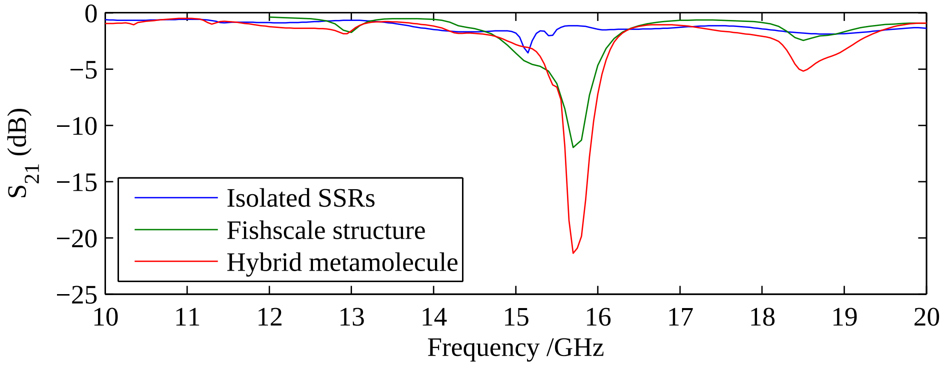

Figure 4.6: Shown above the calculated S_{21} for the SRRs (red), the fishscale (blue), and the hybrid SRR and fishscale structure (green).

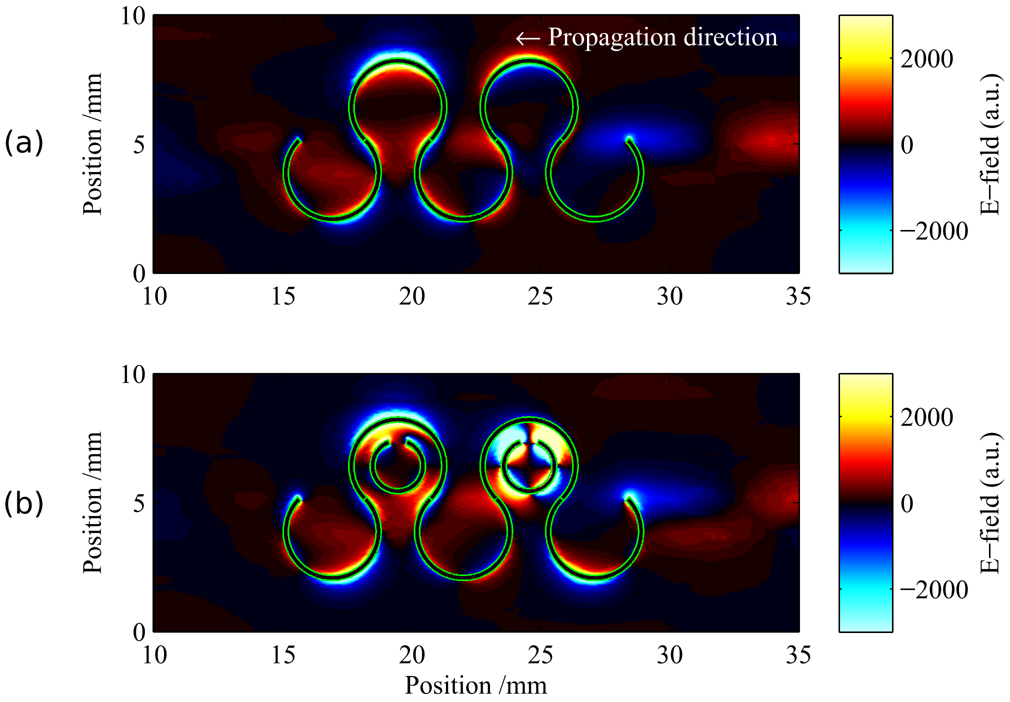

Figure 4.7: Electric field maps produced by the CPW-loaded structures determined using COMSOL simulation. The y-polarized electric fields (according to the geometry of Fig. 4.4 and perpendicular to the propagation axis) for both the isolated fishscale (a) and hybrid structure (b) are shown. The structures were excited by a coaxial port from the right hand side of the figure.

To see the coupling between the SRRs and fishscale, the simulated electric fields produced perpendicular to the propagation axis for the fishscale and hybrid structure are shown in fig 4.7. This polarisation was was chosen as it effectively shows the coupling between the two structures.

Evidence of coupling can be found in the electric field present between the SRR closest to the input port and the surrounding fishscale. This can be seen in the right hand side of fig 4.7(b). The field in this region deviates from that of the isolated fishscale when the SRRs are introduced. Namely, the polarity of this field has changed and now closely follows that of the SRR.

It can also be seen that the polarity of the electric field produced along the outer edge of the fishscale in the hybrid structure is opposite to that of the electric field produced by the same region when no SRRs are present. This change in polarity when the SRRs are present can be seen by noticing the change in, again, the right hand region between figs. 4.7(a) and 4.7(b). Noticeably, this does not apply to the region of the fishscale surrounding the second SRR further along the direction of propagation. It can also be seen that the excitation surrounding this SRR is noticeably weaker than that of the other. It is possible that this is due to the absorption and reflection of the incoming EM wave by the first SRR, leading to a much weaker signal reaching the second SRR. When the input is swapped to the other port in the simulation, the electric fields produced are the mirror image of those in fig. 4.7.

4.5 Experimental Results

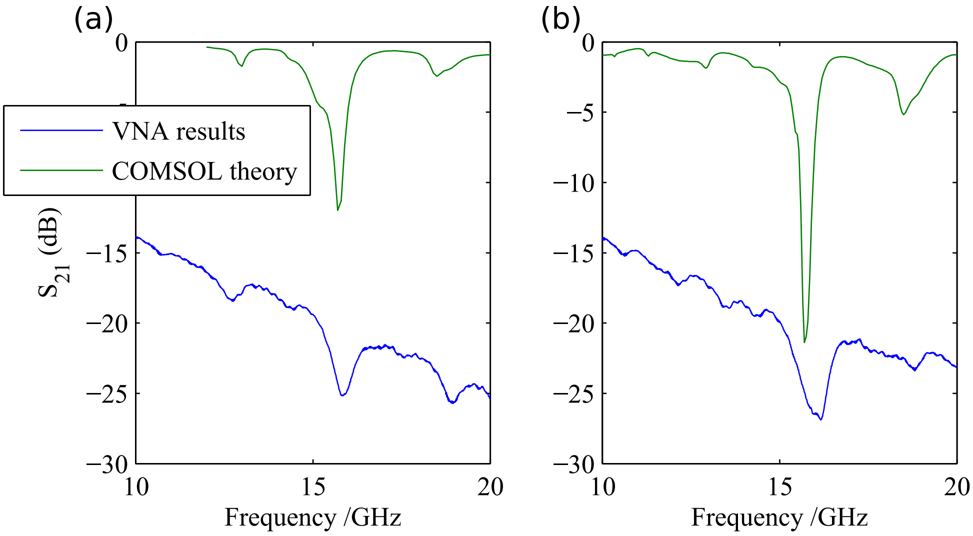

Figure 4.8: Comparison of computational results (green) with experimental results (blue). The S_{21} for the fishscale is shown in (a) and that of the hybrid structure is shown in (b).

As mentioned, physical samples of both the fishscale and hybrid structures were created on the underside of ungrounded CPWs. The dimensions of the waveguide structures are those shown in Fig 4.4, which were modelled in COMSOL. A comparison of the S_{21} for both the physical and numerical results is shown in Fig. 4.8, where it can be seen that the enhancement of the fishscale resonance is verified experimentally. There is an approximately 0.4 GHz shift between simulation and experiment in the position of each resonance, perhaps due to the limitations of the mesh size in COMSOL, slight innacuracies in the dimensions of the physical sample, or slightly innacurate material paremeters.. Both the absorption of the isolated fishscale mode and hybrid mode are not as prominent in the experimental investigations when compared with the numerical results. This may be attributed to the presence of much greater resistive losses in the experimental setup. The percentage decrease in transmission between the experimental results is around 50%, whereas between the computational results it is around 80%. This difference in results is likely due to the lack of a damping coefficient used in the FEM model. In reality, energy would be lost to the dielectric due to the imaginary part of the refractive index. Since in the model the refractive index is entirely real, no energy is absorbed by the substrate, which could explain the difference between the experimental and computational results.

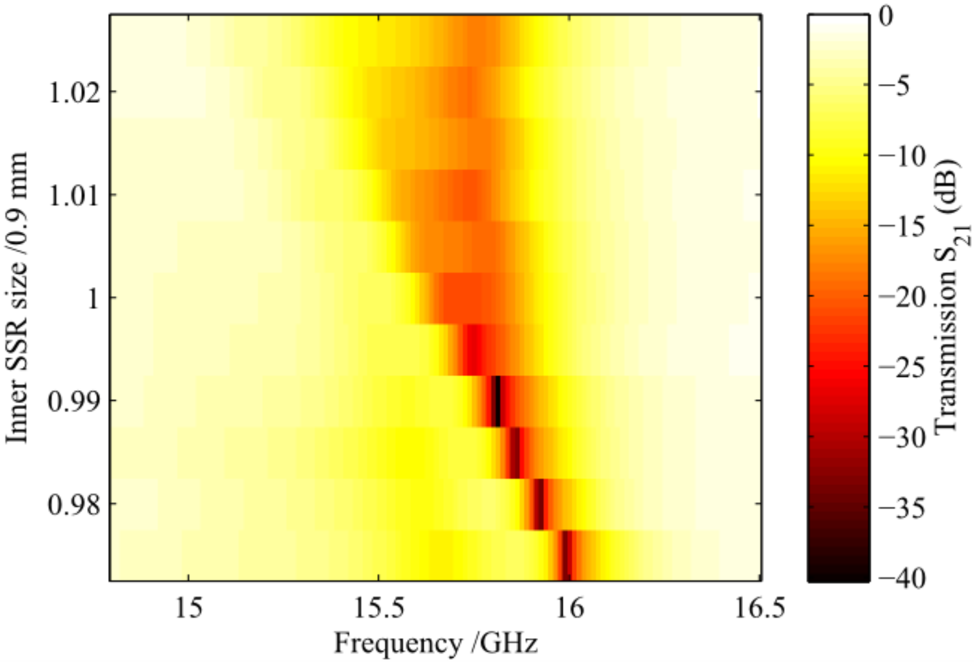

Figure 4.9: Absorption as a function of frequency and SRR size, normalised to the inner radius of the original SRR dimension, which is 0.9 mm. At smaller SRR sizes, both the original fishscale resonance and SRR introduced resonance can be identified separately. For the smallest geometry geometry, the fishscale resonance can be seen on the left while that of the SRRs is seen on the right.

4.6 Effect of SRR size on resonant properties

A further numerical investigation was performed to determine how changes in the sizes of the SRRs affect the coupling of the SRRs to the fishscale mode and the resonant properties of the hybrid structure. In COMSOL, the radii of the SRRs were altered, the

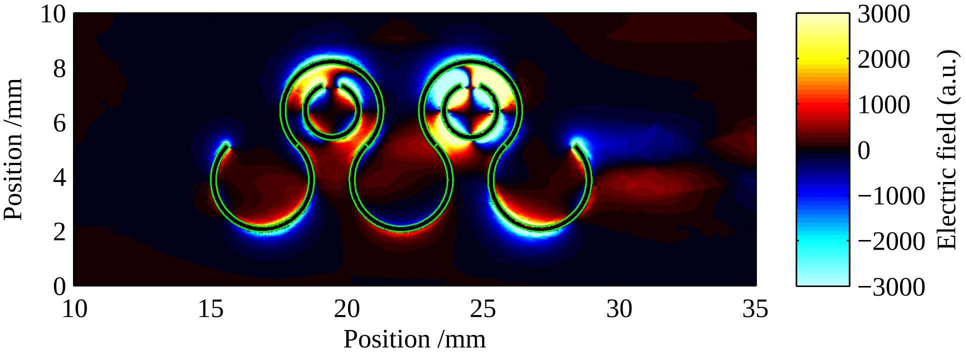

Figure 4.10: The y-polarization of the electric fields produced by the hybrid structure with SRRs 0.98 times the original size at the resonance around 15.9 GHz.

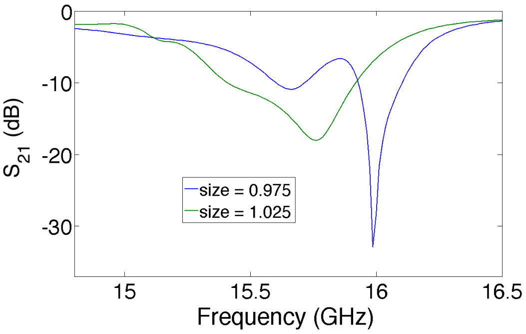

Figure 4.11: Absorption as a function of frequency of frequency for the two most extreme SRR sizes shown in Fig. 4.9. The scan for $r_i = 0.9$ mm $\times 0.975$ is shown in blue, where hybrid mode can be seen on the right while the fishscale mode can be seen on the left. The scan for $r_i = 0.9$ mm $\times$ 1.125 is shown in green and the fishscale mode can be seen in approximately the same place, while the hybrid mode is starting to appear on the left.

size of the radius of each SRR was altered whilst maintaining the SRR's track width at 0.2 mm. The fishscale size was kept constant and the overall absorption of the hybrid metamolecule for each size is presented in Fig. 4.9. The strength of the resonance is affected by tuning the size of the SRRs, the greatest absorption is obtained with SRRs 0.99 times the original size. In Fig. 4.9 two separate modes of the hybrid metamolecule around the area of interest can be observed. For example, for SRR sizes of 0.98 times the original size, the lower frequency resonance of the hybrid metamolecule present at 15.5 GHz is dominated by the fishscale mode and it is present when the SRRs are removed. The resonance of the hybrid metamolecule present at around 15.9 GHz is linked to the presence of the SRRs. In Fig. 4.10, we show the y-polarization of the electric fields in the hybrid metamolecule with SRRs 0.98 times those used to obtain Fig. 4.7(b). Note the large increase of the electric field strength, in Fig. 4.10 in relation to Fig. 4.7(b). The concentration of the electric fields generated at this frequency surrounding the SRRs further demonstrates that this mode is dominated by the SRRs. Evidence of coupling between these two modes of the hybrid metamolecule is apparent in Fig. 4.9 by the shift in frequency of the fishscale mode as the size of the SRRs is altered. The shift of these resonances can be more clearly observed from Fig. 4.11. The shift is specified in relation to the original inner radius that is 0.9 mm. For the smaller SRR size (0.9 mm × 0.975), shown in blue, the SRR mode is observable on the right while the fishscale mode is observable in the centre. For the larger SRR size (0.9 mm × 1.125), the fishscale mode can be observed in approximately the same place, though the SRR mode has started to appear on the left. It is hoped that by extending the length of the structure, it would be possible to tailor SRR sizes to produce stronger yet resonances. As shown, size variation of the SRR structure in the order of 10 μm greatly affects the strength and frequency of the metamaterial response. It is possible that the geometry of the fabricated structure was slightly different to that designed leading to small discrepancies in absorption and frequency between the experimental and computational results shown in Fig. 4.8.

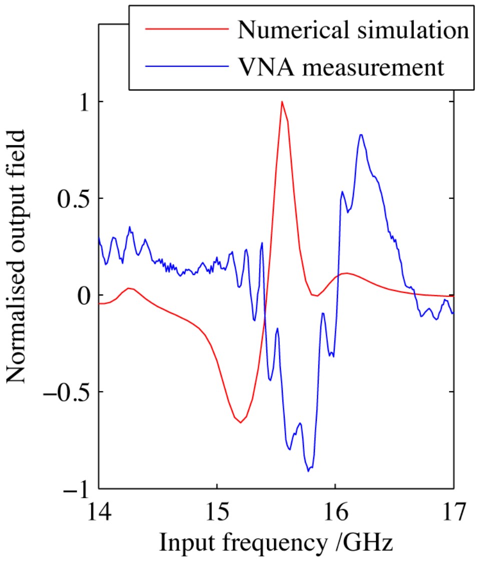

Figure 4.12: The comparison between the differences between P_{lost} for the hybrid structure and that of the fishscale is shown in (a). The experimental results are in blue while the computational results are in red. The frequency shift (about 0.5 GHz) of the resonance between the two sets of results is consistent with the previous computational results shown in Fig. 4.8.

4.7 Use as a radiative antenna

To demonstrate its properties as a radiative antenna, the radial emission from the metamolecule-CPW structure was first analyzed as a function of frequency in COMSOL. As expected, COMSOL predicted that maximum radial emission from the structure was greatest at the frequency of the hybrid mode. To initially verify this behaviour using the experimental data, the ratio of the total losses across the CPW to the input power as a function of frequency were calculated using $P_{lost} = 1 - |S_{21}| - |S_{11}|$.

By calculating this value for the isolated fishscale and the hybrid structure,it was possible to subtract the losses of the former from the latter, the change in overall loss when the SRRs are introduced can be examined. This experimental value can be compared with an equivalent P_{lost} taken from the COMSOL model. The difference in P_{lost} is calculated from the model in the same way as the experimental data; by subtracting the radial power outflow of the fishscale from that of the hybrid structure as a function of frequency. The experimental and simulation results are in good agreement with each other as shown in fig. 4.12, albeit with a shift in frequency consistent with the previous comparisons of computational and experimental data, shown in Fig. 4.8.

From these results we can see that the introduction of the rings to the physical sample caused an increase the power lost at the resonant frequency. Since the rest of the experimental setup remained the same between these results, it is reasonable to assume that the increase in power loss is due to an increase in emission from the metamolecule. This is the behaviour also predicted by COMSOL.

4.8 Measured Far Field

The sample was placed in an anechoic chamber. The sample was launched by a VNA at one end, with a microwave terminator attached to the other. The sample was then rotated relative to a horn antenna connected to the second port of the VNA. It was therefore possible to measure the far field emission as a function of angle. A local maxima was found in the far field at around 16.2 GHz, agreeing with the location seen in Fig. 4.12.

I now present a comparison of the modelled and experimentally measured far field for electric field polarisations both along the length of the CPW (figs. 4.13 and 4.14) and perpendicular to the CPW plane (figs. 4.15 and 4.16). While qualitatively similar to the calculated far field in COMSOL, both sets of experimental results appear to be rotated by about 90° when compared to their computational counterparts. This model contained a cylinder in close proximity to the waveguide with an relative permittivity of 2 to roughly model the wooden support attached to the waveguide as shown in fig. 4.17.

It is hard to determine exactly why these results show an angular shift when the experimental results are compared with the theory, though there are several potential causes. Firstly, the metal mounts by which the VNA connections were attached to the CPW, and the screws by which the CPW was attached to the wooden mount were not modelled. The presence of a conducting material in close proximity to the emitter would effect the emitted field, which would then lead to a discrepacy between the measured and modelled far fields. Secondly, only an approximation of the permittivity of the wooden support was made, and changes in this value would again effect the measured far-field. Furthermore, microwave radiation emitted from elsewhere in the setup may have caused interference in the far-field pattern. Finally, the manner in which the rotation was measured on the mount was rather crude, which likely lead to a small error in measuring the angle of rotation. There are several ways in which this experiment could be improved. By performing the same experiment with an unloaded CPW of the same geometry as that used in experiment, it would be possible to subtract the emission detected from that of the sample loaded on to a CPW, highlighting the effects of the presence of the metamolecule. A sample holder with a known permittivity would aid in the computer modelling of the experiment, allowing better comparison between the experimental and simulated results. Finally, a more precise experimental setup would help to obtain accurate results.

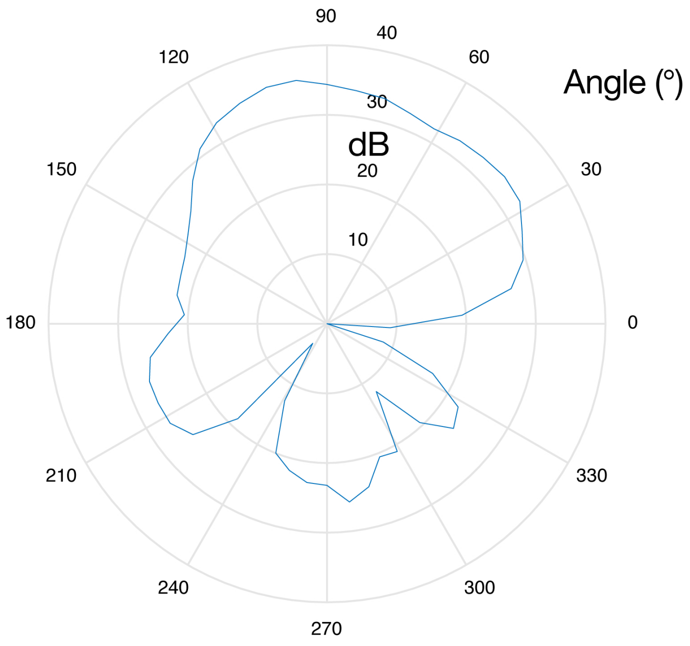

Figure 4.13: The modelled far field at resonance as a function of angle for the polarisation parallel to the length of the CPW. The scale is in dB.

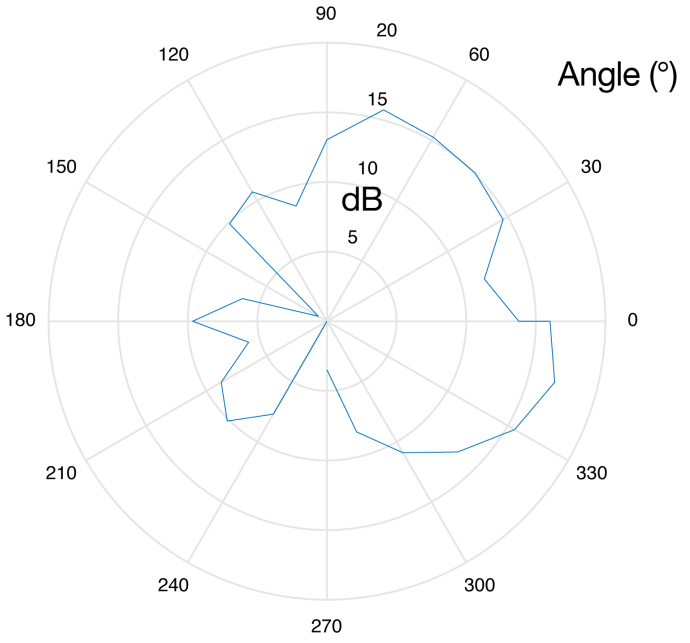

Figure 4.14: The experimental far field at resonance as a function of angle for the polarisation parallel to the length of the CPW. The scale is in dB.

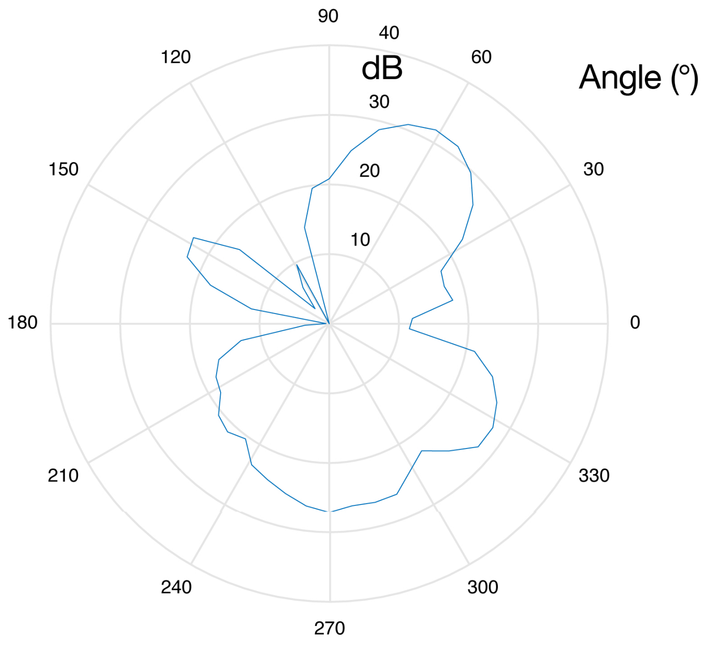

Figure 4.15: The modelled far field at resonance as a function of angle for the polarisation perpendicular to the plane of the CPW. The scale is in dB.

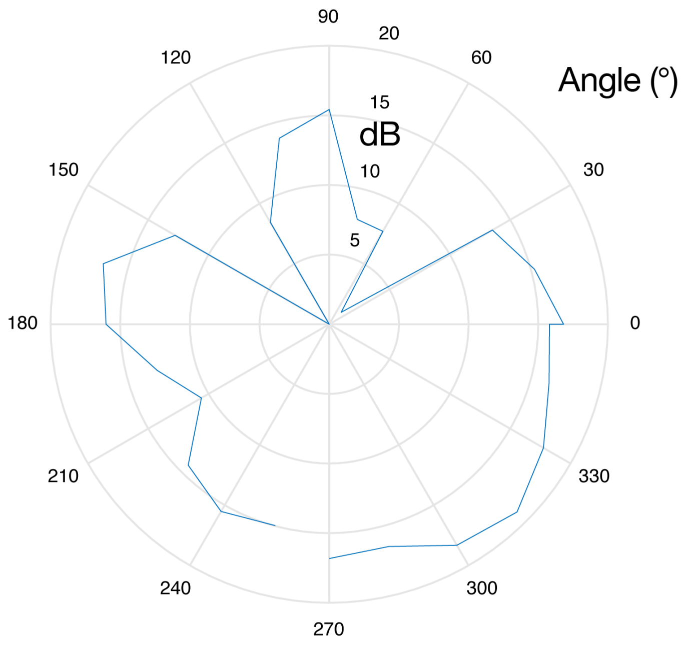

Figure 4.16: The experimental far field at resonance as a function of angle for the polarisation perpendicular to the plane of the CPW. The scale is in dB.

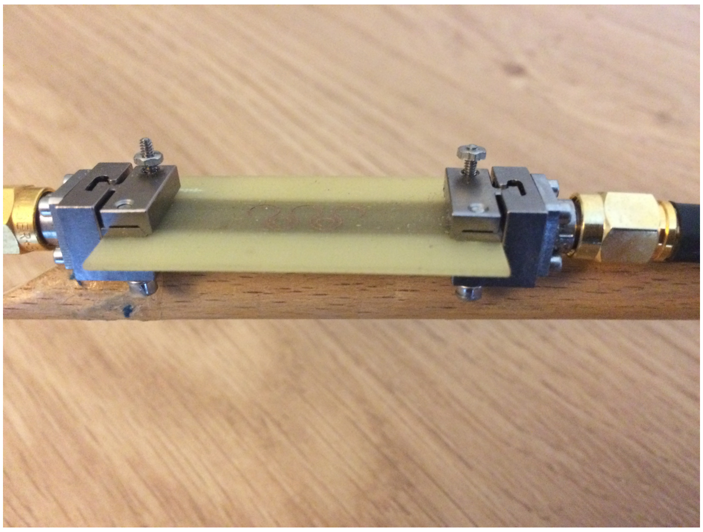

Figure 4.17: A photograph of the sample and the wooden support used for the far-field measurements.

4.9 Conclusions

A novel metamolecule antenna based on the fishscale and SRR designs has been presented and discussed. Its properties have been examined theoretically, using COMSOL, and experimentally, using a VNA in conjunction with a CPW.

The COMSOL model predicts the emission of microwave radiation at the fish-scale/SRR hybrid mode. This emission was also found experimentally by comparing the losses from a fishscale/SRR structure and those from only a fishscale structure. Far-field measurements were performed, and although the features highly resembled those from the computational model, an angular shift in the far field profile between the two models was found. This difference in the far-field profiles could be due to the crudeness of the mount or an incomplete computational model, or a combination of the two.

Unlike most CPW base antenna designs, no line feeding is required. The antenna is driven via the mutual coupling which exists between fish-scale/SRR combination and the CPW. This feature offers the prospect of rapidly interchangeable frequency dependent antennae. In practice it should be possible to optimize antenna gain by increasing the quality factor Q of the fish-scale/SRR combination. The angular profile of the emission can be tuned by changing the number of metamolecules used for the design and of course the shape of the hybrid metamolecule. In addition, it should also be possible to increase the mutual coupling by (i) decreasing the distance between the antenna and CPW, and (ii) finding the optimum placement of the CPW gaps with respect to the fish-scale/SRR combination. Furthermore, it could be possible to tune and affect the absorptive and emission properties via coupling to the FMR resonance of a magnetic material, as outlined in [96].

Chapter 5

Conclusions

In this thesis I have furthered the modelling of lateral photo-Dember emitters. I introduced a model based on a 2D solution of the drift diffusion equation in which the solved currents are fed in to a finite difference time domain model. The results from the FDTD code are then fed i to a far-field algorithm which is able to model the signal received by a detector.

From my results I have found that the previous 1D model by Barnes et. al. is incomplete and essentially classical and lateral photo-Dember should not be treated as separate 1D problems. The surprising but obvious result is that the metallic edge reorients the emission of the classical PD currents as it does for the lateral current. I show that the dynamics of the system are dependent on the currents travelling perpendicular to the semiconductor surface, as opposed to just the lateral currents as previously thought. I then go on to compare this model with experimental results. The first experiment in question involved the examination of photo-Dember emission when the semiconductor is under the influence of a biasing electric field and I find that my model agrees with the results but only for high carrier temperatures. I also performed a separate experiment in which a gap was introduced to various lateral Photo-Dember emitters in order to observe its effects in both the time and frequency domains.

I also present a novel microwave antenna based on the fishscale and split-ring resonator metamaterial designs. I demonstrate that mutual coupling between the fishscale and SRRs is responsible for creating a greater absorption of the input signal than either component is capable of in isolation. The antenna was tested, and I compare the experimental results with the computational model.

5.1 Modelling the Lateral Photo-Dember effect

In chapter 2, I presented a model utilising both a drift-diffusion solver and the standard FDTD algorithm to investigate the lateral photo-Dember effect. In the 2D DD model I used the Scharfetter-Gummel discretization and take in to account various recombination rates as well as field depended diffusion and mobility. Then, the results of the FDTD model were fed into a far-field algorithm that adds the contributions of different angles therefore making it possible to model details of the experimental geometry, such as the acceptance angle of lenses.

My model being 2D predicts that the LPD effect is in fact governed by the currents travelling perpendicular to the surface of the semiconductor, as opposed to the currents travelling lateral to the surface as previously thought. Several more improvements were made to the model in contrast with the one presented by Barnes et. al. Firstly, the drift diffusion model I have uses a realistic level of excitation, causing the drift to play a far greater role in the dynamics than predicted by Barnes. Secondly, my model incorporates a more realistic form of Shockley-Read-Hall recombination, as well as including radiative recombination and Auger recombination. The model also includes field dependent diffusion and mobility.

For future work, it should be possible to extend the validity of the model by using the hydrodynamic model as opposed do the DD model. The hydrodynamic model models carrier dynamics by taking in to account carrier temperatures and quasi-Fermi potentials and other fixed parameters that satisfy particle energy and temperature distributions in each valley in the material.[64] Since I have made my model modular, such a transport model could be easily plugged in to the existing FDTD code.

Experimentally I think that a beam profile of the THz e-field has to be achieved in order to compared with the results of my model, but maybe this should be done after the carrier dynamics are upgraded to the hydrodynamic model.

5.2 Experiments on the Lateral Photo-Dember effect

In chapter 3 I compared various results for the model against experimentation.

Firstly, I compared the results of a photo-Dember emitter illuminated with a biasing electric field applied. I found that by using the mobility and diffusion curves in chapter 2, I was unable to recreate the results of the experiment. However, by assuming an electron temperature of 2000 K, I was able to find good qualitative agreement between the experiment and the model. This would indicate that the curves used in chapter 2 are only particularly useful for describing low injection conditions. Again, I find that the phenomenon is not accurately described by the lateral currents, and those perpendicular to the surface must also be accounted for.

Secondly, I performed an experiment in which a gap was introduced between the semiconductor surface and the metal mask. By introducing a spacing, it was possible to extend the length of the temporal pulse. Fourier transforms of these results demonstrate a free spectral range dependent on the thickness of the cavity.

5.3 An Investigation in to a Novel Microwave Antenna

In chapter 4 I presented and tested a novel microwave antenna.

I designed a metamolecule based on the previously existing split ring resonator and fishscale designs. I found that it was possible to create a greater resonance than either component exhibits in isolation by coupling the two designs.

I found that the design acts as an antenna when loaded on to a coplanar wave guide. Experimentation and a COMSOL model of the system were in good agreement, and a peak in the radial transmission of the antenna was found to accompany the resonance in each. Furthermore, the antenna is able to couple directly to the CPW without the need for line feeding. Such a metamolecule design could be used in THz quantum cascade lasers where the out-coupling is particularly problematic.

References

[1] V Apostolopoulos and M E Barnes. Thz emitters based on the photo-dember effect. *Journal of Physics D: Applied Physics*, 47(37):374002, 2014.

[2] D. McBryde, M. E. Barnes, S. A. Berry, P. Gow, H. E. Beere, D. A. Ritchie, and V. Apostolopoulos. Fluence and polarisation dependence of gaas based lateral photo-dember terahertz emitters. *Opt. Express*, 22(3):3234–3243, Feb 2014.

[3] Mark E. Barnes. *Terahertz emission from ultrafast lateral diffusion currents within semiconductor devices*. PhD thesis, University of Southampton, 2014.

[4] L. C. Maple, S. A. Berry, G. B. G. Stenning, G. J. Bowden, P. A. J. de Groot, and V. Apostolopoulos. A metamolecule antenna for coplanar waveguides. *Opt. Express*, 22(25):30473–30481, Dec 2014.

[5] Masahiko Tani, Kiyomi Sakai, and Hidenori Mimura. Ultrafast photoconductive detectors based on semi-insulating gaas and inp. *Japanese Journal of Applied Physics*, 36(9A):L1175, 1997.

[6] V. L. Malevich. Monte carlo simulation of the dember effect in n-inas exposed to femtosecond pulse laser excitation. *Semiconductors*, 40(2):155–160, 2006.

[7] D. McBryde, P. Gow, S. A. Berry, M. E. Barnes, A. Aghajani, and V. Apostolopoulos. Multiple double-metal bias-free terahertz emitters. *Applied Physics Letters*, 104(20), 2014.

[8] Bernd M. Fischer, Matthias Hoffmann, Hanspeter Helm, Rafal Wilk, Frank Rutz, Thomas Kleine-Ostmann, Martin Koch, and Peter Uhd Jepsen. Terahertz time-domain spectroscopy and imaging of artificial rna. *Opt. Express*, 13(14):5205–5215, Jul 2005.

[9] Naoto Nagai, Ryoichi Kumazawa, and Ryoichi Fukasawa. Direct evidence of inter-molecular vibrations by {THz} spectroscopy. *Chemical Physics Letters*, 413(4–6):495 – 500, 2005.

[10] Ian F. Akyildiz, Josep Miquel Jornet, and Chong Han. Terahertz band: Next frontier for wireless communications. *Physical Communication*, 12:16 – 32, 2014.

[11] AV Smirnova, AM Baryshevb, SV Pilipenkoa, NV Myshonkovaa, VB Bulanova, MY Arkhipova, IS Vinogradova, SF Likhacheva, et al. Space mission millimetron for terahertz astronomy. In *SPIE Astronomical Telescopes+ Instrumentation*, pages 84424C–84424C. International Society for Optics and Photonics, 2012.

[12] Xiang Yang, Xiang Zhao, Ke Yang, Yueping Liu, Yu Liu, Weiling Fu, and Yang Luo. Biomedical applications of terahertz spectroscopy and imaging. *Trends in Biotechnology*, 34(10):810 – 824, 2016.

[13] David M. Slocum, Elizabeth J. Slingerland, Robert H. Giles, and Thomas M. Goyette. Atmospheric absorption of terahertz radiation and water vapor continuum effects. *Journal of Quantitative Spectroscopy and Radiative Transfer*, 127:49 – 63, 2013.

[14] Brian J Drouin, Shanshan Yu, Charles E Miller, Holger SP Müller, Frank Lewen, Sandra Brünken, and Hideta Habara. Terahertz spectroscopy of oxygen, o 2, in its 3 σ- g and 1 δ electronic states: Thz spectroscopy of o2. *Journal of Quantitative Spectroscopy and Radiative Transfer*, 111(9):1167–1173, 2010.

[15] Thomas W Crowe, Tatiana Globus, Dwight L Woolard, and Jeffrey L Hesler. Terahertz sources and detectors and their application to biological sensing. *Philosophical Transactions of the Royal Society of London A: Mathematical, Physical and Engineering Sciences*, 362(1815):365–377, 2004.

[16] B. Wu, H. Wang, K. Chen, R. Zhang, Y. Yang, and C. Ying. Calibration of terahertz spectrum by using carbon monoxide. In *2016 URSI Asia-Pacific Radio Science Conference (URSI AP-RASC)*, pages 1748–1750, Aug 2016.

[17] Holger S.P. Müller, Kaori Kobayashi, Kazumasa Takahashi, Kazuko Tomaru, and Fusakazu Matsushima. Terahertz spectroscopy of {N18O} and isotopic invariant fit of several nitric oxide isotopologs. *Journal of Molecular Spectroscopy*, 310:92 – 98, 2015. Spectroscopy of Radicals and Ions in Memory of Marilyn Jacox.

[18] Herbert M Pickett. Thz spectroscopy of the atmosphere. In *Optoelectronics' 99-Integrated Optoelectronic Devices*, pages 2–6. International Society for Optics and Photonics, 1999.

[19] Gwyn P Williams. Filling the thz gap—high power sources and applications. *Reports on Progress in Physics*, 69(2):301, 2006.

[20] Quanyong Lu and Manijeh Razeghi. Recent advances in room temperature, high-power terahertz quantum cascade laser sources based on difference-frequency generation. In *Photonics*, volume 3, page 42. Multidisciplinary Digital Publishing Institute, 2016.

[21] Shunsuke Kono, Masahiko Tani, Ping Gu, and Kiyomi Sakai. Detection of up to 20 thz with a low-temperature-grown gaas photoconductive antenna gated with 15 fs light pulses. *Applied Physics Letters*, 77(25):4104–4106, 2000.

[22] Masahiko Tani, Kwang-Su Lee, and X-C Zhang. Detection of terahertz radiation with low-temperature-grown gaas-based photoconductive antenna using 1.55 μm probe. *Applied Physics Letters*, 77(9):1396–1398, 2000.

[23] Bradley Ferguson and Xi-Cheng Zhang. Materials for terahertz science and technology. *Nat Mater*, 1(1):26–33, 09 2002.

[24] A. N. Bogomazova, E. M. Vassina, T. N. Goryachkovskaya, V. M. Popik, A. S. Sokolov, N. A. Kolchanov, M. A. Lagarkova, S. L. Kiselev, and S. E. Peltek. No dna damage response and negligible genome-wide transcriptional changes in human embryonic stem cells exposed to terahertz radiation. *Scientific Reports*, 5:7749 EP –, 01 2015.

[25] Yiwen Sun, Ming Yiu Sy, Yi-Xiang J Wang, Anil T Ahuja, Yuan-Ting Zhang, and Emma Pickwell-MacPherson. A promising diagnostic method: Terahertz pulsed imaging and spectroscopy. *World Journal of Radiology*, 3(3):55–65, 03 2011.

[26] Calvin Yu, Shuting Fan, Yiwen Sun, and Emma Pickwell-MacPherson. The potential of terahertz imaging for cancer diagnosis: A review of investigations to date. *Quantitative Imaging in Medicine and Surgery*, 2(1):33–45, 03 2012.

[27] Philip C Ashworth, Emma Pickwell-MacPherson, Elena Provenzano, Sarah E Pinder, Anand D Purushotham, Michael Pepper, and Vincent P Wallace. Terahertz pulsed spectroscopy of freshly excised human breast cancer. *Optics express*, 17(15):12444–12454, 2009.

[28] Caroline B Reid, Anthony Fitzgerald, George Reese, Robert Goldin, Paris Tekkis, PS O'Kelly, Emma Pickwell-MacPherson, Adam P Gibson, and Vincent P Wallace. Terahertz pulsed imaging of freshly excised human colonic tissues. *Physics in Medicine and Biology*, 56(14):4333, 2011.

[29] K Kamburoğlu, N Ö Yetimoĝlu, and H Altan. Characterization of primary and permanent teeth using terahertz spectroscopy. *Dentomaxillofacial Radiology*, 43(6):20130404, 07 2014.

[30] YC Shen, T Lo, PF Taday, BE Cole, WR Tribe, and MC Kemp. Detection and identification of explosives using terahertz pulsed spectroscopic imaging. *Applied Physics Letters*, 86(24):241116, 2005.

[31] John F Federici, Brian Schulkin, Feng Huang, Dale Gary, Robert Barat, Filipe Oliveira, and David Zimdars. Thz imaging and sensing for security applications—explosives, weapons and drugs. *Semiconductor Science and Technology*, 20(7):S266, 2005.

[32] Masahiko Tani, Michael Herrmann, and Kiyomi Sakai. Generation and detection of terahertz pulsed radiation with photoconductive antennas and its application to imaging. *Measurement Science and Technology*, 13(11):1739, 2002.

[33] Yi Huang, Neda Khiabani, Yaochun Shen, and Di Li. Terahertz photoconductive antenna efficiency. In *2011 International Workshop on Antenna Technology (iWAT)*. Institute of Electrical and Electronics Engineers (IEEE), mar 2011.

[34] D. H. Auston. Picosecond optoelectronic switching and gating in silicon. *Appl. Phys. Lett.*, 26:101–103, 1975.

[35] M. Y. Frankel, J. F. Whitaker, G. A. Mourou, F. W. Smith, and A. R. Calawa. High-voltage picosecond photoconductor switch based on low-temperature-grown gaas. *IEEE Transactions on Electron Devices*, 37(12):2493–2498, Dec 1990.

[36] Abhishek Singh, Sanjoy Pal, Harshad Surdi, SS Prabhu, S Mathimalar, Vandana Nanal, RG Pillay, and GH Döhler. Carbon irradiated semi insulating gaas for photoconductive terahertz pulse detection. *Optics express*, 23(5):6656–6661, 2015.

[37] M. E. Barnes, D. McBryde, G. J. Daniell, G. Whitworth, A. L. Chung, A. H. Quarterman, K. G. Wilcox, A. Brewer, H. E. Beere, D. A. Ritchie, and V. Apostolopoulos. Terahertz emission by diffusion of carriers and metal-mask dipole inhibition of radiation. *Opt. Express*, 20(8):8898–8906, Apr 2012.

[38] T. Dekorsy, T. Pfeifer, W. Kutt, and H. Kurz. Subpicosecond carrier transport in gaas surface-space-charge fields. *Phys. Rev. B*, 47:3842–3849, Feb 1993.

[39] M. B. Johnston, D. M. Whittaker, A. Corchia, A. G. Davies, and E. H. Linfield. Simulation of terahertz generation at semiconductor surfaces. *Phys. Rev. B*, 65(16):165301, April 2002.

[40] G. Klatt, F. Hilser, W. Qiao, M. Beck, R. Gebs, A. Bartels, K. Huska, U. Lemmer, G. Bastian, M.B. Johnston, M. Fischer, J. Faist, and T. Dekorsy. Terahertz emission from lateral photo-dember currents. *Opt. Express*, 18(5):4939–4947, Mar 2010.

[41] M. E. Barnes, S. A. Berry, P. Gow, D. McBryde, G. J. Daniell, H. E. Beere, D. A. Ritchie, and V. Apostolopoulos. Investigation of the role of the lateral photo-dember effect in the generation of terahertz radiation using a metallic mask on a semiconductor. *Opt. Express*, 21(14):16263–16272, Jul 2013.

[42] Vladimir M. Shalaev. Optical negative-index metamaterials. *Nat Photon*, 1(1):41–48, 01 2007.

[43] Viktor G Veselago. The electrodynamics of substances with simultaneously negative values of ϵ and μ. *Soviet Physics Uspekhi*, 10(4):509, 1968.

[44] Willie J. Padilla, Dimitri N. Basov, and David R. Smith. Negative refractive index metamaterials. *Materials Today*, 9(7–8):28 – 35, 2006.

[45] D. R. Smith, Willie J. Padilla, D. C. Vier, S. C. Nemat-Nasser, and S. Schultz. Composite medium with simultaneously negative permeability and permittivity. *Phys. Rev. Lett.*, 84:4184–4187, May 2000.

[46] J.B. Pendry, A.J. Holden, D.J. Robbins, and W.J. Stewart. Magnetism from conductors and enhanced nonlinear phenomena. *IEEE Transactions on Microwave Theory and Techniques*, 47(11):2075–2084, 1999.

[47] Jiangfeng Zhou, Thomas Koschny, and Costas M. Soukoulis. Magnetic and electric excitations in split ring resonators. *Opt. Express*, 15(26):17881–17890, Dec 2007.

[48] Withawat Withayachumnankul and Derek Abbott. Metamaterials in the terahertz regime. *IEEE Photonics Journal*, 1(2):99–118, 2009.

[49] Nicholas Fang, Hyesog Lee, Cheng Sun, and Xiang Zhang. Sub–diffraction-limited optical imaging with a silver superlens. *Science*, 308(5721):534–537, 2005.

[50] David Schurig, JJ Mock, BJ Justice, Steven A Cummer, John B Pendry, AF Starr, and DR Smith. Metamaterial electromagnetic cloak at microwave frequencies. *Science*, 314(5801):977–980, 2006.

[51] Antanas Reklaitis. Terahertz emission from inas induced by photo-dember effect: Hydrodynamic analysis and monte carlo simulations. *Journal of Applied Physics*, 108(5), 2010.

[52] E. Moreno, M. F. Pantoja, S. G. Garcia, A. R. Bretones, and R. G. Martin. Time-domain numerical modeling of thz photoconductive antennas. *IEEE Transactions on Terahertz Science and Technology*, 4(4):490–500, July 2014.

[53] M Özişik. *Finite difference methods in heat transfer.* CRC Press, Boca Raton, 1994.

[54] S. González García, B. García Olmedo, and R. Gómez Martín. A time-domain near- to far-field transformation for fdtd in two dimensions. *Microwave and Optical Technology Letters*, 27(6):427–432, 2000.

[55] C.P. Hong. *Computer modelling of heat and fluid flow in materials processing.* IoP, Bristol, 2004.

[56] Hans Langtangen. *Computational partial differential equations : numerical methods and Diffpack programming.* Springer, Berlin New York, 2003.

[57] Richard Johnson. *The handbook of fluid dynamics.* CRC Press, Boca Raton, Fla, 1998.

[58] Jenö Sólyom. *Fundamentals of the Physics of Solids: Volume II: Electronic Properties.* Springer, 2009 edition, 12 2008.

[59] W.F. Fang and K. Itoi. On the time-dependent drift-diffusion model for semiconductors. *Journal of Differential Equations*, 117(2):245 – 280, 1995.

[60] David S. Wilkinson. *Mass Transport in Solids and Fluids (Cambridge Solid State Science Series).* Cambridge University Press, 11 2000.

[61] Zhenyue Zhu. Quantum Hall Effects. Master's thesis, Oklahoma State University, the Netherlands, 2007.

[62] Ling Hsiao and Kaijun Zhang. The relaxation of the hydrodynamic model for semiconductors to the drift–diffusion equations. *Journal of Differential Equations*, 165(2):315 – 354.

[63] P. Degond and P.A. Markowich. On a one-dimensional steady-state hydrodynamic model for semiconductors. *Applied Mathematics Letters*, 3(3):25 – 29.

[64] C. L. Wilson. Hydrodynamic carrier transport in semiconductors with multiple band minima. *IEEE Transactions on Electron Devices*, 35(2):180–187, Feb 1988.

[65] Shin-Chi Lee and Ting-Wei Tang. Transport coefficients for a silicon hydrodynamic model extracted from inhomogeneous monte-carlo calculations. *Solid-State Electronics*, 35(4):561 – 569.

[66] Richard Dorf. *The electrical engineering handbook.* CRC/Taylor & Francis, Boca Raton, FL, 2006.

[67] Jerry Whitaker. *The electronics handbook.* CRC Press IEEE Press, Boca Raton, Fla, 1996.

[68] Jagdeep Shah and R. C. C. Leite. Radiative recombination from photoexcited hot carriers in gaas. *Phys. Rev. Lett.*, 22:1304–1307, Jun 1969.

[69] Ivan Pisarenko and Eugeny Ryndin. Numerical drift-diffusion simulation of gaas pin and schottky-barrier photodiodes for high-speed aiiibv on-chip optical interconnections. *Electronics*, 5(3):52, 2016.

[70] Chih-Tang Sah. *Fundamentals of solid-state electronics.* World Scientific, Singapore River Edge, NJ, 1991.

[71] Joachim Piprek. *Optoelectronic Devices : Advanced Simulation and Analysis.* Springer Science+Business Media, Inc, New York, NY, 2005.

[72] J.P. Colinge. *Physics of semiconductor devices.* Springer, New York, 2006.

[73] Marius Grundmann. *The physics of semiconductors : an introduction including nanophysics and applications.* Springer, Cham, 2015.

[74] Emmanouil Kioupakis, Daniel Steiauf, Patrick Rinke, Kris T. Delaney, and Chris G. Van de Walle. First-principles calculations of indirect auger recombination in nitride semiconductors. *Phys. Rev. B*, 92:035207, Jul 2015.

[75] Daniel Steiauf, Emmanouil Kioupakis, and Chris G Van de Walle. Auger recombination in gaas from first principles. *Acs Photonics*, 1(8):643–646, 2014.

[76] Lachlan E. Black. *Surface Recombination Theory.* Springer International Publishing, Cham, 2016.

[77] William H. Press, Saul A. Teukolsky, William T. Vetterling, and Brian P. Flannery. *Numerical Recipes in C (2Nd Ed.): The Art of Scientific Computing.* Cambridge University Press, New York, NY, USA, 1992.

[78] Joseph Bak. *Complex analysis.* Springer Science+Business Media, LLC, New York, 2010.

[79] Johannes Grabmeier. *Computer algebra handbook : foundations, applications, systems.* Springer, Berlin New York, 2003.

[80] Dragica Vasileska. *Computational electronics semiclassical and quantum device modeling and simulation.* CRC Press, Boca Raton, 2010.

[81] Kane S Yee et al. Numerical solution of initial boundary value problems involving maxwell's equations in isotropic media. *IEEE Trans. Antennas Propag*, 14(3):302–307, 1966.

[82] John David Jackson. *Classical electrodynamics.* Wiley, New York, NY, 3rd ed. edition, 1999.

[83] Wenquan Sui. *Time-domain computer analysis of nonlinear hybrid systems.* CRC Press, Boca Raton, 2002.

[84] Stephen Gedney. *Introduction to the finite-difference time-domain (FDTD) method for electromagnetics.* Morgan & Claypool, San Rafael, Calif. (1537 Fourth Street, San Rafael, CA 94901 USA, 2011.

[85] G. Mur. Absorbing Boundary Conditions for the Finite-Difference Approximation of the Time-Domain Electromagnetic-Field Equations. *Electromagnetic Compatibility, IEEE Transactions on*, pages 377–382, 1981.

[86] S. R. Rengarajan and Y. Rahmat-Samii. The field equivalence principle: illustration of the establishment of the non-intuitive null fields. *IEEE Antennas and Propagation Magazine*, 42(4):122–128, Aug 2000.

[87] J. G. Ruch and G. S. Kino. Transport properties of gaas. *Phys. Rev.*, 174:921–931, Oct 1968.

[88] Roderick W Mccoll, Ronald L Carter, JM Owens, and Tsay-Jiu Shieh. Gaas mesfet simulation using pisces with field-dependent mobility-diffusivity relation. *IEEE Transactions on Electron Devices*, 34(10):2034–2039, 1987.

[89] D. H. Auston. Picosecond optoelectronic switching and gating in silicon. *Applied Physics Letters*, 26(3):101–103, 1975.

[90] Withawat Withayachumnankul and Mira Naftaly. Fundamentals of measurement in terahertz time-domain spectroscopy. *Journal of Infrared, Millimeter, and Terahertz Waves*, 35(8):610–637, 2014.

[91] Hans Christian Bakken Skjeie. Terahertz time-domain spectroscopy. Master's thesis, Institutt for elektronikk og telekommunikasjon, 2012.

[92] Samuel P Mickan and X-C Zhang. T-ray sensing and imaging. *International Journal of High Speed Electronics and Systems*, 13(02):601–676, 2003.

[93] James Lloyd-Hughes and Tae-In Jeon. A review of the terahertz conductivity of bulk and nano-materials. *Journal of Infrared, Millimeter, and Terahertz Waves*, 33(9):871–925, 2012.

[94] Jagdeep Shah and RCC Leite. Radiative recombination from photoexcited hot carriers in gaas. *Physical Review Letters*, 22(24):1304, 1969.

[95] Michael Schall and Peter Uhd Jepsen. Photoexcited gaas surfaces studied by transient terahertz time-domain spectroscopy. *Opt. Lett.*, 25(1):13–15, Jan 2000.

[96] Gavin B. G. Stenning, Graham J. Bowden, Lewis C. Maple, Simon A. Gregory, Alberto Sposito, Robert W. Eason, Nikolay I. Zheludev, and Peter A. J. de Groot. Magnetic control of a meta-molecule. *Opt. Express*, 21(2):1456–1464, Jan 2013.

[97] Simon A Gregory, Gavin B G Stenning, Graham J Bowden, Nikolay I Zheludev, and Peter A J de Groot. Giant magnetic modulation of a planar, hybrid metamolecule resonance. *New Journal of Physics*, 16(6):063002, 2014.

[98] J. Kim, C.S. Cho, and J.W. Lee. Cpw bandstop filter using slot-type srrs. *Electronics Letters*, 41(24):1333–1334, 2005.

[99] P.R. Castillo-Aranibar, A. Garcia-Lamperez, D. Segovia-Vargas, M. Salazar-Palma, and S. Barbin. Multiple split-ring resonators for tri-band filter with asymmetric response. In *Microwave Optoelectronics Conference (IMOC), 2011 SBMO/IEEE MTT-S International*, pages 75–78, 2011.

[100] Cheng-Jung Lee, K.M.K.H. Leong, and T. Itoh. Metamaterial transmission line based bandstop and bandpass filter designs using broadband phase cancellation. In *Microwave Symposium Digest, 2006. IEEE MTT-S International*, pages 935–938, 2006.

[101] I. Gil, F. Martin, X. Rottenberg, and W. De Raedt. Tunable stop-band filter at q-band based on rf-mems metamaterials. *Electronics Letters*, 43(21):1153–1153, 2007.

[102] K. Yang, H. Wang, Z. Lei, Y. Xie, and H. Lai. Cpw-fed slot antenna with triangular srr terminated feedline for wlan/wimax applications. *Electronics Letters*, 47(12):685–686, 2011.

[103] M. Palandoken, A. Grede, and H. Henke. Broadband microstrip antenna with left-handed metamaterials. *Antennas and Propagation, IEEE Transactions on*, 57(2):331–338, 2009.

[104] F. Bilotti, A. Alu, and L. Vegni. Design of miniaturized metamaterial patch antennas with mu-negative loading. *IEEE Transactions on Antennas and Propagation*, 56(6):1640–1647, June 2008.

[105] M. Mehrparvar and F. Hodjat Kashani. Microstrip antenna miniaturization using metamaterial structures. In *20th Iranian Conference on Electrical Engineering (ICEE2012)*, pages 1243–1246, May 2012.

[106] S. Sajuyigbe, M. Ross, P. Geren, S. A. Cummer, M. H. Tanielian, and D. R. Smith. Wide angle impedance matching metamaterials for waveguide-fed phased-array antennas. *IET Microwaves, Antennas Propagation*, 4(8):1063–1072, Aug 2010.

[107] R. B. Greegor, C. G. Parazzoli, J. A. Nielsen, M. H. Tanielian, D. C. Vier, S. Schultz, C. L. Holloway, and R. W. Ziolkowski. Demonstration of impedance matching using a mu-negative (mng) metamaterial. *IEEE Antennas and Wireless Propagation Letters*, 8:92–95, 2009.

[108] Han Xiong, Jing-Song Hong, and Yue-Hong Peng. Impedance bandwidth and gain improvement for microstrip antenna using metamaterials. *Radioengineering*, 2012.

[109] Andreas Bitzer, Alex Ortner, and Markus Walther. Terahertz near-field microscopy with subwavelength spatial resolution based on photoconductive antennas. *Appl. Opt.*, 49(19):E1–E6, Jul 2010.

[110] Christopher W. Berry and Mona Jarrahi. Principles of impedance matching in photoconductive antennas. *Journal of Infrared, Millimeter, and Terahertz Waves*, 33(12):1182–1189, 2012.

[111] Federico Capasso, Claire Gmachl, Deborah L Sivco, and Alfred Y Cho. Quantum cascade lasers. *Physics World*, 12(6):27, 1999.

[112] Jerome Faist, Federico Capasso, Deborah L. Sivco, Carlo Sirtori, Albert L. Hutchinson, and Alfred Y. Cho. Quantum cascade laser. *Science*, 264(5158):553–556, 1994.

[113] Alessandro Tredicucci, Rudeger Kohler, Lukas Mahler, Harvey E Beere, Edmund H Linfield, and David A Ritchie. Terahertz quantum cascade lasers: first demonstration and novel concepts. *Semiconductor Science and Technology*, 20(7):S222, 2005.

[114] Carlo Sirtori, Jerome Faist, Federico Capasso, Deborah L. Sivco, Albert L. Hutchinson, and Alfred Y. Cho. Quantum cascade laser with plasmon enhanced waveguide operating at 8.4 îœm wavelength. *Applied Physics Letters*, 66(24):3242–3244, 1995.

[115] Alan Wei Min Lee, Qi Qin, Sushil Kumar, Benjamin S Williams, Qing Hu, and John L Reno. High-power and high-temperature thz quantum-cascade lasers based on lens-coupled metal-metal waveguides. *Optics letters*, 32(19):2840–2842, 2007.

[116] Karl Unterrainer, Raffaele Colombelli, Claire Gmachl, Federico Capasso, Harold Y Hwang, A Michael Sergent, Deborah L Sivco, and Alfred Y Cho. Quantum cascade lasers with double metal semiconductor waveguide resonators. *Applied physics letters*, 80(17):3060–3062, 2002.

[117] Qing Hu, Benjamin S Williams, Sushil Kumar, Hans Callebaut, Stephen Kohen, and John L Reno. Resonant-phonon-assisted thz quantum-cascade lasers with metal-metal waveguides. *Semiconductor Science and Technology*, 20(7):S228, 2005.

[118] D. Vaitiekus, D. G. Revin, K. L. Kennedy, S. Y. Zhang, and J. W. Cockburn. Quantum cascade laser with unilateral grating. *IEEE Photonics Technology Letters*, 24(23):2112–2114, Dec 2012.

[119] N. Zhuo, J. Zhang, F. Liu, L. Wang, S. Tan, F. Yan, J. Liu, and Z. Wang. Tunable distributed feedback quantum cascade lasers by a sampled bragg grating. *IEEE Photonics Technology Letters*, 25(11):1039–1042, June 2013.

[120] Giacomo Scalari, Lorenzo Sirigu, Romain Terazzi, Christoph Walther, Maria I. Amanti, Marcella Giovannini, Nicolas Hoyler, Jerome Faist, Marcin L. Sadowski, Harvey Beere, David Ritchie, L. Andrea Dunbar, and Romuald Houdre. Multi-wavelength operation and vertical emission in thz quantum-cascade lasers. *Journal of Applied Physics*, 101(8):081726, 2007.

[121] MI Amanti, M Fischer, C Walther, G Scalari, and J Faist. Horn antennas for terahertz quantum cascade lasers. *Electronics Letters*, 43(10):573–574, 2007.

[122] V. A. Fedotov, P. L. Mladyonov, S. L. Prosvirnin, and N. I. Zheludev. Planar electromagnetic metamaterial with a fish scale structure. *Phys. Rev. E*, 72:056613, Nov 2005.

[123] T. S. Kao, F. M. Huang, Y. Chen, E. T. F. Rogers, and N. I. Zheludev. Metamaterial as a controllable template for nanoscale field localization. *Applied Physics Letters*, 96(4):041103, 2010.

[124] W.N. Hardy and L.A. Whitehead. Split-ring resonator for use in magnetic resonance from 200-2000 mhz. *Review of Scientific Instruments*, 52(2):213–216, 1981.

[125] F. Martı n, J. Bonache, F. Falcone, M. Sorolla, and R. MARQUES. Split ring resonator-based left-handed coplanar waveguide. *Applied Physics Letters*, 83(22):4652–4654, 2003.

[126] Thomas J.R. Hughes and Gregory M. Hulbert. Space-time finite element methods for elastodynamics: Formulations and error estimates. *Computer Methods in Applied Mechanics and Engineering*, 66(3):339 – 363, 1988.

[127] J.N. Reddy and D.K. Gartling. *The Finite Element Method in Heat Transfer and Fluid Dynamics, Third Edition*. Computational Mechanics and Applied Analysis. Taylor & Francis, 2010.

[128] Peter P. Silvester and Ronald L. Ferrari. *Finite Elements for Electrical Engineers:*. Cambridge University Press, Cambridge, 3 edition, 009 1996.

[129] Žaklina J. Mančić and Vladimir V. Petrovic. Strong and weak fem formulations of higher order for quasi-static analysis of shielded planar transmission lines. *Microwave and Optical Technology Letters*, 53(5):1114–1119, 2011.

[130] Lennart Edsberg. *Introduction to Computation and Modeling for Differential Equations*. Wiley, 2015.

[131] Shunsuke Yamakawa and Shi-aki Hyodo. Electronic state calculation of hydrogen in metal clusters based on gaussian–fem mixed basis function. *Journal of alloys and compounds*, 356:231–235, 2003.

[132] C. A. J. Fletcher. *Computational Galerkin Methods*. Springer Nature, 1984.

[133] M. Kuzuoglu and R. Mittra. Frequency dependence of the constitutive parameters of causal perfectly matched anisotropic absorbers. *IEEE Microwave and Guided Wave Letters*, 6(12):447–449, 1996.